Published in final edited form as:
Lithos. 2016 February 1; 244: 74–93. doi:10.1016/j.lithos.2015.11.028.

Sulfur and metal fertilization of the lower continental crust

Marek Locmelis[1,2,*], **Marco L. Fiorentini**[2], **Tracy Rushmer**[3], **Ricardo Arevalo Jr.**[1], **John Adam**[3], **Steven W. Denyszyn**

[1]NASA Goddard Space Flight Center, Greenbelt, Maryland, USA

[2]Centre for Exploration Targeting and ARC Centre of Excellence for Core to Crust Fluid Systems, School of Earth and Environment, The University of Western Australia, Perth, Australia

[3]ARC Centre of Excellence for Core to Crust Fluid Systems, Department of Earth and Planetary Sciences, Macquarie University, Sydney, Australia

Abstract

Mantle-derived melts and metasomatic fluids are considered to be important in the transport and distribution of trace elements in the subcontinental lithospheric mantle. However, the mechanisms that facilitate sulfur and metal transfer from the upper mantle into the lower continental crust are poorly constrained. This study addresses this knowledge gap by examining a series of sulfide- and hydrous mineral-rich alkaline mafic-ultramafic pipes that intruded the lower continental crust of the Ivrea-Verbano Zone in the Italian Western Alps. The pipes are relatively small (< 300 m diameter) and primarily composed of a matrix of subhedral to anhedral amphibole (pargasite), phlogopite and orthopyroxene that enclose sub-centimeter-sized grains of olivine. The 1 to 5 m wide rim portions of the pipes locally contain significant blebby and disseminated Fe-Ni-Cu-PGE sulfide mineralization.

Stratigraphic relationships, mineral chemistry, geochemical modelling and phase equilibria suggest that the pipes represent open-ended conduits within a large magmatic plumbing system. The earliest formed pipe rocks were olivine-rich cumulates that reacted with hydrous melts to produce orthopyroxene, amphibole and phlogopite. Sulfides precipitated as immiscible liquid droplets that were retained within a matrix of silicate crystals and scavenged metals from the percolating hydrous melt, associated with partial melting of a metasomatized continental lithospheric mantle. New high-precision chemical abrasion TIMS U-Pb dating of zircons from one of the pipes indicates that these pipes were emplaced at 249.1 ± 0.2 Ma, following partial melting of lithospheric mantle pods that were metasomatized during the Eo-Variscan oceanic to continental subduction (~420–310 Ma). The thermal energy required to generate partial melting of the metasomatized mantle was most likely derived from crustal extension, lithospheric decompression and subsequent asthenospheric rise during the orogenic collapse of the Variscan belt (< 300 Ma).

[*]corresponding author: Marek.Locmelis@nasa.gov.

Electronic Appendix
A1 – Accuracy and precision of the laser ablation ICP-MS and bulk rock analyses.
A2 – Full mineral chemistry data set.
A3 – Core-rim comparison of mineral phases from Valmaggia.
A4 – Summary of new bulk rock data generated during this study.

Unlike previous models, outcomes from this study suggest a significant temporal gap between the occurrence of mantle metasomatism, subsequent partial melting and emplacement of the pipes. We argue that this multi-stage process is a very effective mechanism to fertilize the commonly dry and refractory lower continental crust in metals and volatiles. During the four-dimensional evolution of the thermo-tectonic architecture of any given terrain, metals and volatiles stored in the lower continental crust may become available as sources for subsequent ore-forming processes, thus enhancing the prospectivity of continental block margins for a wide range of mineral systems.

1. Introduction

The Ivrea-Verbano Zone (IVZ) in northwest Italy (Fig. 1) represents a section of continental crust and lithospheric mantle that was uplifted during the Alpine orogeny (Mehnert, 1975; Garuti et al., 1980; Rutter et al., 1993). Because of its exposure, it is an excellent natural laboratory to study the formation and evolution of the Earth's lower continental crust and continental lithospheric mantle. Thus, previous studies of the IVZ have contributed significantly to the understanding of the dynamic evolution of lower crustal and upper mantle rocks (e.g. (Mehnert, 1975; Rivalenti et al., 1981; Zingg, 1983; Sills and Tarney, 1984; Quick et al., 1994; Henk et al., 1997; Barboza et al., 1999).

Despite the wealth of previous work, only little research has been done on a series of mafic-ultramafic alkaline pipe-like intrusions that intruded into the lower stratigraphic sections of the IVZ (Garuti et al., 2001; Fiorentini et al., 2002; Fiorentini and Beresford, 2008). These small intrusions (<300 m diameter) consist of amphibole-rich peridotites and hornblendites, with minor segregations of more felsic composition and host blebby and disseminated magmatic sulfide mineralization along their outer rims (Garuti et al., 2001). They have previously been interpreted as ultramafic intrusions derived from a depleted peridotite source that was metasomatically enriched in alkalis, Cu, S and platinum-group elements (Garuti et al., 2001; Fiorentini and Beresford, 2008). However, relatively little work has been done on the nature of the parental magmas of the pipes and their crystallization history.

This study integrates new electron microprobe and laser ablation ICP-MS data for individual pipe minerals with both new and previously-published bulk-rock analyses, to investigate (i) the crystallization history of the pipes and the nature of their parental magmas; (ii) the tectonic environment enabling the pipe formation; and (iii) the potential of such intrusions to produce economically important deposits of Ni, Cu and platinum-group elements (PGE). The results are used to reflect on the mechanisms that control sulfur and metal mass transfer between the upper mantle and lower continental crust. We also establish a geodynamic framework for the emplacement of the pipes, supported by new high-precision U-Pb zircon geochronology on the Valmaggia pipe.

2. Geological Background

2.1 Ivrea-Verbano Zone

The Ivrea-Verbano Zone outcrops subvertically over ~150 × 15 km, extending from northwest Italy into southern Switzerland (Fig. 1). To the west and northwest, the Canavese

segment of the Insubric Line separates the IVZ from the Austroalpine Domain (Schmid et al., 1987). To the south and southeast, the Cremosina, Cossato-Mergozzo-Brissago and Pogallo Lines separate the IVZ from the Strona-Ceneri Zone (Boriani et al., 1990).

Three main lithological formations exist: (i) the Mafic Complex, (ii) the Kinzigite Formation, and (iii) the mantle peridotites (Fig. 1). The Mafic Complex, formed from mantle-derived mafic magmas underplating the basement of the Southern Alps, can be subdivided into three units: the Layered Series (or Cyclic Units), the Main Gabbro and the Diorite Unit (e.g. (Rivalenti et al., 1984; Pin and Sills, 1986; Sinigoi et al., 1994; Garuti et al., 2001). The Layered Series is the lowermost unit and consists of a sequence of layered mafic-ultramafic rocks with intercalated septa of strongly migmatized metasediments (Rivalenti et al., 1984; Garuti et al., 2001). It is overlain by the Main Gabbro, which grades upwards into the Diorite Unit. A metasedimentary septum of up to 100 meters thick separates the Layered Series and the Main Gabbro, suggesting that the two formations represent two different intrusive events (Ferrario et al., 1982; Garuti et al., 2001). The Kinzigite Formation is in magmatic contact with the top of the Diorite Unit. It consists of a prograde metamorphic sequence of middle amphibolite-to-granulite facies rocks, primarily composed of metapelites intercalated with mafic meta-igneous rocks, marbles, quartzites and pegmatites (Schnetger, 1994; Bea and Montero, 1999).

The mantle peridotites occur within the Mafic Complex and are considered to represent obducted slices of the continental mantle that outcrop along the Insubric Line near Baldissero, Balmuccia and Finero (Fig. 1; (Shervais and Mukasa, 1991; Hartmann and Wedepohl, 1993; Zanetti et al., 1999; Grieco et al., 2001; Mazzucchelli et al., 2010; Wang et al., 2013; Schaltegger et al., 2015; Wang and Becker, 2015). The peridotites have undergone different degrees of partial melting and metasomatism shown by melt extraction modelling using major and minor element compositions complemented by Nd and Sr isotopic data (Hartmann and Wedepohl, 1993). Most prominently, highly refractory major element compositions and distinct incompatible trace element enrichments in the amphibole- and phlogopite-bearing peridotite at Finero have been interpreted to reflect metasomatism of depleted peridotite by water-rich fluids derived from dehydration and melting of subducted sediments and oceanic crust (Exley et al., 1982; Hartmann and Wedepohl, 1993; Zanetti et al., 1999).

2.2 Pipe-like bodies

Five pipes are known to exist in the IVZ. However, due to dense vegetation and difficult terrain in the area, it is possible that more pipes outcrop, but are yet to be discovered. Four pipes are hosted within the Main Gabbro of the Mafic Complex at the localities of Bec d'Ovaga, Castello di Gavala, Valmaggia, and Piancone la Frera (Fig. 1). One pipe, at Fei di Doccio, is hosted within the Kinzigite Formation. No pipes have been found inside the Layered Series or the Diorite Unit. Due to poor exposure, the geometries of the pipes and their relationship to the host rocks are primarily derived from abandoned underground mines that were mined for Fe and Ni until the end of World War 2 (Fiorentini et al., 2002).

The pipes occur as small discordant intrusive bodies up to 300 m in diameter and mostly consist of hydrated peridotites and hornblendites that appear as massive dark-grey rocks

with a medium to coarse grained texture in outcrops. The pipes do not display distinct layering and have sharp contacts with the wall rock without the development of any chilled margins (Fig. 2-A, B). Along the margins, there is a discontinuous but common presence of 1–100 cm-thick pegmatoidal gabbroic pods. From a broad petrographical and geochemical perspective, the pipes are mafic-ultramafic and have an alkaline signature as well as unusually elevated incompatible element contents, as reflected in the abundance of accessory minerals, including apatite, zircon, dolomite and baddeleyite (Garuti et al., 2001; Fiorentini et al., 2002; Zaccarini et al., 2014).

The field relationships, mafic-ultramafic lithologies and cumulate textures of the pipes imply an intrusive igneous origin. All pipes have remarkably similar compositions and were previously considered to have been emplaced coevally ~290 Ma ago (*cf.* (Garuti et al., 2001). However, existing geochronological data have largely relied on $^{207}Pb/^{206}Pb$ stepwise-evaporation methodologies. This technique does not include U isotopic data and for Phanerozoic rocks will result in the calculation of an age older than a $^{206}Pb/^{238}U$ age, with no possibility of assessing the effects of Pb loss or other disturbance in the U-Pb systematics of the zircons. In addition, since the pipes prevalently intruded Early Permian magmatic rocks of the Mafic Complex, the lack of textural information on the analyzed zircons makes it unclear whether the obtained ages refer to crystallization ages or reflect an inherited population. Therefore, reliance upon $^{207}Pb/^{206}Pb$ analyses for zircons of this age leaves open the question of the accuracy of the published ages of the pipes. Here we present new high-precision U-Pb zircon data by the Chemical Abrasion Isotope Dilution Thermal Ionization Mass Spectrometry (CA-ID-TIMS) method showing that the emplacement and crystallization age of at least one of the pipes is significantly younger than previously reported.

2.3 Nickel-sulfide mineralization

Nickel-Cu-PGE sulfide occurrences in the Ivrea-Verbano Zone vary widely in texture, composition and ore-grade. Low-grade Ni-Cu-PGE sulfide mineralization with bulk rock tenors of up to 1.65 wt.% Ni, up to 0.84 wt.% Cu, and up to 350 ppb Pt+Pd is commonly associated with peridotitic, pyroxenitic and gabbroic dykes and sills with intercalated granulitic metasediments which occur within the Layered Series at the transition between the upper mantle region and the lower continental crust (Garuti et al., 1986; Zaccarini et al., 2014). Conversely, higher-grade mineralization is associated with the pipes that intruded the upper Mafic Complex and lower Kinzigite Formation, with bulk-rock tenors up to 10.7 wt.% Ni, 11.9 wt.% Cu, 4464 ppb Pt+Pd and 367 ppb Ru+Ir+Os (Garuti et al., 2001; Zaccarini et al., 2014).

The sulfide assemblage in the pipes consists mostly of pyrrhotite, pentlandite and chalcopyrite with minor amounts of cubanite, mackinawite and pyrite. The sulfides occur mainly along the 1–5 m wide rim portions of the pipes, predominantly as polyphase intergranular blebs of random distribution with grain sizes between < 100 μm and 5–10 cm (Fig. 2-C). Sulfides are comparatively rare in the core portions of the pipes, where they occur as both intragranular and intergranular polyphase blebs composed of pyrrhotite with minor amounts of pentlandite and chalcopyrite and grain sizes between <100 μm and 1 mm.

Whereas the blebs appear to have segregated as droplets from an immiscible sulfide liquid, the occurrence of small chalcopyrite-dominated veins crosscutting the rock (commonly < 50 μm width) suggests that some of the (Cu) sulfides were remobilized and redeposited during postmagmatic processes, as is commonly observed in most orthomagmatic sulfide deposits (Garuti et al., 2001; Seat et al., 2004; Locmelis et al., 2010; Zaccarini et al., 2014; Le Vaillant et al., 2015).

3. Samples and Analytical Methods

3.1 Samples

Four pipes were investigated during this study, specifically those at Bec d'Ovaga, Castello di Gavala, Valmaggia and Fei di Doccio. Thus, the samples comprise pipes that intruded into the Mafic Complex as well as into the Kinzigite Formation (Fig. 1).

Samples for mineral analyses: The key characteristics of the samples analyzed by electron microprobe and laser ablation ICP-MS are summarized in Table 1. Due to the inaccessibility of the old underground mines, three samples were taken from an existing collection at the University of Leoben: two polished blocks that represent the central portions of the pipes at Bec d'Ovaga (BO-1) and Castello di Gavala (GV-1262), and one polished block from Fei di Doccio (FD-1) that was collected from a mining dump just at the entrance of the main underground working area. These are the same samples that were previously characterized by Garuti et al. (2001), who analyzed the major and minor element chemistry of silicate minerals as well as the bulk-rock chemistry. New samples were collected from the Valmaggia pipe, which is cross-cut by underground galleries that are still relatively accessible (Fiorentini et al., 2002). Samples were taken from outcrops in the core portion of the pipe (VMG-7) and the rim portion (I-7) and used for the preparation of polished sections as well as for bulk rock analyses. A third sample (VMG-2, approximately 5 kg) was collected from the mine floor near sample site VMG-7 and used for geochronological and bulk-rock analysis.

Samples for bulk rock analyses: In addition to the three bulk rock analyses of the newly sampled material from Valmaggia, 39 bulk-rock powders from the collection at the University of Leoben were analyzed for their major, minor and trace element compositions, comprising material from all four pipes, i.e. Bec d'Ovaga (19 samples), Castello di Gavala (n = 10), Fei di Doccio (n = 3) and Valmaggia (n = 7; Appendix A-4). Because these samples were only available as rock powders, the results (together with the data reported Garuti et al., 2001) are used to better constrain the bulk composition of the pipes.

3.2 Mineral chemistry analysis

Electron-microprobe analysis—A Jeol Superprobe JXA-8200 equipped with wavelength and energy dispersive spectrometers (WDS and EDS) in the Eugen Stumpfl Microprobe Laboratory at the University of Leoben was used to determine the major and minor element chemistry of olivine, orthopyroxene, amphibole and phlogopite. Silicates were measured in WDS mode with an accelerating voltage of 15 kV and a beam current of 10 nA. The analyses of the samples for Si, Ti, Al, Cr, Fe, Mn, Mg, Ca, Na, K and Ni were

carried out using the Kα lines, and were calibrated on natural K-feldspar, albite, diopside, chromite, rhodonite, ilmenite and metallic Ni using the method described in Zaccarini et al. (2014). Major elements have been determined with an accuracy of ≤ 3% and an external precision of ≤ 3% (2-sigma), whereas minor elements (< 1 wt%) have been determined with an accuracy of ≤ 5% and an external precision of ≤ 4% (2-sigma).

Laser ablation ICP-MS analysis—The trace element chemistry of amphibole, phlogopite, orthopyroxene and olivine was determined using a laser ablation inductively coupled plasma mass spectrometer (LA-ICP-MS) system in the Geochemical Analysis Unit (GAU), CCFS/GEMOC, Macquarie University, Sydney, Australia. The system consists of a Photon Machines Excite excimer laser coupled to an Agilent 7700 quadrupole ICP-MS. The analyses used 85 μm beam sizes, a pulse rate of 5 Hz and a fluence of 10.6 J/cm^2. The instrument was calibrated against the NIST 610 silicate glass standard reference material (National Institute of Standards and Technology, Gaithersburg, USA, (Norman et al., 1996). Magnesium values obtained by electron microprobe were used as the internal standard to determine the trace element concentrations in the silicate grains. The BCR2-g standard (basaltic glass prepared from the U.S. Geological reference material BCR-2, Columbia River, USA, (Norman et al., 1998)) was analyzed as an unknown for quality control during each run. The BCR2-g analyses show that the accuracy for all elements is ≤6% when compared to the preferred published values (Norman et al., 1998), with an external precision of ≤7% (2-sigma; a detailed discussion on the accuracy and precision is presented in Appendix A-1).

3.3 Chemical abrasion isotope dilution TIMS U-Pb Geochronology

Sample VMG-2 was crushed using the SelFrag high-voltage pulse disaggregator at Curtin University (Western Australia). All further processing and analyses were carried out at the University of Western Australia. In order to extract zircons the crushed sample material was processed using a Frantz isodynamic separator and heavy liquid separation using LST (a lithium heteropolytungstate). Resulting concentrates of non-magnetic, high-density minerals yielded several small, euhedral zircons that were handpicked under a binocular microscope. These zircons were then pre-treated according to the chemical-abrasion technique described by Mattinson (2005), in which zircons are annealed at 850°C for 60 hours, followed by leaching in HF at 200°C for 12 hours to remove zones of Pb loss. The samples were spiked with an in-house ^{205}Pb-^{235}U tracer solution, calibrated against SRM981, SRM 982 (for Pb), and CRM 115 (for U), as well as an externally calibrated U-Pb solution (the JMM solution from the EarthTime consortium).

The zircons were dissolved by vapor-transfer of HF, using Teflon microcapsules in a Parr pressure vessel placed in a 200°C oven for six days. No further chemical separation was required. The resulting residue was re-dissolved in HCl and H_3PO_4 and placed on outgassed, zone-refined rhenium single filament with 5 μL of silicic acid gel. U-Pb isotopic analyses were carried out using a Thermo Triton T1 mass spectrometer, in peak-jumping mode using a secondary electron multiplier. Uranium was measured as an oxide (UO_2). Fractionation and dead time were monitored using SRM981 and SRM 982. Mass fractionation was 0.02 ± 0.06 %/amu. Data were reduced and plotted using the software packages Tripoli (from

CIRDLES.org) and Isoplot 4.15 (Ludwig, 2011). All uncertainties are reported at 2-sigma.The weights of the grains were calculated from measurement of photomicrographs and estimates of the third dimension. The weight of the grains only provides information about absolute U concentration and does not contribute to the age calculation, and an uncertainty of 50% may be attributed to this estimate.

3.4 Bulk-rock geochemical analysis

Bulk-rock compositions of the samples from Valmaggia were determined by X-Ray Fluorescence (XRF) and Inductively Coupled Plasma-Mass Spectrometry (ICP-MS), following open vessel multi-acid digestion at Geoscience Laboratories ('Geolabs'), Sudbury, Canada. Major and minor elements have been determined with an accuracy typically better than 2 % and a 2-sigma external precision ≤ 3 %, whereas most trace elements have been determined with an accuracy of ≤ 6% and a precision of ≤ 6% (2-sigma). A detailed discussion on the accuracy and precision is presented in Appendix A-1.

4. Results

4.1 Petrography

The dominant silicate minerals in the pipes are olivine, amphibole, phlogopite, and orthopyroxene (Fig. 3-A). Amphibole occurs as two main phases: a minor green type (cummingtonite), which occurs both in the groundmass and as a partial-replacement of other silicates, and a largely dominant brown amphibole (pargasite), which is abundant in all of the pipe rocks. Textures are locally variable but more uniform towards the core of the pipes. Here they show poikilitic features with large (generally > 1 cm) subhedral to anhedral crystals of orthopyroxene, pargasite and phlogopite (partially) enclosing rounded grains of olivine (sub-centimeter diameter; Fig. 3-A). The 1 to 5 meter wide rim portions of the pipes are characterized by network-like sulfide mineralization (Fig 3-B) dominated by pyrrhotite and lesser amounts of pentlandite and chalcopyrite (*cf.* section 2.3). The pipes contain a wide range of accessory phases, including locally abundant plagioclase and clinopyroxene. Due to grain sizes too small for laser ablation ICP-MS analyses in the studied samples (i.e. < 50 um), compositional data for individual crystals of plagioclase and clinopyroxene are not included in this study. Other accessory phases include apatite, spinel, ilmenite, magnetite, carbonates, rutile, titanite zircon, and baddeleyite. The pipe emplaced into the meta-sediments at Fei di Doccio also contains accessory graphite. A detailed description of the accessory mineral assemblage has been presented by Garuti et al. (2001) and Fiorentini et al. (2002).

4.2 Mineral chemistry

Averages of major, minor and trace elements in the silicate minerals from individual pipes are presented in Table 2. The full data set (including each individual mineral analysis) is presented in electronic Appendix A-2. Most of the analyses are of mineral cores, but a number of grains from the Valmaggia samples were examined in depth for mineral core-rim variation. In these cases, no systematic elemental zonation was observed (Appendix A-3).

Olivine—Olivine displays a notable variation in forsterite content (Fo = molar [Mg/(Mg +Fe)]*100) across the individual pipes. Olivines from the pipe at Fei di Doccio, which was emplaced into the metasedimentary rocks of the Kinzigite Formation, have the lowest Fo content between 71.9 and 72.4 (Fig. 4, Tab. 2, Appendix A-2). Grains from the pipes that were emplaced into the Mafic Complex have notably higher Fo, ranging from 74.9 to 76.5 at Valmaggia, and from 81.2 to 85.2 at Bec d'Ovaga and Castello di Gavala. Nickel concentrations in olivine vary between 600 and 2000 ppm and correlate inversely with Fo within individual pipes with the exception of Fei Di Doccio where Ni is widely independent of Fo (Fig. 4-A). Manganese and Co display negative correlations with Fo (Fig. 4-B, C), with Mn concentrations between 1700 and 3000 pm and Co contents between 74 and 190 ppm. Titanium (< 34 ppm) and Ca (< 255 ppm) concentrations are generally low (Fig. 4-D). Olivines from the pipes are depleted in most trace elements relative to the primitive mantle (PM, (McDonough and Sun, 1995) and display remarkably similar PM-normalized element patterns in the four pipes (Fig. 4-E). However, distinct positive anomalies exist for B and Li with concentrations ~5 to 20 times higher than the primitive mantle values, whereas Mn and Ge are moderately enriched (~2–3 times the mantle)

Orthopyroxene—The enstatite content of orthopyroxene ranges from 75.6 to 78.8 in the Valmaggia and Fei di Doccio pipe samples, and from 82.7 to 84.5 in the samples from Bec d'Ovaga and Castello di Gavala (Table 2, Appendix A-2). All orthopyroxene grains are low in Ca, with concentrations between ~0.1 and 0.5 wt. % CaO, and have Al_2O_3 contents between 1.4 and 3.9 wt. %. The grains show considerable variation in Cr (130 – 1400 ppm), Ti (46 – 790 ppm) and Na (31 – 970 ppm). Mantle-normalized (N) trace element patterns for orthopyroxene show depletions in most trace elements compared to the primitive mantle (Fig. 5-A). All pipes display similar trace element patterns, including distinct positive B anomalies (B_N = 5 – 35). Orthopyroxene is also mostly depleted in rare earth elements (REE) when compared to the composition of the C-1 chondrite (McDonough and Sun, 1995). C-1 normalized values range from ~0.1 to 1 in grains from Bec d'Ovaga and Valmaggia to values as low as ~ 0.05 to 0.1 in grains from Castello di Gavala and Fei di Doccio (Fig. 5-B). All spider diagrams for orthopyroxenes exhibit concave-upward shapes with a steeper increase towards Tm, Yb and Lu and are characterized by negative Sm and Gd anomalies that are separated by positive Eu anomalies. The most distinct negative Sm and Gd anomalies exist in grains from Fei di Doccio, which is the only pipe emplaced into meta-sedimentary rocks.

Amphibole—Following the mineral formula and site occupancy classification of Leake et al. (1997), the green amphiboles from the pipes fall in the cummingtonite field whereas the brown amphiboles are pargasites. Textural relationships and local replacement of magmatic silicates by cummingtonite imply a secondary, postmagmatic origin for this type of amphibole. Thus, as this study investigates the magmatic origin of the pipes, only the hydromagmatic brown pargasites were analyzed.

Pargasites from Bec d'Ovaga are characterized by magnesium numbers (Mg# = molar [Mg/(Mg+Fe)]*100) between 82.8 and 85.2, whereas grains from Castello di Gavala (79.4 – 81.1), Fei di Doccio (75.8 – 77.6) and Valmaggia (71.1 – 77.5) have notably lower Mg#. All

pargasites contain 13 to 15 wt.% Al_2O_3, 2.7 to 3.6 wt.% Na_2O and 0.2 to 1.1 wt.% K_2O. Titanium concentrations range from 1.2 to 2.2 wt.% TiO_2 in the samples from Castello di Gavala and Fei di Doccio and from 2.0 to 3.3 wt.% TiO_2 at Bec d'Ovaga and Valmaggia. Furthermore, most grains contain notable amounts of Cr_2O_3, with concentrations between 0.3 and 0.8 wt. % in grains from Valmaggia, Bec d'Ovaga and Castello di Gavala. Conversely, grains from Fei di Doccio are relatively Cr-poor with ~0.1 wt. % Cr_2O_3. Due to similarities in T sites occupancies (with close to the maximum of 2 ^{iv}Al per formula unit), A sites (close to full and with K/Na < 0.4), Fe^{+2} and Mg occupancies of M2 sites (Fe^{+2} + Mg = 0.2–0.3 apfu), Mg# and Cr_2O_3. The pargasites resemble crystals experimentally precipitated from hydrous basanite and olivine-basalt melts at 0.5–2.0 GPa and 1000–1050 °C (Adam et al., 2007).

The pargasites are generally enriched in incompatible trace and minor elements relative to the composition of the primitive mantle (Fig. 6-A) and display distinct negative Cs, P and Li anomalies with values 0.5 to 8 times the primitive mantle. Grains from Castello di Gavala and Bec d'Ovaga display distinct positive Pb anomalies relative to primitive mantle, with Pb_N values between 100 and 460, as opposed to Pb_N values of 30 to 55 in grains from Valmaggia and Fei di Doccio. The pargasites have REE concentrations 1–2 orders of magnitude above the C1 chondrite composition with convex-upward chondrite normalized patterns that show a slight enrichment from La to Pr and flattening towards Yb and Lu (Fig. 6-B). Distinct negative Eu anomalies exist for grains from Fei di Doccio. Overall, all pargasites have very similar patterns, although grains from Castello di Gavala have notably flatter patterns and overall lower REE contents.

Phlogopite—Phlogopites in the sample from Bec d'Ovaga have Mg# between 88.4 and 89.1, whereas grains from Fei di Doccio and Valmaggia have lower Mg# between 81.5 and 87.4 (Table 2; Appendix A2). It is noted that phlogopite from Castello di Gavala is not included in this study as the grains were too small for laser ablation ICP-MS analysis (< 50 μm). Phlogopite from Fei di Doccio is characterized by low Ti concentrations between 0.8 and 1.5 wt. % TiO_2. Grains from Bec d'Ovaga and Valmaggia have notably higher TiO_2 contents, mostly between 3.1 and 4.4 wt. % TiO_2. Sodium concentrations range between 0.7 and 2.6 wt. % Na_2O. The grains also contain minor amounts of Cr, ranging from 0.1 to 0.3 wt.% Cr_2O_3 in the sample from Fei di Doccio and from 0.3 to 0.6 wt. % at Bec d'Ovaga and Valmaggia.

Overall, phlogopites from all samples have very similar mantle-normalized trace element patterns (Fig. 7-A). Lithium displays positive, but highly variable anomalies, ranging from Li_N = 50 – 67 in grains from Fei di Doccio to Li_N = 3 – 9 at Valmaggia and Li_N = 0.2 – 0.5 at Bec d'Ovaga. Furthermore, all of the phlogopites have variable but strongly positive anomalies for Cs, Rb and Ba. The largest anomalies are for grains from Bec d'Ovaga (Cs_N = 1000–5200, Rb_N = 1700–2400, and Ba_N = 450–1300); grains from the other localities display values of Cs_N = 210 – 1600, Rb_N = 190 – 730, and Ba_N = 210 – 910. All grains are also enriched in Pb (Pb_N = ~100 – 200), Nb (Nb_N = ~10 – 40), Ta (Ta_N = 10 – 40), Ti (Ti_N = 5 – 25) and B (B_N = ~5 – 15).

Chondrite-normalized REE patterns are widely similar for all samples with values 1–2 orders of magnitude below the C1 chondrite composition, except for positive Eu anomalies (Eu_N = ~1–6; Fig. 7-B). Phlogopites from Fei di Doccio and Valmaggia show an enrichment of light rare earth elements relative to heavy rare earth elements, whereas grains from Bec d'Ovaga display a flatter pattern due to notably depleted La to Nd signatures.

4.3 Bulk-rock geochemical data

New bulk-rock data for the Valmaggia, Castello di Gavala and Bec d'Ovaga pipes are presented in Figure 8 and Appendix A-4. These new data together with the previously published results of Garuti et al. (2001) show that the pipes are distinctively alkali-rich (with ~0.5 – 1.5 % Na_2O) and sodic in character (with molecular Na/(Na+K) ≈ 0.8). In addition, the new data indicate that the pipe compositions are both more variable and less mafic than previously reported (*cf.* Garuti et al., 2001). They are also generally enriched in incompatible minor and trace elements, together with some compatible and chalcophile elements. Specifically, Li, large ion lithophile elements (Cs, Rb, K and Ba), actinides (Th and U), Pb, Sr, high field strength elements (Nb, Ta, Zr, Hf and Ti), and light rare earths (LREE) are all enriched relative to the primitive mantle (Fig. 8-A). Positive anomalies exist for Pb and Ba, whereas Cr displays a distinct negative anomaly. Niobium, Ta and (with the exception of Valmaggia) Ti display mild-to-moderate negative peaks. Although B was not analyzed, its bulk-rock contents must be notably enriched relative to the primitive mantle, based on the high B contents in the main silicate phases of the pipes (*cf.* Figs. 4–7). Light rare earths are enriched relative to heavy rare earths, although the latter have relatively shallow slopes on C-1 chondrite normalized plots (Fig. 8-B). The pipes at Bec d'Ovaga, Castello di Gavala and Valmaggia display positive Eu and negative Sm anomalies when compared to the C-1 chondrite, whereas the pipe at Fei di Doccio is characterized by negative Eu and Sm anomalies. Consistent with the presence of sulfide mineralization, the pipes are enriched in S, Co, Ni, Cu, Mo and PGE in their mineralized rim portions (locally up to 15 – 20 wt. % S, as opposed to < 5% S in the central portions) as outlined in section 2.3.

4.4 U-Pb geochronological data

Six zircons were analyzed from sample VMG-2 (Table 3, Figure 9). Calculated weights were between 0.4 and 1.2 μg, with U concentrations between 149 and 302 ppm. Th/U ratios were consistent with each other, between 0.63 and 0.82. One analysis (#6) had a young $^{206}Pb/^{238}U$ age of 214 Ma, and is interpreted to show effects of Pb loss not fully mitigated by the chemical abrasion process. The other five data overlap within 2σ uncertainties, with a well-constrained weighted-mean $^{206}Pb/^{238}U$ age of 249.1 ± 0.2 Ma (N = 5, MSWD = 0.71). The relatively large analytical uncertainty in the $^{207}Pb/^{235}U$ ratio is likely the result of low initial ^{235}U concentration. The five tightly-clustered data with uniform agreement with respect to the $^{206}Pb/^{238}U$ age permit the interpretation that this is the magmatic age of the rock.

5. Discussion

The pipes were previously interpreted to be derived from a depleted mantle protolith that was flushed with hydrous metasomatic fluids, which lowered the peridotite solidus and caused partial melting (Garuti et al., 2001; Fiorentini and Beresford, 2008). This produced pockets of volatile-rich magmas that evolved and intruded into the lower-to-mid continental crust rocks of the Ivrea-Verbano Zone. To build upon current knowledge on these rarely studied pipes, and to question some of the existing ideas, we reassess the existing model integrating new and existing datasets to evaluate:

- **i.** how the pipes were formed and/or emplaced,
- **ii.** the composition of the parental magma(s),
- **iii.** its/their source and evolution,
- **iv.** the role of mantle metasomatism and nature of the metasomatizing fluid, and
- **v.** the implications for sulfur and metal fertilization of the lower continental crust.

5.1 Pipe emplacement

A number of possible mechanisms exist by which the pipes may have formed and each has implications for assessing the origin of the parental magma, the source and nature of the metasomatic agent (if present), and the prevailing geodynamic environment during the pipe emplacement. Mechanisms include:

- **a.** Tectonic emplacement of peridotites that were metasomatized either before or after their emplacement;
- **b.** Metasomatic alteration and replacement of local country rocks;
- **c.** Intrusion of mafic-ultramafic magmas.

(a) A tectonic emplacement of metasomatized peridotites is unlikely because the pipes do not resemble mantle-derived peridotites such as alpine-type peridotites and type II lherzolite xenoliths from alkaline basalts. They are too enriched in Ca, Al, Fe and alkalis, and have relatively low Mg# and MgO. Although some of the Fe-enrichment can be attributed to sulfide accumulation, olivine has forsterite contents between 72 and 84, which are significantly beneath the 88–93 typical of mantle-derived peridotites (Nixon, 1987). In addition, while the margins of the pipes are locally faulted and show evidence of minor deformation, there is no structural evidence for the occurrence of significant shear zones that may have resulted from the tectonic emplacement of mantle-derived peridotite bodies.

(b) A metasomatic replacement origin was effectively discounted by Garuti et al. (2001), who argued that the lack of correlation between pipe and wall-rock geochemistry was inconsistent with such an origin. Field relationships and the occurrence of sharp lithological contacts between pipes and wall-rocks support this interpretation. The observations and the data generated in this study are in accordance with the interpretations in Garuti et al. (2001) and argue against a metasomatic replacement for the genesis of the pipes.

This leaves the possibility of (c) an intrusive magmatic model. The pipe-like nature of the bodies, textural relationships between silicate minerals, and the compositons of bulk rocks and minerals suggest that the pipes have formed as heteradcumulates in an open-system magmatic environment. A necessary feature of this origin is the role of reaction relationships in the production of hydrous silicate phases. This can be described via the reaction:

$$\text{Olivine} \pm \text{clinopyroxene} + \text{melt} \rightarrow \text{orthopyroxene} + \text{amphibole} \pm \text{phlogopite} \quad (1)$$

Figure 10 illustrates this relationship, showing liquidus phase equilibria for a hydrous olivine basalt melt together with bulk-pipe and pipe mineral compositions, plotted within the basalt tetrahedron of Yoder and Tilley (1962). The original compositions have been adjusted to remove their sulfide components and then re-cast as CMAS ($CaO–MgO–Al_2O_3–SiO_2$) components following the procedure of O'Hara (1968). The bulk compositions of the pipes fall on a mixing line between the peritectic P1 for reaction (1) and olivine, consistent with an admixture of trapped inter-cumulus melt, residual olivine, orthopyroxene, amphibole and phlogopite crystallized in peritectic proportions. Textural criteria (i.e. poikilitic orthopyroxene, amphibole and phlogopite enclosing rounded olivine) and phase equilibria for hydrous mafic systems (Fig. 10) suggest that the earliest precipitates were probably dunitic. During subsequent cooling of the magmatic system hydrous melts, that continued to ascend through the pipes, began reacting with the early precipitated cumulates to form amphibole and phlogopite via reaction 1. It is noted that because olivine remains an abundant phase in all pipes, reaction (1) cannot have proceeded to completion. Because clinopyroxene is consumed by reaction (1) its scarcity in the pipes is consistent with this same reaction. Olivine persisted simply because of its greater initial volume and the incompletion of the reaction prior to final solidification of the pipes.

The role of plagioclase is not shown in reaction (1) but must nevertheless have been significant at certain stages of pipe crystallization. This is evident from the new bulk-rock data generated during this study that show that local plagioclase-rich segregations exist within the pipes with up to 25 wt% bulk-rock Al_2O_3. These are too aluminous to represent residual inter-cumulus melts and must instead be considered as plagioclase-rich cumulates. Because plagioclase is comparatively scarce in the more mafic samples where olivine is abundant, it is likely that plagioclase was added to the cumulate sequence relatively late in crystallization history of the pipes.

In summary, the peritectic textural relationships observed in the pipes suggests that early olivine-rich cumulates were subsequently and pervasively percolated by hydrous mafic melts that continued to ascend through the pipes as the magmatic system cooled; these later melts reacted with and/or consumed early formed olivine ± clinopyroxene to produce orthopyroxene, amphibole and phlogopite. Hence, the individual pipes are interpreted to represent open-end conduits within a larger magmatic plumbing system.

5.2 Composition of the parental magma

Because of the cumulate-related origin of the pipes, indirect methods are necessary to establish the nature of the parent magma from which the pipes crystallized. In the first

instance, we assumed that (broadly speaking) the parent magma was basaltic. This is in keeping with similarities between the ferromagnesian silicates in the pipes and equivalent near-liquidus phases experimentally crystallized from natural basalts (Adam et al., 2007). We also assumed that crystallization occurred under steady state conditions, so that the melt composition was effectively constant, and that equilibrium occurred between all phases. Although this is undoubtedly simplistic, it allows broad limits to be placed on the nature and provenance of the parent magma. To attempt more than this with the information available would be unrealistic.

In the case just outlined, the peritectic P1 represents both the parental melt and any inter-cumulus melt. Concentrations of incompatible elements in the parental melt can also be calculated, provided only that the fraction F of retained inter-cumulus melt is also known. In the absence of independent criteria for estimating F, a range of possibilities was investigated. The first was to assume that no inter-cumulus melt was retained in the pipes (i.e. F = 0). This allows melt concentrations to be calculated directly from mineral and bulk rock compositions using appropriate mineral/melt partition coefficients. For this purpose we used partition coefficients from Adam and Green (2006) and Adam et al. (2007), and mineral compositions from Appendix A-2 with bulk data from Garuti et al. (2001). The latter were used in preference to the new data because they include reliable estimates of S.

The calculated melt compositions are presented in Table 4 and Figure 11. They are strongly enriched in incompatible elements relative to the primitive mantle and an average ocean island basalt (based on data from the GEOROC data base: http://georoc.mpch-mainz.gwdg.de/georoc/; Fig 11-A). The melt compositions also have several features in common with lamproites in the Western Alps and Spain, including high Cs, Th, U and Pb contents (Turner et al., 1999; Peccerillo and Martinotti, 2006). However, while the mineral assemblage of the pipes and the calculated melt compositions strongly resemble lamproites, several differences exist. Lamproites are ultra-potassic rocks (>3 wt.% K_2O) with high K_2O/Al_2O_3 ratios of >0.6 (Foley et al., 1987), whereas the pipes have distinctly lower K contents (<<1 wt.% K_2O; K_2O/Al_2O_3 <<0.1). Moreover, the amphiboles in the pipes are pargasites as opposed to the richterites that are characteristic of lamproites (Mitchell and Bergman, 1991). In addition the assumption of zero inter-cumulus melt is a simplified and improbable scenario for the pipe crystallization, making a lamproitic origin of the pipes unlikely. To model melt compositions where F was > 0, we used the equilibrium / batch melting equation of Shaw (2006):

$$C_m = C_m = \frac{C_o}{D + F - DF} \quad (2)$$

Where C_m = concentration in melt, C_o = the original bulk rock concentration, F = the degree of melting, and D is the bulk-rock/melt partition coefficient for the residual mineral assemblage.

We assumed that F was equal to the fraction of retained inter-cumulus melt and that (prior to trapping) the inter-cumulus melt and parent melt were of the same composition. The bulk-rock data used in the calculations were from Garuti et al. (2001) which include S analyses.

Major element concentrations in melting residues were calculated by subtracting 10 % (or 20%) of an olivine basalt melt (equivalent to P1 and based on melt from run 1925 of Adam et al., 2007) from the bulk-pipe compositions. Mineral modes for the resulting residue were then calculated from mass balances using mineral data from Table 2 and Appendix A-2, together with an estimated bulk-sulfide composition. Mineral/melt partition coefficients were taken from Adam and Green (2006) and Adam et al. (2007). Sulfide melt/silicate melt partition coefficients were estimated from the relationships given by Kiseeva and Wood (2013), using the melt composition from run 1925 of Adam et al. (2007), and the estimated bulk-sulfide composition. The latter was calculated by regressing the bulk-rock data of Garuti et al. (2001) to find a mixture of sulfide phases (pyrrhotite, pentlandite and chalcopyrite) that best fitted the whole-rock trends for chalcophile elements and S. This gave a composition dominated by pyrrhotite with 59.9 % (by weight) Fe, 1.24 % Cu, 0.12 % Co, 1.0 % Ni and 37.0 % S, which is supported by petrographic observations that show a pyrrhotite dominated sulfide assemblage.

The resulting incompatible-element patterns are flatter and have smaller absolute concentrations (Fig 11-B) than calculated previously for F = 0. The melt composition calculated assuming 10% of retained parental melt in the pipes (retained as inter-cumulus melt, where F = 10 %) has overall concentrations that are slightly higher than calculated for a scenario where F = 20 %; however, the shapes for both patterns are nearly identical. For these two possibilities the parental magma displays some analogies with an average ocean-island basalt composition, but the calculated melts are notably enriched in Cs, Pb and P, and distinctly depleted in Nb and Ta. These characteristics have more in common with arc-related magmas, but are also shared by adakite-like lavas from the Meshkan district of north-east Iran that formed within a Tethyan (post) collisional setting (Shabanian et al., 2012); Fig. 11-B). A parent of this kind would be consistent not only with the distinctive incompatible-element enrichments of the pipes, but also with their volatile-rich character which is required for the precipitation of amphibole and phlogopite (Merzbacher and Eggler, 1984; Johnson et al., 1991). Accordingly, it is argued that the parental melt feeding the pipes was probably basaltic, but with some unusual and arc-like (perhaps adakitic) characteristics.

5.3 Origin and evolution of the parental magma

Garuti et al. (2001) and Fiorentini and Beresford (2008) suggested that the pipes formed from partial melting of a harzburgitic protolith that was percolated and refertilized by a metasomatic agent derived from a wet mantle plume. Here we re-assess this model, focusing on mineral trace element chemistry, which provides more robust information compared to earlier bulk-rock studies that may not be able to discriminate different magmatic/metasomatic events and processes.

Olivine forsterite contents between 72 and 85, together with negative correlations with Mn and Co (Fig. 4-B, C), suggest that the pipes underwent variable degrees of fractionation during emplacement and crystallization. This is particularly evident in the case of the Fei di Doccio pipe, which has the lowest Mg# and was emplaced at the highest structural level among the known occurrences in the Ivrea-Verbano Zone. However, as discussed above, the similar bulk-rock and silicate chemistry of all samples suggests that all pipes were derived

from the same magma source and emplaced coevally in an open-ended conduit plumbing system.

Pargasites in the pipes are characterized by TiO_2 contents between 1–3 wt.% and Nb concentrations >> 1 ppm with Nb/La ratios between 0.6 and 2.1 (Tab 2; Appendix A-2). These features indicate a hydromagmatic origin for the pargasites and crystallization from an evolved silicate melt (Coogan et al., 2001; Gillis et al., 2003) that reacted with the early precipitated olivine and clinopyroxene following reaction (1). The presence of magmatic amphibole implies a water content of at least 4 wt.% in the magma at this stage (Merzbacher and Eggler, 1984; Johnson et al., 1991). Similarly, Costa et al. (2001) showed that anomalously high Na contents of phlogopite, as observed in the pipes with concentrations up to 2.2 wt.% Na_2O, reflect open system processes involving evolved, water-rich melts with high Na/(Na+K) contents and reaction with early crystallized phases (e.g. olivine and pyroxene), conditions remarkably similar to the open-system conduit model proposed for the pipes.

The elevated contents of Li and B (two highly fluid-mobile trace elements; e.g. (Taylor and McLennan, 1985) observed in olivine, orthopyroxene and amphibole (Figs 4 to 7) suggest that pipes originated from melting of a mantle reservoir that was anomalously enriched in incompatible elements and associated with subducted oceanic crust (Brenan et al., 1998; Gillis et al., 2003; Foley et al., 2013). Furthermore, low V/Sc ratios in olivine (Fig. 12) suggest oxidizing conditions during olivine crystallization (Canil and Fedortchouk, 2001; Lee et al., 2005; Mallmann and O'Neill, 2007; Foley et al., 2013), which supports the involvement of a subducted crustal component in the primary mantle source of the pipes (Kelley and Cottrell, 2009; Rowe et al., 2009).

The mineral chemistry of olivine, orthopyroxene and pargasite imply that processes associated with the subduction of crustal material fertilized the mantle source that generated the pipes. However, the trace element chemistry of phlogopite seems to contradict such a model. Low Zr/Nb and Cs/Rb ratios in phlogopite (Fig. 13) suggest the involvement of a juvenile mantle source instead of crustal input (Fritschle et al., 2013). Moreover, the low-to-moderate Ba contents of phlogopite (< 8000 ppm) are an indicator for reducing conditions during crystallization of this mineral phase (Foley et al., 1987; Fritschle et al., 2013).

Interestingly, the different source signatures recorded by phlogopite and the other mineral phases mimic the contrasting histories commonly observed in lamproites, where depleted mantle-derived minerals (e.g. olivine xenocrysts) indicative of a harzburgitic origin are associated with hydrous, incompatible element-rich minerals derived from metasomatic fluids (Foley, 1992; Prelevic and Foley, 2007; Prelević et al., 2008). However, as discussed above, a lamproitic origin for the pipes is unlikely due to several distinctive mineralogical and geochemical differences and an improbable scenario used for the melt calculations (i.e. F=0). Conversely, the subduction-related signatures observed in the other silicates, together with the volatile character of the pipes and their distinctive bulk-rock incompatible-element enrichments and calculated parental melt compositions (for F > 0), support the hypothesis that the pipes were derived from an arc-like (possibly adakitic) parent.

5.4 Mantle metasomatism and pipe emplacement

In order to understand the geodynamic environment where and when the pipes were emplaced, it is important to constrain the larger tectonic setting of the IVZ in the Permian and before. In Europe, the Variscan orogeny from 420 to 290 Ma is related to the collision between Laurussia and Gondwana and intervening terranes leading to the formation of the Pangea supercontinent (Matte, 2001; Faure et al., 2009). At the end of the Carboniferous, the belt extended from the Caucasus, to the East, to the southern Appalachians in North America (Matte, 2001). In Western Europe, Variscan basement occurs mainly in the following domains: Armorica, French Massif Central, Vosges, Bohemian Massif, Alps, Corsica-Sardinia, Pyrenees and the Iberian Belt (von Raumer et al., 2009).

The Variscan cycle is subdivided into three mains stages (Ledru et al., 1994; Faure et al., 2009): (i) the Eo-Variscan oceanic to continental subduction from 420 to 380 Ma, marked by high-pressure metamorphism (Faure et al., 2009); (ii) the Meso-Variscan collision stage from 360 to 310 Ma, resulting from the tectonic accretion of terranes mainly derived from the Gondwana continental margin (Schaltegger, 1997; Eichhorn et al., 2000; Paquette et al., 2003); and (iii) the Neo-Variscan gravitational collapse from ca. 300 to 280 Ma, which is marked by exhumation of the partially molten root of the orogenic crust forming migmatitic domes (Burg and Vanderhaeghe, 1993; Vanderhaeghe et al., 1999; Ledru et al., 2001). This is followed by the development of a series of Permian rifts (e.g. (Stampfli et al., 2013) coeval with underplating of mantle-derived magmas at 280–250 Ma (Tribuzio et al., 1999; Eichhorn et al., 2000; Paquette et al., 2003; Cocherie et al., 2005; Monjoie et al., 2007; Sinigoi et al., 2011). In this geodynamic framework, our new high-precision U-Pb zircon age of 249.1 ± 0.2 Ma indicates an emplacement of at least the Valmaggia pipe coincidental with the development of continental-scale Permian rifting which is in contrast to the older Pb-Pb ages of Garuti et al. (2001). It should be noted that $^{207}Pb/^{206}Pb$ ages calculated from our analyses of the VMG-2 zircons (Table 3) are generally in agreement with the results presented by Garuti et al. (2001). However, the new $^{206}Pb/^{238}U$ age presented here is considered to be more precise and accurate due to the identification of a coherent, concordant cluster of data that shows no evidence for the effects of Pb loss nor inheritance of older crystals or overgrown cores.

Based on this new geodynamic framework and the results of this study, it is reasonable to hypothesize that the melts that intruded as pipes into the deep continental crust of the IVZ at ~249 Ma were derived from partial melting of a continental lithospheric mantle. This region of the mantle had been previously metasomatized in the Eo-Variscan during oceanic and continental subduction, which started as early as ca. 420 Ma. This process is illustrated in Fig. 14. The most striking differences for the genesis and emplacement of the pipes between the previous models and this new one are 1) the nature of the metasomatizing fluids, 2) the absence of a mantle plume, and) the relative timing between mantle metasomatism and pipe emplacement.

Nature of the metasomatizing fluid—In the model presented in this study, there is no need to invoke the emplacement of a mantle plume as suggested by Garuti et al. (2001) and Fiorentini and Beresford (2008). The metasomatic fluids are largely related to subduction

processes that started in the Eo-Variscan (Fig. 14-A to D). The thermal energy required to generate partial melting of these metasomatized pods of lithospheric mantle was most likely derived by decompression melting and asthenospheric rise, which occurred during the orogenic collapse of the Variscan belt at ca. 290–250 Ma (Fig. 14-D to E). The associated lithospheric extension would have favored both the emplacement of the large underplated Mafic Complex (Fig. 14-E) and the establishment of the magmatic conduit system of the pipes (Fig. 14-F).

Relative timing between mantle metasomatism and pipe emplacement—Unlike the previous model of Garuti et al. (2001) and Fiorentini and Beresford (2008), which inferred synchronous mantle metasomatism and pipe emplacement, we emphasize a significant temporal gap between mantle metasomatism and the partial melting that led to the genesis of the parental melts that formed the pipes. This difference in timing is a fundamental aspect of the model that is proposed here as it allows the “storage” of metal- and volatile-rich pods of lithospheric mantle at active continental margins. Due to their elevated volatile content, these metasomatized pods would be more easily fusible than surrounding lithospheric mantle. Therefore, they may be reactivated due to a wide range of mechanisms, including slab break up, plume emplacement and/or post-orogenic extension and decompression melting (e.g. (Raddick et al., 2002; Peccerillo and Martinotti, 2006; Faccenna et al., 2010; Sizova et al., 2012). Melting of these pods would contribute to enhancing the fertility of continental block margins (Begg et al., 2010; Richards, 2013; Wilkinson, 2013; Mole et al., 2014; Hughes et al., 2015), as discussed in the next section on processes that facilitate metal and fluid fertilization of the deep continental crust.

5.5 Metal and fluid fertilization of the lower continental crust

Most current world-class magmatic Ni-Cu-PGE sulfide deposits formed relatively close to the Earth’s surface. The formation of near-surface magmatic sulfide deposits is widely considered to require additional S from the assimilation of crustal S-bearing rocks (Naldrett, 2004). This is related to the inverse relationship between pressure and S-solubility in a magma, i.e. the lower the pressure, the more S can be dissolved in a magma (Wendlandt, 1982; Mavrogenes and O’Neill, 1999). As a consequence, mantle-derived magmas will tend to reach upper crustal settings sulfide-undersaturated. Consequently, addition of external S or significant crystal fractionation is required to trigger sulfide saturation. The scenario would be radically different in mineral systems forming at the base of the continental crust where high pressures imply that S-saturation can be reached at lower S contents

The intragranular occurrence of sulfide blebs in early-formed silicates argues for early sulfide supersaturation in all pipes. In addition, isotopic evidence indicates that the sulfur for the Ni-Cu-PGE mineralization hosted in all pipes, irrespective of their setting in either the Mafic Complex or the Kinzigite Formation, is largely derived from mantle reservoirs (Garuti et al., 2001), thus arguing against crustal contamination as a significant S and metal source. The question arises as to why most of the mineralization in the pipes is hosted along their margins, where the average size of sulfide droplets is generally much larger than in the core portions of these magmatic bodies (see also Garuti et al., 2001; Fiorentini et al., 2002). Following the argument of Godel et al. (2013) the sub-spherical small sulfide blebs in the

core of the pipes are interpreted to have formed by early segregation of immiscible sulfide liquid upon emplacement of the magma flowing in the pipe conduits. These newly formed droplets were trapped in situ by the crystallizing framework of olivine. Conversely, following the same argument of Godel et al. (2013) the larger sulfide blebs and patches concentrated along the margins of the pipes have been transported in a flowing sulfur-saturated magma over some distance and accumulated at their present site by mechanical processes, most likely due to interaction with the host rocks. At Fei di Doccio, which historically represents the largest accumulation of pipe-hosted Ni-Cu-PGE sulfide mineralization in the IVZ (Garuti et al., 2001), the sulfide supersaturation process may have been enhanced by assimilation of graphite from the meta-sedimentary wall rocks, which caused reduction in the ascending pipe magma, thereby furthering lowering its sulfur capacity, similar to the model proposed by Tomkins et al. (2012) for the formation of magmatic sulfide mineralization in subduction-related arc environments.

Although relatively minor sources of base and precious metals in their own right, the IVZ pipes provide a rare and important insight into ore-forming processes in the deep continental crust. It is a notable feature of the pipes, that their parental magmas were not especially enriched in chalcophile elements, as reflected in the low Ni, Co and Cu contents in the calculated parental melt (Fig. 11). Thus, the pipe magmas must have undergone processes that allowed for a significant concentration of chalcophile elements into the sulfides prior to crystallization.

The low metal contents of the parental melt are readily explained if the pipes were emplaced in an open-end feeder system for ascending mafic-ultramafic magmas as discussed above. Once the pipes started to cool in their deep crustal environment, the negative pressure dependence of sulfide solubility facilitated the onset of sulfide saturation and the mechanical accumulation of mono and intermediate sulfide solution (mss and iss) in the outer parts of the pipes, where most of the Ni-Cu-PGE sulfide mineralization is now hosted. The mss and iss would have scavenged metals from the percolating (hydrous) melt and re-equilibrated at lower temperatures into the observed lower-temperature sulfide assemblage, a common process in magmatic sulfide systems (e.g. (Kullerud et al., 1969; Naldrett, 2004; Godel et al., 2007; Locmelis et al., 2009; Dare et al., 2010; Oberthür, 2011).

Depending on the timing, longevity and chemistry of such a magmatic plumbing system, focused and long-term contributions of chalcophile metals, volatiles and heat can be transferred into the base of the continental crust.

If the pipes had been emplaced in an active compressional environment during the Variscan continental collision as opposed to the extensional post-orogenic setting constrained through the high-precision geochronology presented in this study (Fig. 14), their magmatic plumbing would have attained self-organizing criticality with the establishment of high-flux conduits (cf. McCuaig and Hronsky, 2014). This would have led to focused energy and mass flux transfer from the mantle into the crust, with the potential for the formation of orthomagmatic deposits such as those hosted in the Appalachian Belt in the USA (Thompson and Naldrett, 1984), the Svecofennian Raahe-Ladoga and Vammala Belts in Finland (Eilu et al. 2012), or the magmatic Ni-Cu mineralization at the Kalatongke deposit in NW China (Li et al. 2012).

However, rather than through a network of self-organized high-flux conduits, mantle-derived magmas trickled through a series of lower energy pipes, which reflect a slow and persistent flux of magmas through the interface between the lithospheric mantle and the continental crust. In other words, the magmatic plumbing system that originated the pipes did not self-organize, with the result that high-flux networks were not established and no major ore-forming process occurred.

Even if not necessarily conducive to the synchronous genesis of economic mineral deposits, this process of metal and volatile transfer from the lithospheric mantle to the base of the continental crust can nonetheless be a very effective mechanism to fertilize the notably dry and restitic lower continental crust. Accordingly, even without necessarily generating significant syngenetic Ni-Cu-PGE mineralization, this process has the potential to add metals and volatiles into the base of the continental crust, thus seeding the ground for the genesis of later mineral systems. This process could represent an effective mechanism to enhance the metal endowment of continental block margins and paleo-margins (Richards, 2013; Wilkinson, 2013; Loucks, 2014; Mole et al., 2014; Hughes et al., 2015; Lu et al., 2015).

6. Conclusions

Sulfide- and hydrous mineral-rich peridotite pipes were emplaced into the lower continental crust of the Ivrea-Verbano Zone during the waning stages of the Variscan orogenic cycle after the Neo Variscan. Geochemical modelling and phase equilibria are consistent with a cumulate origin for the pipe rocks under lower crustal conditions. We propose that the pipes were originally conduits for mafic magmas that became filled with cumulates under open-system conditions. The earliest formed rocks were olivine cumulates. However, as the system cooled, olivine reacted with hydrous melts to produce orthopyroxene, amphibole and phlogopite. Sulfides precipitated as immiscible liquid droplets that were retained within a matrix of silicate crystals and scavenged metals from the percolating hydrous melt.

These alkaline mafic pipes, now precisely dated at 249.1 ± 0.2 Ma, were derived from partial melting of a continental lithospheric mantle that had been previously metasomatized as the result of subduction in the Eo-Variscan, which started as early as ca. 420 Ma. Unlike previous models that inferred synchronous mantle metasomatism and pipe emplacement, we emphasize a significant temporal gap between mantle metasomatism and the partial melting that led to the genesis of the parental melts that formed the pipes. This difference in timing is a fundamental aspect of the model that is proposed here, as it would allow the “storage” of metal- and volatile-rich pods of lithospheric mantle at active continental margins.

The thermal energy required to generate partial melting of the metasomatized lithospheric mantle was most likely derived from the ingressing asthenospheric mantle and lithospheric extension and decompression, which occurred during the orogenic collapse of the Variscan belt at ca. 290 Ma. This geodynamic scenario would have favored both the emplacement of the large underplated Mafic Complex and the establishment of open-end pipe conduits.

Depending on the longevity and chemistry of the magmatic plumbing system, these open-end conduits have the potential to produce focused and long-term contributions of chalcophile metals, volatiles and heat into the base of the continental crust. Even if not necessarily conducive to the synchronous genesis of mineral deposits of economic interest, this process of metal and volatile enrichment may be a very effective mechanism to fertilize the lower continental crust. Metals and volatiles stored in the lower continental crust may subsequently become the source or contributing factor for other ore-forming processes, thus enhancing the prospectivity of specific continental block margins for a wide range of mineral systems.

Acknowledgements

This work was carried out as part of foundation research project “Metal Sources and Transport Mechanisms in the Deep Lithosphere” in the Australian Research Council (ARC) Centre of Excellence for Core to Crust Fluid Systems (CCFS). Marek Locmelis, Marco Fiorentini, Tracy Rushmer and John Adam acknowledge support through the ARC Centre of Excellence for Core to Crust Fluid Systems (CE11E0070). Marek Locmelis also acknowledges support by an appointment to the NASA Postdoctoral Program at the Goddard Space Flight Center, administered by Oak Ridge Associated Universities through a contract with NASA. Marco Fiorentini also acknowledges support from the Australian Research Council through Linkage Project LP120100668, the Future Fellowship Scheme (FT110100241). The University Centrum for Applied Geosciences (UCAG) at the University of Leoben, Austria, is thanked for the access to the E.F. Stumpfl electron-microprobe. Federica Zaccarini and Giorgio Garuti are thanked for the electron microprobe analyses, guidance during field work and valuable and critical comments on the manuscript, as well as for making available a large number of highly valuable samples from the pipes. Nick Arndt, Carole Cordier, Steve Barnes, Marilena Moroni and Stefano Caruso are thanked for insightful discussions and logistical support in the field. The laser ablation ICP-MS data were obtained using instrumentation funded by DEST Systemic Infrastructure Grants, ARC LIEF, NCRIS, industry partners and Macquarie University. Will Powell is thanked for assistance with the laser ablation ICP-MS analyses. This is contribution 682 from the ARC Centre of Excellence for Core to Crust Fluid Systems http://www.ccfs.mq.edu.au.

Appendix A1 –: Accuracy and precision of the laser ablation ICP-MS mineral analyses and Geoscience Laboratory bulk-rock analyses

Laser ablation ICP-MS analyses

Repeated BCR2-g analysis during this study show that the accuracy for elements and/or masses is ≤6% when compared to the preferred published values (Norman et al., 1998), with an external precision of ≤7% (2-sigma). It is noted that several masses (e.g. ^{31}P, ^{39}K, ^{62}Ni, ^{69}Ga, ^{57}Fe) yielded less accurate and precise results. The ^{62}Ni and ^{69}Ga analysis show a low accuracy (14 to 88% deviation from preferred values) and low external 2-sigma precision (8 to 67%) caused by isobaric interferences that cannot be resolved using the low resolving power (M/ΔM=300) of quadrupole ICP-MS (Arevalo et al. 2011). As a consequence, the ^{60}Ni and ^{71}Ga values were used, which show a distinctly better accuracy (1–7%) and precision (4–9%). The ^{31}P analyses display a similarly high deviation from the preferred values (11–20%), but a notably better external precision of 5 to 9%. This is interpreted to reflect elemental variation in the distributed BCR2g glasses as implied by the wide range of published values (i.e. P = 1065 to 2208 ppm; GeoReM data base (Jochum et al., 2005). The errors of the ^{39}K and ^{57}Fe analyses of up to 16% are likely caused by the large extrapolation from ppm levels in the NIST 610 glass to weight percent levels in the BCR2g glass and, in the case of Fe, are further compounded by the measurement of a low abundance isotope (^{57}Fe) to avoid the molecular interferences that affect ^{56}Fe. However, errors caused by large extrapolation are unimportant for this study, because electron-microprobe data was used for

high abundance elements. Beryllium, B, Cr, As, Cd and Tm values are not reported by Norman et al. (1998) and the data were compared to the GeoReM preferred values (and/or the reported range for As because no preferred values are stated). The GeoReM values represent averages complied from several studies with different analytical techniques (e.g. LA-ICP-MS, TIMS, SIMS, EPMA, ID-ICP-MS), as opposed to the preferred data by Norman et al. (1998) that were primarily obtained by LA-ICP-MS (unless otherwise noted in Table A-1). Beryllium and Tm are in good agreement with the GeoReM values with a deviation of better than 5 % and external 2-sigma precisions of ~10–5 %. The Be and Tm 2-sigma precisions are slightly higher than the values for the masses discussed above which is related to the overall low abundances of these elements in BCR2g (Be = 2.3 ppm, Tm = 0.5 ppm). Boron (20–30% deviation from the GeoReM value), As (10–290%) and Cd (15–45%) display notably high deviations as well as well as low external 2-sigma precisions of the analyses (20–170%) that appear to be related to overall low abundances as well as inhomogeneity within the BCR2g glass as shown by the wide range of reported data for these elements in the GeoReM database.

Geoscience Laboratory bulk-rock analyses

Major and minor elements

The accuracy of the bulk-rock major and minor element data were assessed through the analyses of the certified reference materials BHVO-2 (United States Geological Service (USGS) basalt powder, Kilauea, Hawaii, USA) and BIR-1 (USGS basalt powder, near Reykjavik, Iceland), as well as the preliminarily certified reference material OKUM (International Association of Geoanalysts (IAG) komatiite powder, McArthur Township, Ontario, Canada). The external precision was evaluated through three analyses of OKUM and duplicate analyses of two pipe samples (GV-1285 and BO-125). All data are presented in Table A1-B.

A comparison of the BHVO-2 and BIR-1 data with the preferred GeoReM values shows that most major and minor elements were determined with an accuracy of better than 2 % (Table A1-B). It is noted that the BIR-1 analysis yielded notably higher errors for K_2O (34 %) and P_2O_5 (19 %) which can be linked to the low concentrations of these elements in BIR-1 (0.02 wt% K_2O and 0.02 wt% P_2O_5). The OKUM data are compared to the preliminarily certified IAG values as only a limited number of elements are included in the GeoReM database. The OKUM analyses support an accuracy of better than 2 % for most elements, although the Na_2O concentrations show a slightly higher deviation of 4 % from the IAG value (1.14 wt% Na_2O). The errors for K_2O (26 %) and P_2O_5 (12 %) are notably higher due the low concentrations of these elements in the OKUM (0.05 wt% K_2O and 0.03 wt% P_2O_5). The duplicate analyses of OKUM and the pipe samples show that the 2-sigma external precision of the major and minor element analysis is better than 3 % (Table A1-B); higher values are generally associated with low concentrations of an element in the analyzed sample.

Trace elements

The accuracy of the trace element data were evaluated by analyzing the certified reference material AGV-2 (USGS andesite powder, Guano Valley, Oregon USA), as well as BHVO-2

and OKUM. The external 2-sigma precision of the trace element analyses was evaluated through two analyses of OKUM and duplicate analyses of the pipe samples GV-1282, VM-1317, BO-1242 and BO-1266. All data are presented in Table A1-C.

The comparison of the AGV-2, BHVO-2 and OKUM data collected during this study with the preferred GeoReM values (for AGV-2, and BHVO-2) and IAG values (for OKUM) shows that most trace elements were determined with an accuracy of ≤ 6% (Table A1-C). Several elements analyzed in AGV-2 and BHVO-2 (e.g. Be, Cd, Ce, Sb, Zn) show notably higher deviations from the preferred GeoReM values up to ~20 %. The measured abundances of these elements, however, are well in the range of the reported concentrations in the GeoReM database and therefore are interpreted to reflect inhomogeneity in the powdered materials as well as low abundances (mostly < 2 ppm). Deviations of more than 10% for some elements measured in OKUM relative to the IGA values (Be = 52%, Cu = 11%. Sb, 10%, Ta = −25%, U = −11%) appear to be primarily related to low abundances (< 0.1 ppm).

A notable exception is the measured Li content of 9.1 ppm in AGV-2, compared to the preferred GeoReM value of 11 ppm (a deviation of −17%). The measured Li value is lower than the range reported in the GeoReM database (9.71 – 12.4 ppm). However, the analyses of BHVO2 (4.5 ppm Li, GeoReM value = 4.8 ppm, deviation = −6%) and OKUM (4.2 and 4.3 ppm Li, IAG value: 4.38, deviation: −3%) show a significantly better accuracy, suggesting that the low Li concentration reflects sample inhomogeneity than an analytical problem.

The duplicate analyses of OKUM and the pipe samples show a good external precision in the range that is expected for the level of abundances and/or sample inhomogeneity. Trace element abundances > 1 ppm have been determined with a 2-sigma external precision mostly better than 6 %, whereas lower element abundances (0.1 – 1 ppm) have been determined with an external precisions up to 40 % (2-sigma), and up to 240 % for concentrations < 0.1 ppm.

Table A1-A -

Multiple analyses of the BCR2g basaltic glass standard and comparison with reference values. Magnesium values obtained by electron microprobe were used as the internal standard.

During olivine analysis											
	BCR2g-1	**BCR2g-2**	**BCR2g-3**	**BCR2g-4**	**BCR2g-5**	**AVERAGE**	**External Precision (2-sigma)**	**GeoReM preferred value[a]**	**Deviaton from GeoReM value**	**Norman et al. 1998[b] (preferred)**	**Deviat from prefer pub valu**
Li7 (ppm)	9.52	9.02	10.32	9.86	9.80	9.70	10%	9.0	8%	9.60	1%
Be9	2.22	2.48	2.01	2.15	2.58	2.29	21%	2.3	−1%	n.d.	n.d
B11	5.98	5.81	8.15	8.50	8.48	7.38	37%	6.0	23%	n.d.	n.d
Mg25	21110	21110	21110	21110	21110	21110	0%	21472	−2%	21110	0%

During olivine analysis

	BCR2g-1	BCR2g-2	BCR2g-3	BCR2g-4	BCR2g-5	AVERAGE	External Precision (2-sigma)	GeoReM preferred value[a]	Deviaton from GeoReM value	Norman et al. 1998[b] (preferred)	Deviat from prefer pub valu
Al27	73940	74922	75752	76501	70851	74393	6%	70903	5%	71962	3%
Si29	267263	276662	275583	284751	266804	274213	5%	254157	8%	254063	8%
P31	1261	1353	1234	1315	1321	1297	7%	1615	−20%	1615	−20
Ca43	50997	50325	50864	50577	50714	50696	1%	50457	0%	50886	−0.4
Sc45	32.4	32.0	37.2	38.6	32.7	34.6	18%	33	5%	33.0	5%
Ti49	14579	14505	14652	14523	13945	14441	4%	14100	2%	13700	5%
V51	436	427	423	429	423	427.57	2%	425	1%	414	3%
Cr53	14.3	15.0	14.3	15.1	14.3	14.6	6%	17	−14%	n.d.	n.d
Mn55	1530	1507	1607	1605	1533	1556.37	6%	1550	0%	1549	0%
Fe57	87436	84257	86732	86452	81839	85343.53	5%	96386	−11%	97164	−12
Co59	37.5	36.9	36.7	38.1	37.1	37.2	3%	38	−2%	35.8	4%
Ni60	11.3	11.1	11.4	11.7	12.0	11.5	6%	13	−12%	10.8	6%
Ni62	12.7	13.0	13.7	12.6	12.3	12.8	8%	13	−1%	10.8	19%
Cu63	17.1	16.5	18.8	18.3	18.2	17.8	10%	21	−15%	19.4	−8%
Cu65	16.8	17.4	17.6	19.4	18.5	17.9	11%	21	−15%	19.4	−8%
Zn66	146	140	151	153	137	145.36	10%	125	16%	147	−1%
Ga69	34.6	31.8	53.4	62.8	31.4	42.8	67%	23	86%	22.7	88%
Ga71	22.3	21.5	22.3	24.2	22.8	22.6	9%	23	−2%	22.7	0%
Ge72	3.1	2.4	3.0	3.4	3.2	3.0	25%	1.5	101%	n.d.	n.d
Y89	33.16	32.32	33.24	33.33	34.63	33.34	5%	35	−5%	35.3	−6%
Zr90	187	182	184	190	192	187.08	4%	184	2%	194	−4%
Nb93	13.63	13.7	13.87	13.89	13.01	13.62	5%	12.5	9%	12.8	6%
Mo95	254	254	246	251	245	250.06	3%	270	−7%	244	2%
Hf178	4.76	4.85	4.76	4.73	4.98	4.82	4%	4.84	0%	5	−4%
Ta181	0.817	0.795	0.783	0.825	0.761	0.80	6%	0.78	2%	0.78	2%
Pb208	10.66	10.39	10.78	10.98	10.55	10.67	4%	11	−3%	11.5	−7%

During orthopyroxene analysis

	BCR2g-1	BCR2g-2	BCR2g-3	BCR2g-4	BCR2g-5	BCR2g-6	BCR2g-7	AVERAGE	External Precision (2-sigma)	GeoReM preferred value[a]	Deviate from GeoRe value
Li7 (ppm)	9.53	9.35	10.04	9.47	9.93	9.84	10.02	9.74	6%	9.0	8%
Be9	2.05	1.94	2.30	2.12	2.14	2.09	2.43	2.15	15%	2.30	−6%
B11	5.00	7.66	7.15	8.15	8.93	8.96	7.24	7.6	36%	6.0	26%
Na23	22836	23316	24249	23568	24277	23996	23289	23647	5%	23963	−1%
Mg25	21110	21110	21110	21110	21110	21110	21110	21110	0%	21472	−2%
Al27	73622	75287	75804	70519	71853	71584	69953	72660	6%	70903	2%
Si29	267469	272799	283758	275479	278432	283546	269976	275923	5%	254157	9%

During orthopyroxene analysis

	BCR2g-1	BCR2g-2	BCR2g-3	BCR2g-4	BCR2g-5	BCR2g-6	BCR2g-7	AVERAGE	External Precision (2-sigma)	GeoReM preferred value[a]	Deviate from GeoRe value
P31	1269	1335	1313	1317	1310	1327	1251	1303	5%	1615	−19%
K39	16551	15644	16768	16628	17080	16649	16054	16482	6%	14900	11%
Ca43	49929	51497	50451	49964	50482	50785	50203	50473	2%	50457	0%
Sc45	32.0	33.3	37.7	32.9	33.1	34.8	32.0	33.69	12%	33	2%
Ti49	14681	14501	14554	13914	13979	13938	13918	14212	5%	14100	1%
V51	427	435	429	425	426	427	427	428	2%	425	1%
Cr53	15.1	15.6	16.1	14.6	14.7	14.5	14.8	15.0	8%	17	−12%
Mn55	1527	1510	1562	1536	1543	1560	1519	1537	3%	1550	−1%
Fe57	90364	84258	85908	82407	82147	72710	81378	82739	13%	96386	−14%
Co59	36.9	37.4	38.0	37.7	37.3	37.4	37.1	37.4	2%	38	−2%
Ni60	11.2	11.3	12.0	11.7	11.5	12.0	11.5	11.6	5%	13	−11%
Ni62	12.4	12.0	12.4	11.9	11.9	12.1	13.5	12.3	10%	13	−5%
Cu63	16.4	16.9	16.8	18.2	18.1	18.3	18.0	17.5	9%	21	−17%
Cu65	16.6	16.3	17.5	18.0	18.0	18.6	18.1	17.61	10%	21.0	−16%
Zn66	141	149	146	136	143	148	138	143.14	7%	125.0	15%
Ga69	33.1	32.1	53.1	31.6	32.1	32.7	31.4	35.17	45%	23.0	53%
Ga71	22.5	22.9	24.0	23.3	24.0	23.1	22.1	23.11	6%	23.0	0%
Ge72	2.9	3.0	3.2	2.6	2.8	4.5	4.8	3.38	53%	1.5	126%
As75	1.1	1.2	1.3	1.1	1.0	2.8	4.2	1.92	132%	0.99–2.5[c]	27–84
Rb85	49.1	49.8	52.0	50.8	51.9	50.9	48.9	50.48	5%	47	7%
Sr86	334.63	337.12	344.95	337.41	346.65	347.05	337.9	340.82	3%	342	0%
Sr88	335.18	343.17	346.08	341.67	346.93	348.51	341.85	343.34	3%	342	0%
Y89	32.62	32.83	33.37	34.22	35.25	35.29	33.36	33.85	6%	35	−3%
Zr90	184	188	187	192	196	194	186	189.56	5%	184	3%
Nb93	13.43	14	14.26	12.78	13.01	13.17	12.91	13.37	8%	12.5	7%
Mo95	246	264	253	248	251	245	246	250.60	5%	270	−7%
Cd111	<0.32	<0.32	0.209	0.149	0.336	0.381	0.177	0.25	82%	0.20	25%
Cs133	1.047	1.21	1.318	1.206	1.184	1.206	1.166	1.19	13%	1.16	3%
Ba137	663.91	673.4	688.59	669.63	686.02	682.94	676.96	677.35	3%	683	−1%
La139	23.71	24.41	24.21	24.21	25.05	24.91	24.28	24.40	4%	24.7	−1%
Ce140	51.09	51.22	51.07	50.56	51.6	51.93	52.47	51.42	2%	53.3	−4%
Pr141	6.77	6.83	6.93	6.62	6.95	6.91	6.91	6.85	3%	6.7	2%
Nd146	28.67	29.43	28.94	28.78	29.69	29.79	28.75	29.15	3%	28.9	1%
Sm147	6.46	6.41	6.15	6.65	6.67	7.04	6.57	6.56	8%	6.59	0%
Eu153	1.834	1.87	1.925	1.864	1.946	1.954	1.972	1.91	6%	1.97	−3%
Gd157	6.12	6.17	5.77	6.44	6.82	6.6	6.27	6.31	11%	6.71	−6%
Tb159	0.917	0.95	0.873	0.96	1.001	1.02	0.935	0.95	10%	1.02	−7%
Dy161	5.99	6.1	6.12	6.42	6.7	6.55	6.19	6.30	8%	6.44	−2%
Ho165	1.305	1.213	1.261	1.297	1.331	1.322	1.22	1.28	7%	1.27	1%
Er167	3.32	3.35	3.28	3.62	3.47	3.52	3.59	3.45	8%	3.70	−7%

During orthopyroxene analysis

	BCR2g-1	BCR2g-2	BCR2g-3	BCR2g-4	BCR2g-5	BCR2g-6	BCR2g-7	AVERAGE	External Precision (2-sigma)	GeoReM preferred value[a]	Deviate from GeoRe value
Tm169	0.479	0.473	0.498	0.461	0.532	0.506	0.498	0.49	10%	0.51	−3%
Yb173	2.91	3.34	3.19	3.53	3.47	3.47	3.33	3.32	13%	3.39	−2%
Lu175	0.477	0.477	0.475	0.532	0.518	0.491	0.52	0.50	10%	0.503	−1%
Hf178	4.7	4.66	4.76	5.07	5.16	4.99	4.93	4.90	8%	4.84	1%
Ta181	0.726	0.821	0.79	0.761	0.757	0.763	0.741	0.77	8%	0.78	−2%
Pb208	10.45	11.23	10.72	10.01	10.54	10.49	10.28	10.53	7%	11	−4%
Th232	5.76	6.01	5.81	5.89	6.28	6.23	6.01	6.00	7%	5.9	2%
U238	1.784	1.82	1.74	1.739	1.875	1.836	1.86	1.81	6%	1.69	7%

During amphibole analysis

	BCR2g-1	BCR2g-2	BCR2g-3	BCR2g-4	BCR2g-5	BCR2g-6	BCR2g-7	AVERAGE	External Precision (2-sigma)	GeoReM preferred value[a]	Deviate from GeoRe value
Li7 (ppm)	10.49	10.12	9.64	10.24	10.44	9.89	10.12	10.13	6%	9.0	13%
Be9	2.42	1.96	2.16	2.35	2.17	2.06	2.35	2.21	15%	2.30	−4%
B11	5.82	5.95	6.75	8.83	8.54	8.38	6.11	7.20	37%	6.0	20%
Na23	23710	24875	23113	24097	24309	23748	23874	23961	5%	23963	0%
Mg25	21110	21110	21110	21110	21110	21110	21110	21110	0%	21472	−2%
Al27	74689	72572	74199	74390	73720	71062	70647	73040	5%	70903	3%
Si29	273921	277914	270983	277374	274407	275149	275802	275079	2%	254157	8%
P31	1263	1409	1343	1279	1258	1287	1282	1303	8%	1615	−19%
K39	16728	17289	15420	16650	16782	16607	16730	16601	7%	14900	11%
Ca43	50561	50333	50574	49888	49596	50704	50519	50311	2%	50457	0%
Sc45	32.6	32.7	32.0	34.5	34.4	33.2	32.8	33.2	6%	33	0%
Ti49	14663	14659	14578	14303	13949	13871	13983	14287	5%	14100	1%
V51	446	452	438	426	417	426	430	434	6%	425	2%
Cr53	14.9	15.2	14.8	14.3	14.1	15.0	15.2	14.78	6%	17	−13%
Mn55	1532	1552	1514	1545	1535	1549	1540	1538	2%	1550	−1%
Fe57	79844	84431	83683	88180	88584	78603	80951	83468	9%	96386	−13%
Co59	37.1	37.3	37.3	36.8	37.0	37.1	37.5	37.2	1%	38	−2%
Ni60	11.8	11.6	11.4	11.6	11.7	11.8	11.1	11.6	4%	13	−11%
Ni62	15.1	13.6	11.5	12.0	12.6	11.3	13.1	12.7	21%	13	−2%
Cu63	17.2	17.8	16.5	17.9	18.6	19.8	18.1	18.0	12%	21	−14%
Cu65	17.8	17.6	16.7	18.0	19.3	18.3	18.4	18.0	9%	21	−14%
Zn66	143	158	149	148	142	137	141	146	9%	125	16%
Ga69	33.8	39.4	33.1	38.2	42.9	32.0	31.9	35.9	24%	23	56%
Ga71	21.7	23.8	22.8	23.3	23.5	22.5	23.1	22.9	6%	23	0%
Ge72	2.6	3.3	3.3	2.9	4.1	2.9	4.5	3.36	39%	1.5	124%
As75	0.9	1.1	1.1	1.1	1.1	0.9	1.6	1.11	44%	0.99–2.5[c]	12–56

During amphibole analysis

	BCR2g-1	BCR2g-2	BCR2g-3	BCR2g-4	BCR2g-5	BCR2g-6	BCR2g-7	AVERAGE	External Precision (2-sigma)	GeoReM preferred value[a]	Deviat from GeoRe value
Rb85	50.7	52.6	50.2	52.0	51.0	50.6	50.9	51.1	3%	47	9%
Sr86	342.5	341.89	340.23	339.8	344.57	340.61	347.76	342	2%	342	0%
Sr88	344.19	344.75	340.72	345.1	343.82	344.29	346.08	344	1%	342	1%
Y89	32.22	32.05	32.53	34.27	33.62	34.98	33.75	33.3	7%	35	−5%
Zr90	184	183	182	193	189	194	188	187	5%	184	2%
Nb93	13.69	14.07	13.92	13.58	13.31	12.89	12.96	13.5	7%	12.5	8%
Mo95	253	268	263	256	252	250	250	256	6%	270	−5%
Cd111	<0.33	0.28	<0.27	<0.211	0.318	0.155	0.179	0.233	67%	0.2	17%
Cs133	1.164	1.215	1.224	1.195	1.195	1.166	1.195	1.19	4%	1.16	3%
Ba137	684.21	688.45	679.82	688.82	676.82	672.94	693.02	683	2%	683	0%
La139	23.94	24	24.28	25.06	24.36	24.64	24.58	24.4	3%	24.7	−1%
Ce140	52.06	53	52.63	51.87	51.19	50.86	52.15	52.0	3%	53.3	−3%
Pr141	6.75	6.8	6.79	6.92	6.96	6.87	7	6.87	3%	6.7	3%
Nd146	28.83	28.66	28.99	30.01	28.99	29.35	29.69	29.2	3%	28.9	1%
Sm147	6.56	6.27	6.56	6.9	6.53	6.57	6.25	6.52	7%	6.59	−1%
Eu153	1.919	1.996	1.924	1.996	1.88	1.938	1.956	1.94	4%	1.97	−1%
Gd157	6.15	5.76	6.04	6.44	6.06	6.58	6.35	6.20	9%	6.71	−8%
Tb159	0.937	0.943	0.872	0.988	0.954	0.985	1.021	0.96	10%	1.02	−6%
Dy161	6.61	5.61	6.27	6.46	6.09	6.57	6.21	6.26	11%	6.44	−3%
Ho165	1.25	1.28	1.25	1.203	1.265	1.318	1.294	1.27	6%	1.27	0%
Er167	3.44	3.78	3.37	3.38	3.44	3.66	3.49	3.51	9%	3.70	−5%
Tm169	0.493	0.487	0.472	0.484	0.497	0.549	0.49	0.50	10%	0.51	−3%
Yb173	3.34	3.05	3.34	3.04	3.5	3.79	3.36	3.35	15%	3.39	−1%
Lu175	0.51	0.465	0.496	0.494	0.489	0.558	0.511	0.50	11%	0.503	0%
Hf178	4.61	4.83	4.82	4.97	5.11	4.98	4.84	4.88	7%	4.84	1%
Ta181	0.728	0.742	0.721	0.78	0.783	0.777	0.754	0.76	7%	0.78	−3%
Pb208	10.65	11.08	11.13	10.87	11.03	10.22	10.57	10.79	6%	11	−2%
Th232	5.86	5.66	5.93	5.95	6.06	6.08	5.99	5.93	5%	5.90	1%
U238	1.955	2.012	1.868	1.803	1.813	1.852	1.827	1.88	8%	1.69	11%

During phlogopite analysis

	BCR2g-1	BCR2g-2	BCR2g-3	BCR2g-4	BCR2g-5	BCR2g-6	BCR2g-7	AVERAGE	External Precision (2-sigma)	GeoReM preferred value[a]	Deviat from GeoRe value
Li7 (ppm)	9.91	9.64	9.92	10.12	9.81	10.32	9.95	5%	9.0	11%	9.60
Be9	2.36	2.22	2.31	2.02	2.00	1.99	2.15	16%	2.3	−7%	n.d.
B11	7.34	7.05	8.38	8.62	6.50	8.80	7.78	24%	6.0	30%	n.d.
Na23	23875	23390	24259	23611	24099	24540	23962	4%	23963	0%	2340
Mg25	21110	21110	21110	21110	21110	21110	21110	0%	21472	−2%	2111
Al27	74626	73985	72111	70766	70909	72093	72415	4%	70903	2%	7196

During phlogopite analysis

	BCR2g-1	BCR2g-2	BCR2g-3	BCR2g-4	BCR2g-5	BCR2g-6	BCR2g-7	AVERAGE	External Precision (2-sigma)	GeoReM preferred value[a]	Deviate from GeoRe value
Si29	279893	270416	280590	263227	279440	270338	273984	5%	254157	8%	25406
P31	1415	1235	1323	1333	1268	1331	1318	9%	1615	−18%	1615
K39	16710	16354	17017	16754	16799	17178	16802	3%	14900	13%	14900
Ca43	51255	49613	50635	50805	50492	50845	50608	2%	50457	0%	50886
Sc45	36.1	36.9	33.5	33.3	31.4	33.2	34.1	12%	33	3%	33.0
Ti49	14539	14275	14030	13801	14053	14011	14118	4%	14100	0%	13700
V51	438	414	430	424	436	434	429	4%	425	1%	414
Cr53	14.6	15.6	14.1	15.5	15.6	14.3	14.9	9%	17	−12%	n.d.
Mn55	1541	1519	1556	1524	1553	1547	1540	2%	1550	−1%	1549
Fe57	71013	84632	82046	83405	84700	85342	81856	13%	96386	−15%	97164
Co59	38.6	35.6	38.0	37.2	38.2	37.7	37.5	6%	38	−1%	35.8
Ni60	11.4	11.2	11.9	11.8	11.7	11.7	11.6	5%	13	−11%	10.8
Ni62	14.4	14.8	12.3	11.9	11.8	14.2	13.2	21%	13	2%	10.8
Cu63	17.8	15.5	18.3	19.5	18.5	17.1	17.8	16%	21	−15%	19.4
Cu65	17.9	16.3	17.9	20.8	18.2	18.3	18.2	16%	21	−13%	19.4
Zn66	162	138	139	141	146	137	144	13%	125	15%	147
Ga69	39.5	49.6	32.7	30.8	32.0	31.7	36.1	41%	23	57%	22.7
Ga71	23.9	22.3	23.1	22.7	22.8	23.7	23.1	5%	23	0%	22.7
Ge72	3.3	2.6	2.6	3.3	4.2	3.6	3.26	39%	1.5	117%	n.d.
As75	1.1	1.3	1.0	8.3	4.5	6.9	3.84	168%	54–289%	n.d.	n.d.
Rb85	51.4	50.0	51.7	50.9	50.5	51.8	51.0	3%	47	9%	49.0
Sr86	341.13	342.55	344.82	345.24	343.89	351.1	345	2%	342	1%	342
Sr88	345.96	340.98	348.21	347.02	345.21	349.39	346	2%	342	1%	342
Y89	33.11	32.71	35.32	34.98	33.66	35.56	34.2	7%	35	−2%	35.3
Zr90	189	186	196	194	186	200	192	6%	184	4%	194
Nb93	14.19	13.99	13.11	13.19	13.29	13.16	13.5	7%	13	8%	12.8
Mo95	263	237	252	246	250	253	250	7%	270	−7%	244
Cd111	<0.30	0.303	<0.138	0.227	<0.153	0.342	0.291	40%	0.20	45%	n.d.
Cs133	1.176	1.209	1.201	1.196	1.224	1.281	1.21	6%	1.16	5%	1.13
Ba137	694.59	690.8	687.92	679.33	695.41	687.6	689	2%	683	1%	660
La139	24.83	24.31	24.82	24.86	24.48	25.5	24.8	3%	24.7	0%	24.5
Ce140	51.59	51.52	51.78	51.35	53.16	52.33	52.0	3%	53.3	−3%	50.5
Pr141	6.67	6.77	6.87	6.81	6.88	6.99	6.83	3%	6.7	2%	6.8
Nd146	29.63	28.76	30.03	29.73	29.22	29.94	29.6	3%	28.9	2%	29
Sm147	6.49	6.31	6.39	6.76	6.61	6.6	6.53	5%	6.59	−1%	6.6
Eu153	1.922	1.978	2.042	1.929	1.885	2.014	1.96	6%	1.97	0%	1.92
Gd157	6.49	6.56	6.66	6.6	6.35	6.72	6.56	4%	6.71	−2%	6.5
Tb159	0.954	0.861	1.031	1.005	0.95	1.041	0.97	14%	1.02	−5%	1.06
Dy161	6.33	6.32	6.72	6.56	6.22	6.83	6.50	8%	6.44	1%	6.5
Ho165	1.274	1.218	1.378	1.204	1.3	1.369	1.29	11%	1.27	2%	1.31

During phlogopite analysis

	BCR2g-1	BCR2g-2	BCR2g-3	BCR2g-4	BCR2g-5	BCR2g-6	BCR2g-7	AVERAGE	External Precision (2-sigma)	GeoReM preferred value[a]	Deviat from GeoRe value
Er167	3.34	3.37	3.76	3.79	3.48	3.71	3.58	11%	3.70	−3%	3.6
Tm169	0.499	0.466	0.523	0.551	0.499	0.507	0.51	11%	0.51	0%	n.d.
Yb173	3.4	3.27	3.53	3.56	3.17	3.63	3.43	10%	3.39	1%	3.5
Lu175	0.498	0.476	0.529	0.508	0.482	0.509	0.50	8%	0.503	−1%	0.51
Hf178	4.89	4.54	4.88	5.16	4.98	5.19	4.94	10%	4.84	2%	5
Ta181	0.766	0.767	0.806	0.787	0.765	0.781	0.78	4%	0.78	0%	0.78
Pb208	11.14	10.07	10.47	11.41	10.51	11.1	10.78	9%	11	−2%	11.5
Th232	5.93	5.88	6.14	6.03	5.91	6.22	6.02	5%	5.9	2%	6.1
U238	1.886	1.719	1.823	1.771	1.834	1.94	1.83	9%	1.69	8%	1.73

[a] GeoReM preferred values (www.georem.mpch-mainz.gwdg.de/)

[b] Si, Al, P, Ca were determined by EPMA, Li and Tb by solution ICP-MS

[c] No preferred value given by GeoReM. Instead the reported As range is shown.

Table A1-B -

Assessment of the accuracy and precision of the bulk-rock major and minor element data generated during this study.

Bulk-rock sample duplicate analyses

	GV1285	GV1285 - duplicate	Ext. Precision (2-sigma)	BO1251	BO1251 - duplicate	Ext. Precision (2- sigma)
Al2O3 (wt %)	4.21	4.19	1%	703%	702%	0%
CaO	3.165	3.174	0%	454%	452%	1%
Fe2O3	45.78	45.7	0%	1426%	1420%	1%
K2O	0.09	0.09	0%	22%	22%	0%
MgO	2.25	2.25	0%	3024%	3027%	0%
MnO	0.047	0.049	6%	20%	19%	3%
Na2O	0.22	0.22	0%	102%	102%	0%
P2O5	0.007	0.007	0%	12%	11%	2%
SiO2	11.45	11.43	0%	4153%	4143%	0%
TiO2	0.16	0.16	0%	90%	90%	0%

Bulk-rock duplicate analyses of reference materials

	OKUM-1	OKUM-2	OKUM-3	Ext. Precision (2-sigma)	IAG preliminary certified value	Deviation of OKUM average from IAG value
Al2O3 (wt %)	7.95	7.98	8.02	1%	7.973	0%
CaO	7.877	7.922	7.939	1%	7.859	1%
Fe2O3	11.76	11.81	11.83	1%	11.81	0%
K2O	0.07	0.05	0.05	41%	0.045	26%
MgO	21.47	21.59	21.7	1%	21.27	1%
MnO	0.183	0.182	0.182	1%	0.181	1%

Na2O	1.08	1.10	1.11	3%	1.14	−4%
P2O5	0.024	0.023	0.024	5%	0.027	−12%
SiO2	43.84	44.01	44.26	1%	44.113	0%
TiO2	0.37	0.38	0.37	3%	0.381	−2%

Bulk-rock duplicate analyses of reference materials

	BHVO-2	**GeoReM preferred value**	**Deviation from GeoReM value***	**BIR-1**	**GeoReM preferred value**	**Deviation from GeoReM value***
Al2O3 (wt %)	13.67	13.5	1.3%	15.66	15.4	1.7%
CaO	11.556	11.4	1.4%	13.482	13.4	0.6%
Fe2O3	12.43	12.3	1.1%	11.44	11.3	1.2%
K2O	0.51	0.52	−1.9%	0.02	0.03	−33.3%
MgO	7.36	7.23	1.8%	9.79	9.7	0.9%
MnO	0.171	0.17	0.6%	0.18	0.176	0.6%
Na2O	2.21	2.22	−0.5%	1.79	1.81	−1.1%
P2O5	0.275	0.27	1.9%	0.02	0.027	−18.5%
SiO2	50.06	49.9	0.3%	47.85	47.7	0.3%
TiO2	2.74	2.73	0.4%	0.96	0.97	−1.0%

Table A1-C -

Assessment of the accuracy and precision of the bulk-rock trace element data generated during this study.

Reference materials

	AGV-2	**GeoReM preferred value**	**Deviation from GeoReM value***	**BHVO-2**	**GeoReM preferred value**	**Deviation from GeoReM value***	**OKUM-1**	**OKUM-2**	**Ext. Precision (2-sigma)**	**IAG preliminary certified value**	**Deviation of OKUM averag from IAG valu**
Ba (ppm)	1134.4	1130	0.4%	132.2	131	1%	6.2	6.1	2%	6.38	−4%
Be	2.03	2.3	−12%	1.09	1	9%	0.11	0.09	28%	0.066	52%
Bi	0.08	0.04 to 0.07	14% to 100%	0.03	0.01–0.03	0% to 200%	0.01	0.13	242%	n.d.	−
Cd	0.102	0.063 to 0.25	−59% to 62%	0.118	0.06	97%	0.062	0.057	12%	n.d.	−
Ce	69.44	68.6	1%	37	37.5	−1%	1.28	1.17	13%	1.271	−4%
Co	15.87	16	−1%	46.54	45	3%	90.93	90.63	0%	89	2%
Cr	17	16	6%	302	280	8%	2524	2499	1%	2461	2%
Cs	1.13	1.2	−6%	0.096	0.1	−4%	0.183	0.181	2%	0.184	−1%
Cu	52.3	53	−1%	134.3	127	6%	49.1	46	9%	43	11%
Dy	3.56	3.47	3%	5.532	5.31	4%	1.549	1.571	2%	1.609	−3%
Er	1.863	1.81	3%	2.586	2.54	2%	1.018	1.046	4%	1.042	−1%
Eu	1.5038	1.53	−2%	2.0826	2.07	1%	0.2868	0.2961	5%	0.303	−4%
Ga	19.7	20	−2%	21.12	22	−4%	8.75	8.62	2%	8.81	−1%

Reference materials

	AGV-2	GeoReM preferred value	Deviation from GeoReM value*	BHVO-2	GeoReM preferred value	Deviation from GeoReM value*	OKUM-1	OKUM-2	Ext. Precision (2-sigma)	IAG preliminary certified value	Deviation of OKUM averag from IAG valu
Gd	4.595	4.52	2%	6.514	6.24	4%	1.237	1.204	4%	1.141	7%
Hf	5.13	5	3%	4.44	4.36	2%	0.57	0.6	7%	0.548	7%
Ho	0.6674	0.65	3%	0.9755	0.98	0%	0.3369	0.3361	0%	0.355	−5%
In	0.0452	0.0452 to 0.05	−10% to 0%	0.0858	0.082–0.19	−55% to 5%	0.034	0.0355	6%	n.d.	–
La	38.29	37.9	1%	15.42	15.2	1%	0.46	0.42	13%	0.415	6%
Li	9.1	11	−17%	4.5	4.8	−6%	4.2	4.3	3%	4.38	−3%
Lu	0.2487	0.247	1%	0.2735	0.274	0%	0.1472	0.146	1%	0.149	−2%
Mo	2.24	1.83–2.26	−1% to 22%	4.29	4	7%	0.37	0.27	44%	n.d.	–
Nb	13.279	14.5	−8%	17.398	18.1	−4%	0.332	0.342	4%	0.346	−3%
Nd	31.08	30.5	2%	24.74	24.5	1%	1.52	1.41	11%	1.49	−2%
Ni	19.2	20	−4%	122.6	119	3%	896.7	902.1	1%	884	2%
Pb	12.9	13.2	−2%	1.5	1.6	−6%	0.3	0.2	57%	0.265	−6%
Pr	8.186	7.84	4%	5.365	5.35	0%	0.258	0.25	4%	0.239	6%
Rb	64.2	66.3	−3%	9.07	9.11	0%	0.88	0.9	3%	0.96	−7%
Sb	0.45	0.385–0.6	−25% to 17%	0.11	0.13	−15%	0.08	0.09	17%	0.077	10%
Sc	12.8	13	−2%	32.9	32	3%	29.2	29	1%	28	4%
Sm	5.656	5.49	3%	6.169	6.07	2%	0.7	0.705	1%	0.712	−1%
Sn	1.8	2.3	−22%	2.61	1.7	54%	0.17	0.23	42%	0.25	−20%
Sr	640.4	661	−3%	388.1	369	5%	15.7	15.6	1%	16.1	−3%
Ta	0.821	0.87	−6%	1.115	1.14	−2%	0.02	0.019	7%	0.026	−25%
Tb	0.6078	0.64	−5%	0.9318	0.92	1%	0.22	0.2222	1%	0.225	−2%
Th	6.277	6.1	3%	1.175	1.22	−4%	0.028	0.029	5%	0.031	−8%
Ti	5912	6295	−6%	16238	16300	0%	2124	2133	1%	2284	−7%
Tl	0.265	0.27	−2%	0.019	0.011–0.08	−76% to 73%	0.014	0.015	10%	0.015	−3%
Tm	0.2537	0.26	−2%	0.3364	0.33	2%	0.145	0.148	3%	0.154	−5%
U	1.895	1.86	2%	0.42	0.403	4%	0.012	0.013	11%	0.014	−11%
V	118.4	122	−3%	319.9	317	1%	173.3	170.2	3%	167	3%
W	0.51	0.439–0.56	−9% to 16%	0.22	0.21	5%	0.09	0.06	57%	n.d.	–
Y	19.16	19	1%	25.83	26	−1%	9.17	9.33	2%	9.27	0%
Yb	1.635	1.62	1%	2.009	2	0%	0.973	0.989	2%	1.02	−4%
Zn	84	86	−2%	98	103	−5%	63	63	0%	61.2	3%
Zr	230	230	0%	170	172	−1%	18	19	8%	17.4	6%

Pipe samples

	GV1282	GV1282 - duplicate	Ext. Precision (2-sigma)	VM1317	VM1317 - duplicate	Ext. Precision (2-sigma)	BO1242	BO1242 - duplicate	Ext. Precision (2-sigma)	BO1260	BO1260 - duplicate	Pr s
Ba (ppm)	1.8	1.7	8%	17.1	17.2	1%	179.5	176.4	2%	10201.2	10256.3	
Be	0.02	0.03	57%	0.17	0.14	27%	0.92	0.88	6%	0.37	0.34	
Bi	0.91	0.88	5%	0.29	0.28	5%	0.59	0.35	72%	0.05	0.02	
Cd	0.083	0.077	11%	0.156	0.159	3%	0.425	0.442	6%	0.059	0.053	
Ce	0.14	0.13	10%	2.15	2.11	3%	13.93	13.61	3%	62.11	61.74	
Co	616.86	603.99	3%	276.34	276.8	0%	115.31	112.32	4%	10.8	11.02	
Cr	134	130	4%	2079	2136	4%	938	906	5%	5	5	
Cs	0.009	0.009	0%	0.054	0.052	5%	0.356	0.35	2%	0.198	0.194	
Cu	387.4	381.5	2%	2217.8	2188.7	2%	1075.9	1042.7	4%	5.8	5.5	
Dy	0.007	0.009	35%	0.785	0.796	2%	2.25	2.186	4%	3.079	3.104	
Er	0.006	0.006	0%	0.465	0.448	5%	1.356	1.295	7%	1.459	1.44	
Eu	0.0074	0.009	28%	0.2397	0.2427	2%	0.9273	0.9108	3%	7.3876	7.5676	
Ga	1.55	1.53	2%	5.92	6.09	4%	11.93	11.22	9%	19.81	19.77	
Gd	0.01	0.012	26%	0.75	0.746	1%	2.281	2.198	5%	4.904	4.969	
Hf	0.02	0.02	0%	0.42	0.4	7%	1.45	1.45	0%	3.54	3.56	
Ho	0.0022	0.0018	28%	0.154	0.1566	2%	0.446	0.4513	2%	0.5753	0.5627	
In	0.0047	0.0049	6%	0.0395	0.0391	1%	0.0762	0.076	0%	0.0168	0.0173	
La	0.07	0.07	0%	0.83	0.82	2%	5.92	5.85	2%	29.67	28.96	
Li	0.3	0.3	0%	3.3	3.4	4%	2.9	2.8	5%	3.7	3.8	
Lu	0.0009	0.0007	35%	0.0599	0.0597	0%	0.1863	0.1921	4%	0.1446	0.1456	
Mo	0.2	0.21	7%	0.14	0.13	10%	0.6	0.61	2%	0.17	0.16	
Nb	0.035	0.04	19%	0.223	0.234	7%	3.116	3.017	5%	3.566	3.92	
Nd	0.07	0.07	0%	1.9	1.98	6%	9.12	8.94	3%	38.06	37.69	
Ni	50340	49562	2%	4142.9	4138.2	0%	2139.7	2079.5	4%	2.7	2.6	
Pb	2.8	2.8	0%	3.9	3.9	0%	5	4.7	9%	6.5	6.5	
Pr	0.016	0.014	19%	0.354	0.357	1%	2.016	1.932	6%	8.431	8.343	
Rb	0.07	0.07	0%	0.42	0.44	7%	6.5	6.16	8%	27.5	27.68	
Sb	0.02	0.02	0%	0.02	0.02	0%	0.06	0.07	22%	0.02	0.01	
Sc	0.3	0.4	40%	17.2	17.1	1%	25.5	24.3	7%	7.9	8	
Sm	0.02	0.014	50%	0.655	0.614	9%	2.135	2.111	2%	6.251	6.2	
Sn	0.02	0.02	0%	0.03	0.13	177%	0.97	0.93	6%	0.09	0.09	
Sr	0.7	0.7	0%	107.3	107.4	0%	198	193.2	3%	630.4	638.4	
Ta	bdl.	bdl.	–	0.016	0.016	0%	0.194	0.186	6%	0.112	0.123	
Tb	0.0017	0.002	23%	0.1213	0.1207	1%	0.35	0.3506	0%	0.5725	0.5685	
Th	0.009	0.01	15%	0.059	0.062	7%	0.614	0.596	4%	0.471	0.476	
Ti	174	167	6%	2121	2113	1%	4170	3997	6%	8971	8960	
Tl	0.058	0.055	8%	0.029	0.031	9%	0.053	0.051	5%	0.097	0.097	
Tm	0.001	0.001	0%	0.061	0.0638	6%	0.1954	0.1922	2%	0.1725	0.1742	
U	0.005	0.005	0%	0.019	0.018	8%	0.201	0.186	11%	0.324	0.334	
V	26	24.4	9%	180.6	182	1%	174.1	166.1	7%	120.6	121.4	

Pipe samples

	GV1282	GV1282 - duplicate	Ext. Precision (2-sigma)	VM1317	VM1317 - duplicate	Ext. Precision (2-sigma)	BO1242	BO1242 - duplicate	Ext. Precision (2-sigma)	BO1260	BO1260 - duplicate	Pr s
W	0.03	0.02	57%	0.87	0.88	2%	0.22	0.21	7%	0.02	0.02	
Y	0.04	0.04	0%	4.05	4.02	1%	12.38	11.94	5%	15.26	15.21	
Yb	0.006	0.005	26%	0.411	0.396	5%	1.286	1.224	7%	1.001	1.007	
Zn	7	8	19%	109	112	4%	169	161	7%	66	65	
Zr	1	1	0%	14	13	10%	65	64	2%	228	229	

References

References

Arevalo R Jr; McDonough WF; Piccoli PM (2011): In Situ Determination of First-Row Transition Metal, Ga and Ge Abundances in Geological Materials via Medium-Resolution LA-ICP-MS. Geostandards and Geoanalytical Research v. 35, no. 2, pp. 253–273.

Jochum KP, Nohl U, Herwig K, Lammel E, Stoll B, and Hofmann AW, 2005, GeoReM: A New Geochemical Database for Reference Materials and Isotopic Standards: Geostandards and Geoanalytical Research, v. 29, p. 333–338.

Norman MD, Griffin WL, Pearson NJ, Garcia MO, and O'Reilly SY, (1998): Quantitative analysis of trace element abundances in glasses and minerals: a comparison of laser ablation inductively coupled plasma mass spectrometry, solution inductively coupled plasma mass spectrometry, proton microprobe and electron microprobe data: Journal of Analytical Atomic Spectrometry, v. 13, p. 477–482.

Appendix 2 -: Full mineral chemistry data set (olivine)

Bec d'Ovaga - Olivine electron microprobe and LA-ICP-MS analyses

Electron microprobe data					
DataSet/Point	**BO1-ol-1**	**BO1-ol-2**	**BO1-ol-3**	**BO1-ol-4**	**BO1-ol-5**
SiO2 (wt%)	40.06	39.90	39.96	40.40	40.03
TiO2	0.00	0.00	0.01	0.05	0.00
AI2O3	0.00	0.00	0.00	0.03	0.00
Cr2O3	0.00	0.00	0.01	0.01	0.00
FeO	14.70	14.36	14.77	14.66	14.56
MnO	0.25	0.22	0.20	0.26	0.26
MgO	46.54	46.31	46.68	46.18	47.02
CaO	0.00	0.00	0.00	0.00	0.00
Na2O	0.01	0.00	0.01	0.03	0.02
K2O	0.01	0.00	0.01	0.00	0.01
NiO	0.07	0.09	0.14	0.11	0.20
P2O5	n.d.	n.d.	n.d.	n.d.	n.d.
CI	0.01	0.00	0.00	0.00	0.00
TotaI	101.66	100.89	101.79	101.74	102.10

Mg-number	84.9	85.2	84.9	84.9	85.2
Laser Ablation ICP-MS data					
GLITTER!: Trace Element Concentrations MDL filtered.					
EIement	**BO1-ol-1**	**BO1-ol-2**	**BO1-ol-3**	**BO1-ol-4**	**BO1-ol-5**
Li7 (ppm)	5.04	6.94	5.96	7.31	6.13
Be9	<0.0205	<0.0140	0.02	<0.0232	0.03
B11	5.45	4.74	4.33	5.03	4.88
Al27	3.09	5.04	6.28	4.41	9.89
Si29	197618	201029	186392	200171	203488
P31	65.6	102	88.9	107	75.4
Ca42	<37.83	<36.64	47.3	<41.75	<38.94
Ca43	<24.24	33.5	22.2	<28.24	<28.08
Sc45	5.36	5.42	5.22	5.35	5.38
Ti49	8.33	9.71	16.4	8.15	9.22
V51	0.27	0.32	0.32	0.23	0.36
Cr53	2.07	2.01	1.82	1.06	3.32
Mn55	2069	1984	1963	2047	2143
Fe57	71798	71567	71127	74112	75654
Co59	82.1	83.8	73.7	84.3	92.7
Ni60	897	1071	776	1027	1104
Ni62	892	1049	805	1002	1091
Cu63	<0.088	<0.079	<0.043	0.66	<0.077
Cu65	<0.120	<0.119	0.08	0.62	0.26
Zn66	33.16	33.36	17.41	27.10	37.16
Ga69	<0.0112	0.02	0.03	<0.0127	<0.0132
Ga71	<0.0121	<0.0221	0.02	0.02	<0.022
Ge72	2.50	2.32	2.18	2.13	2.44
Y89	0.01	0.01	0.01	0.01	0.00
Zr90	0.10	0.02	0.06	0.02	0.03
Nb93	0.01	0.00	<0.00269	0.00	0.00
Mo95	<0.0059	0.01	<0.0027	<0.0086	0.01
Hf178	0.00	0.00	<0.00	<0.0077	0.00
Ta181	<0.00274	0.00	<0.00	0.00	0.00

Appendix A3 –: Core-rim comparison of the chemistry of olivine, orthopyroxene, amphibole and phlogopite from the Valmaggia pipe

The plots illustrate the absence of significant systematic core-rim zonation patterns in the investigated mineral phases. All values are normalized to the composition of the primitive mantle (McDonough and Sun, 1995).

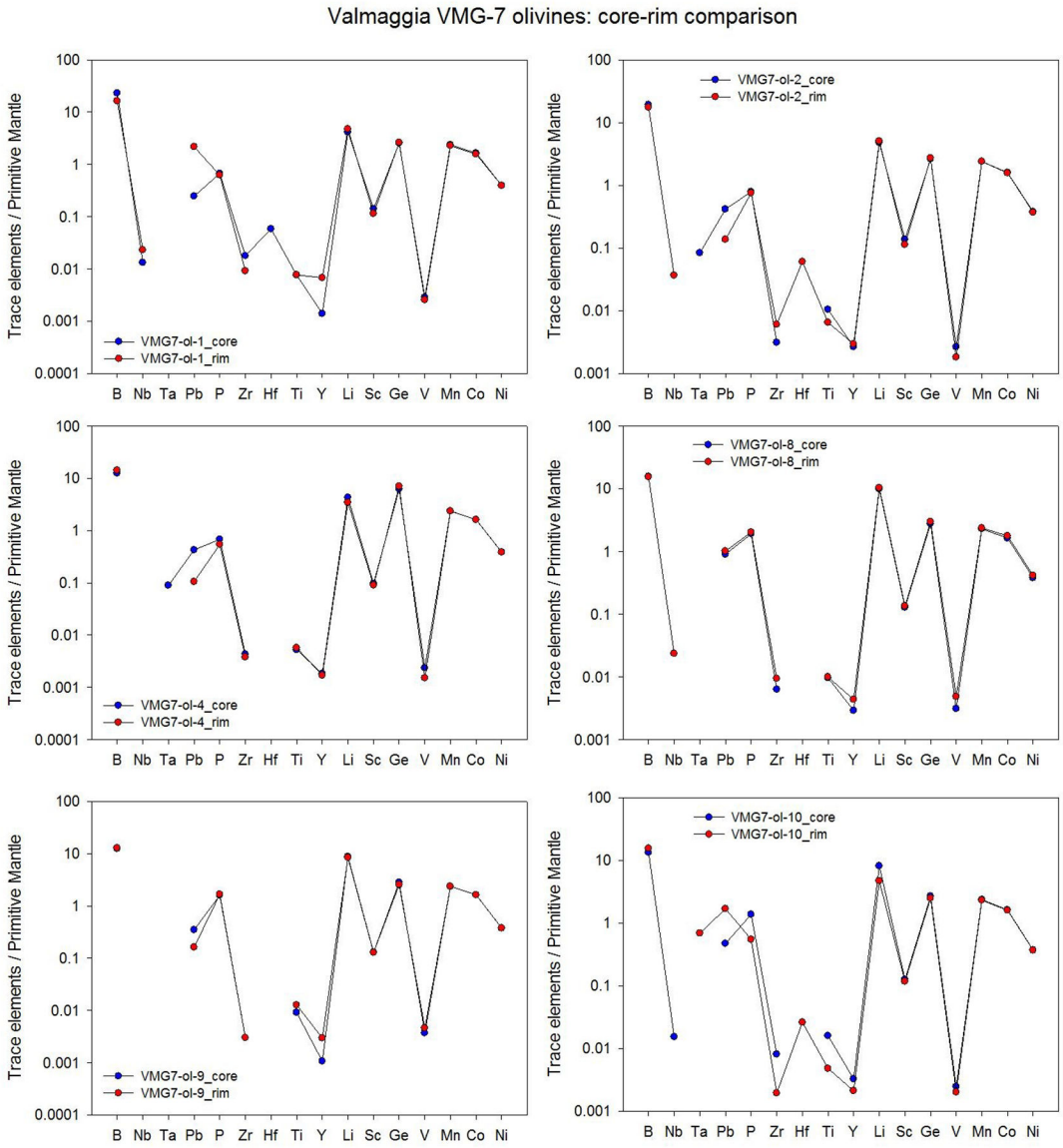

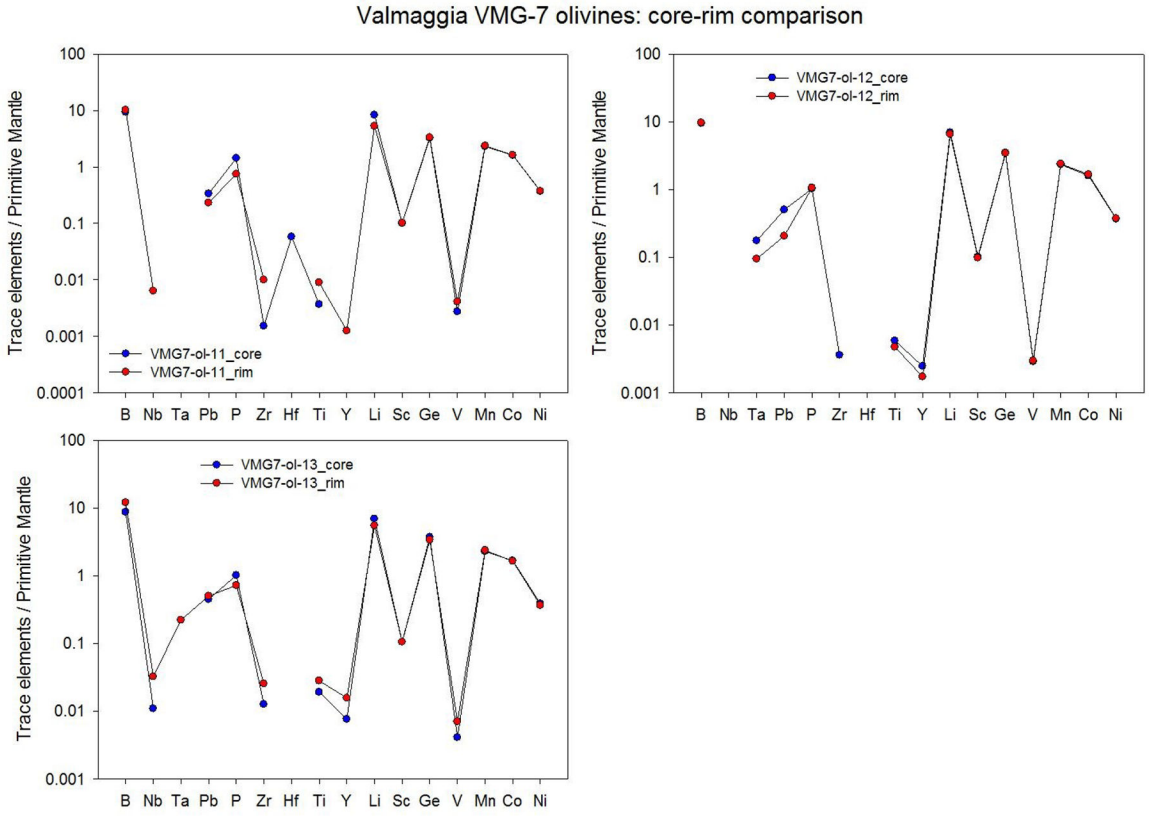

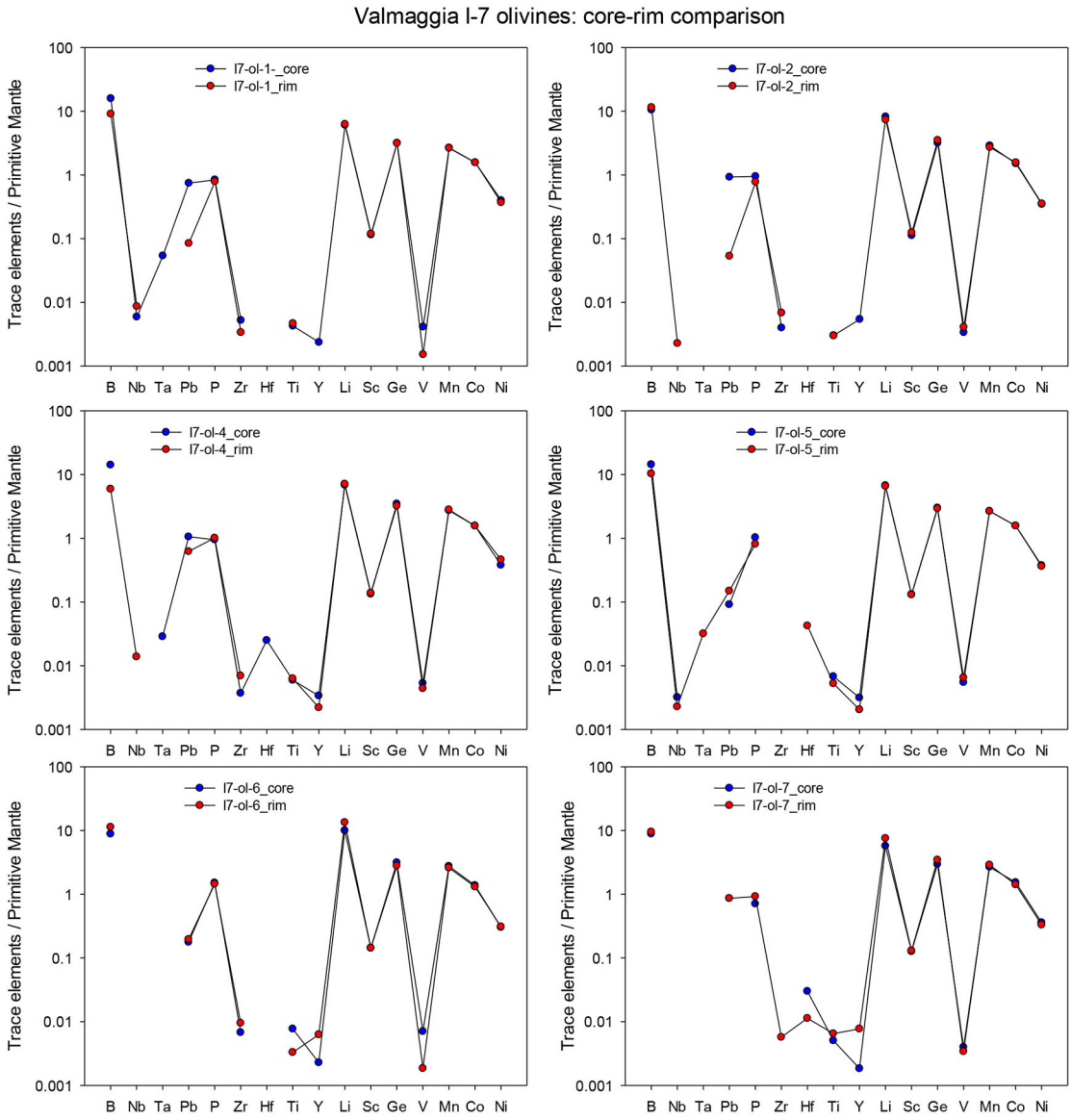

Valmaggia VMG-7 (centre of pipe) opx: core-rim comparison

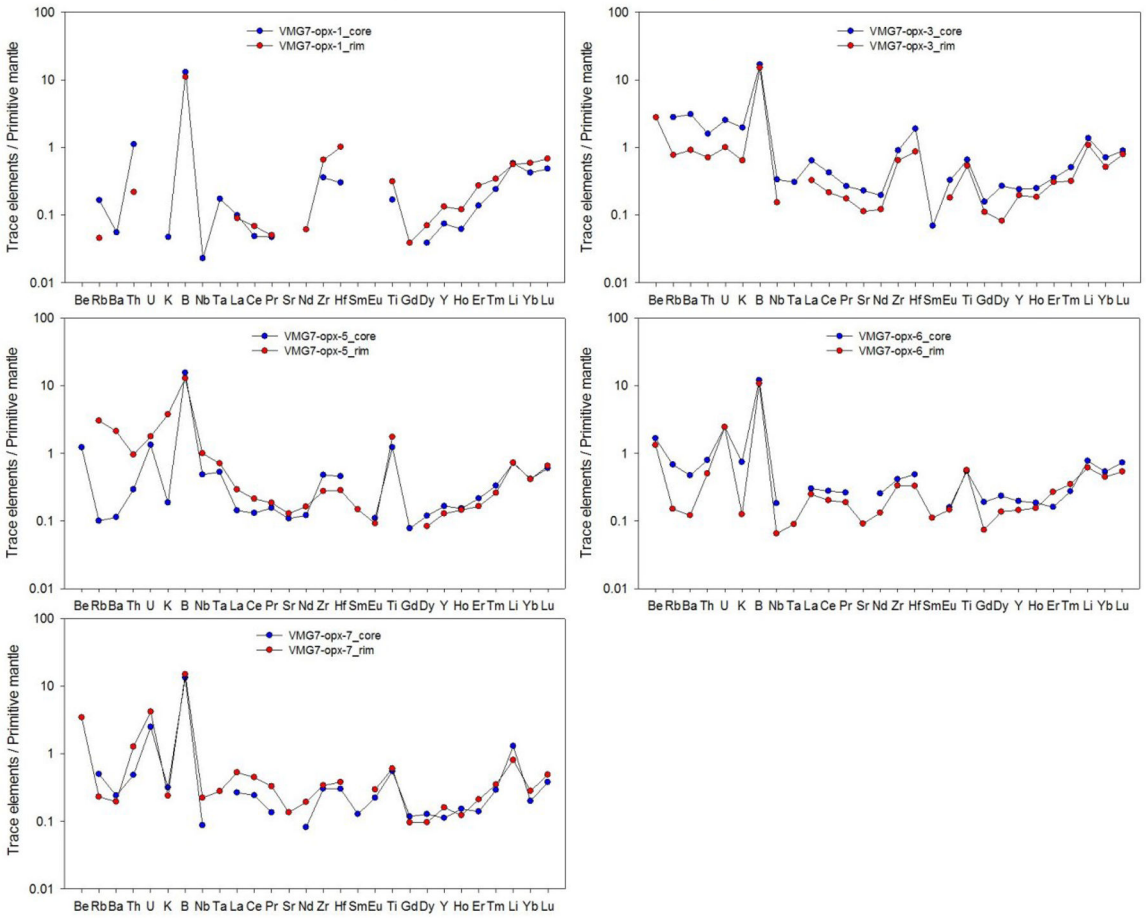

Valmaggia I-7 (rim of pipe) opx: core-rim comparison

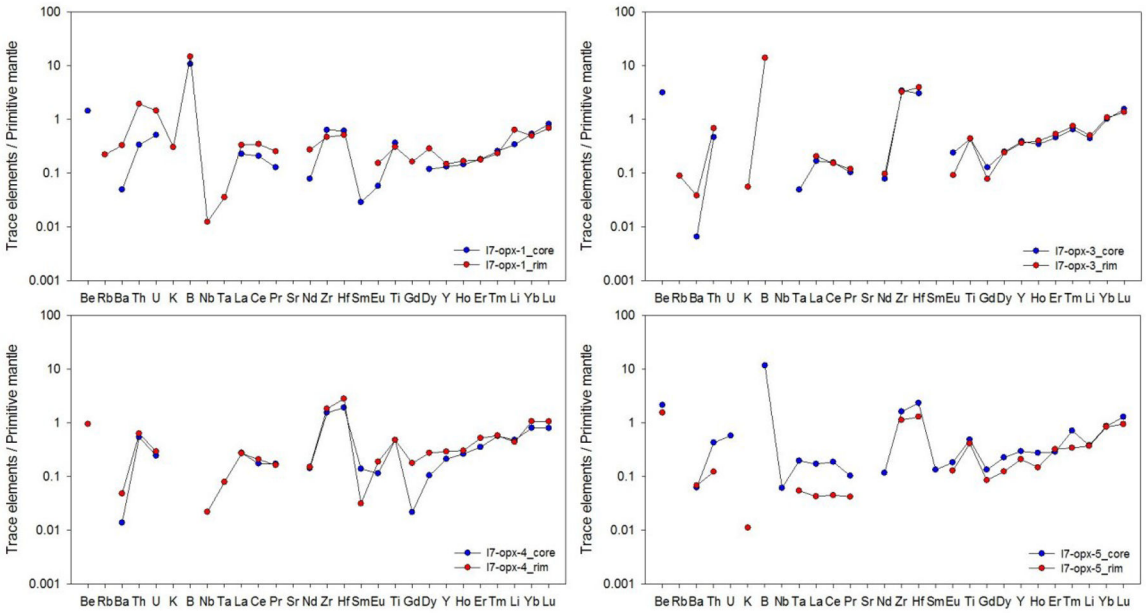

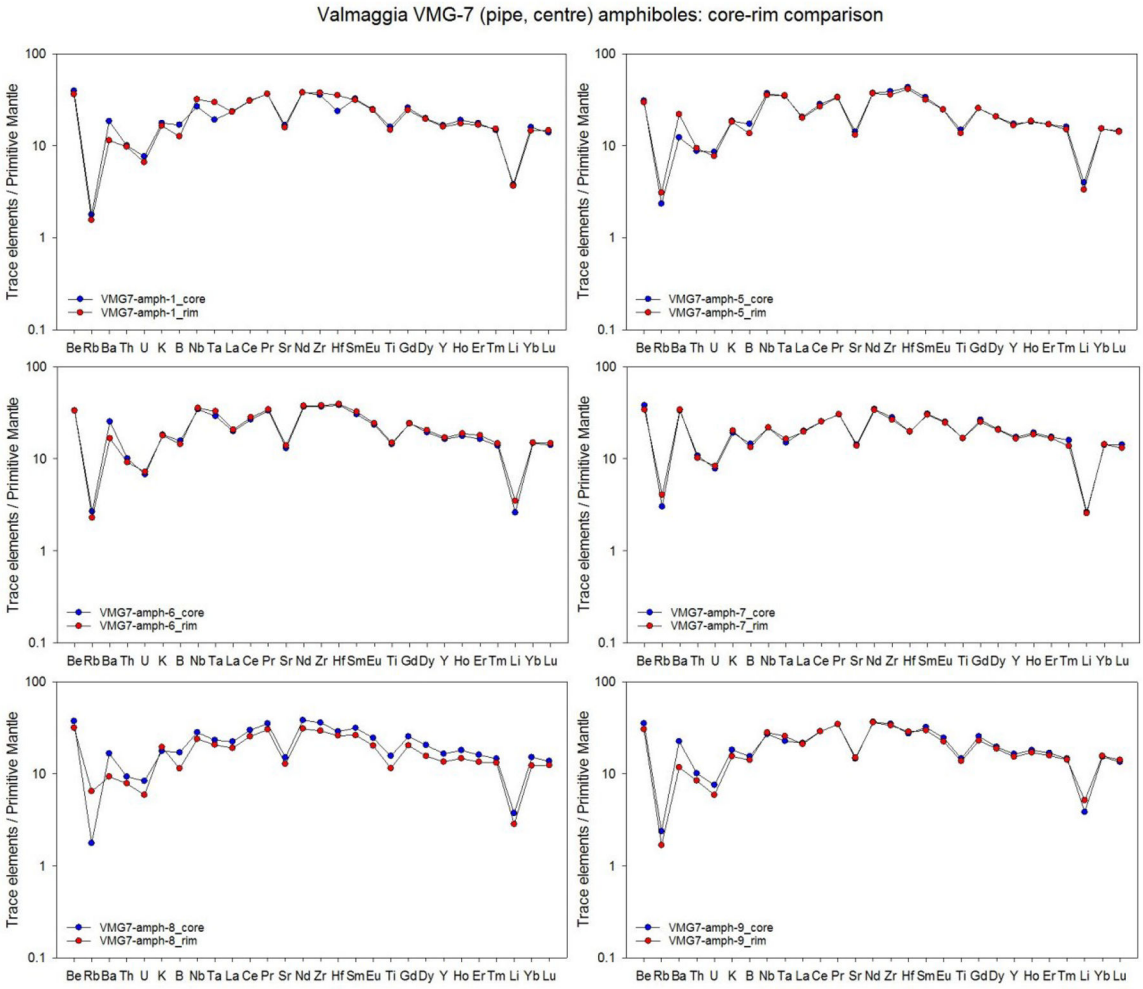

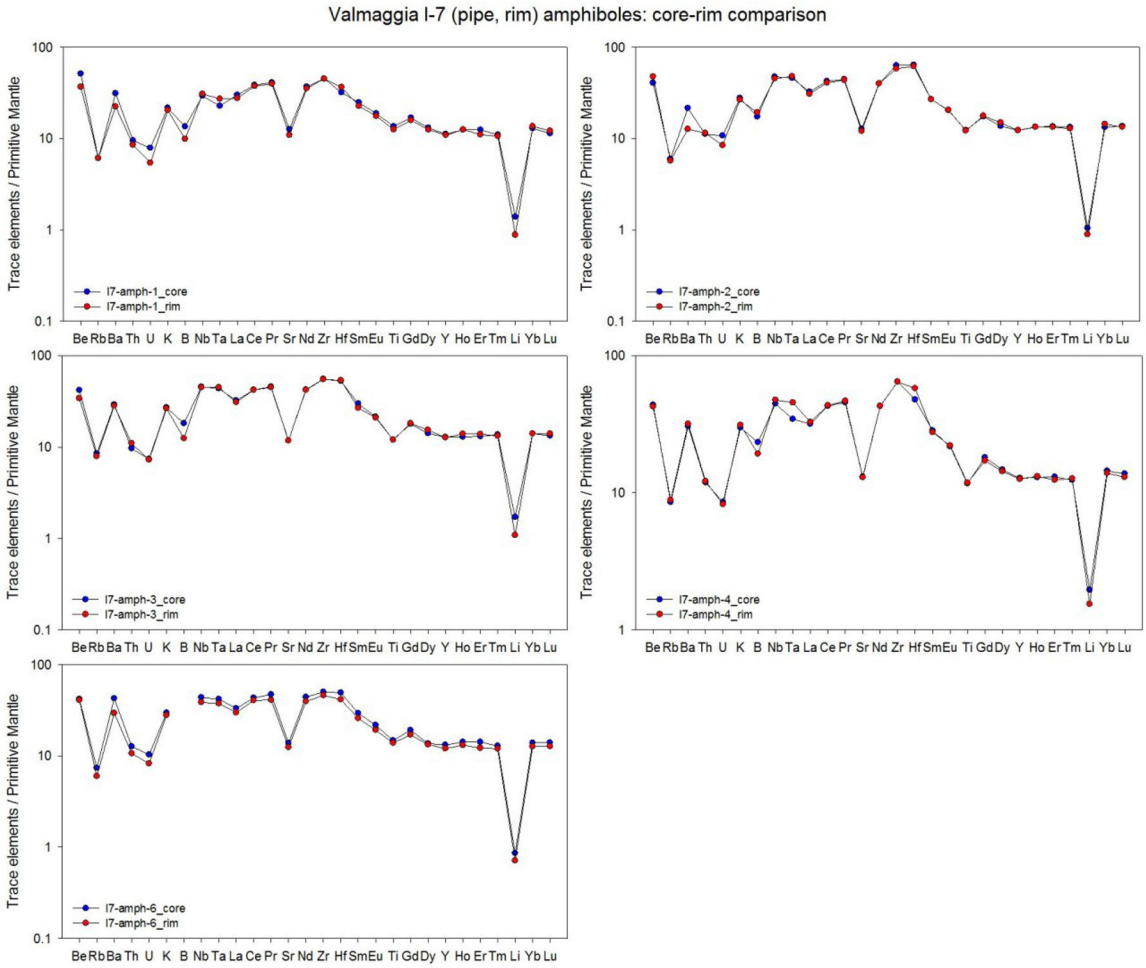

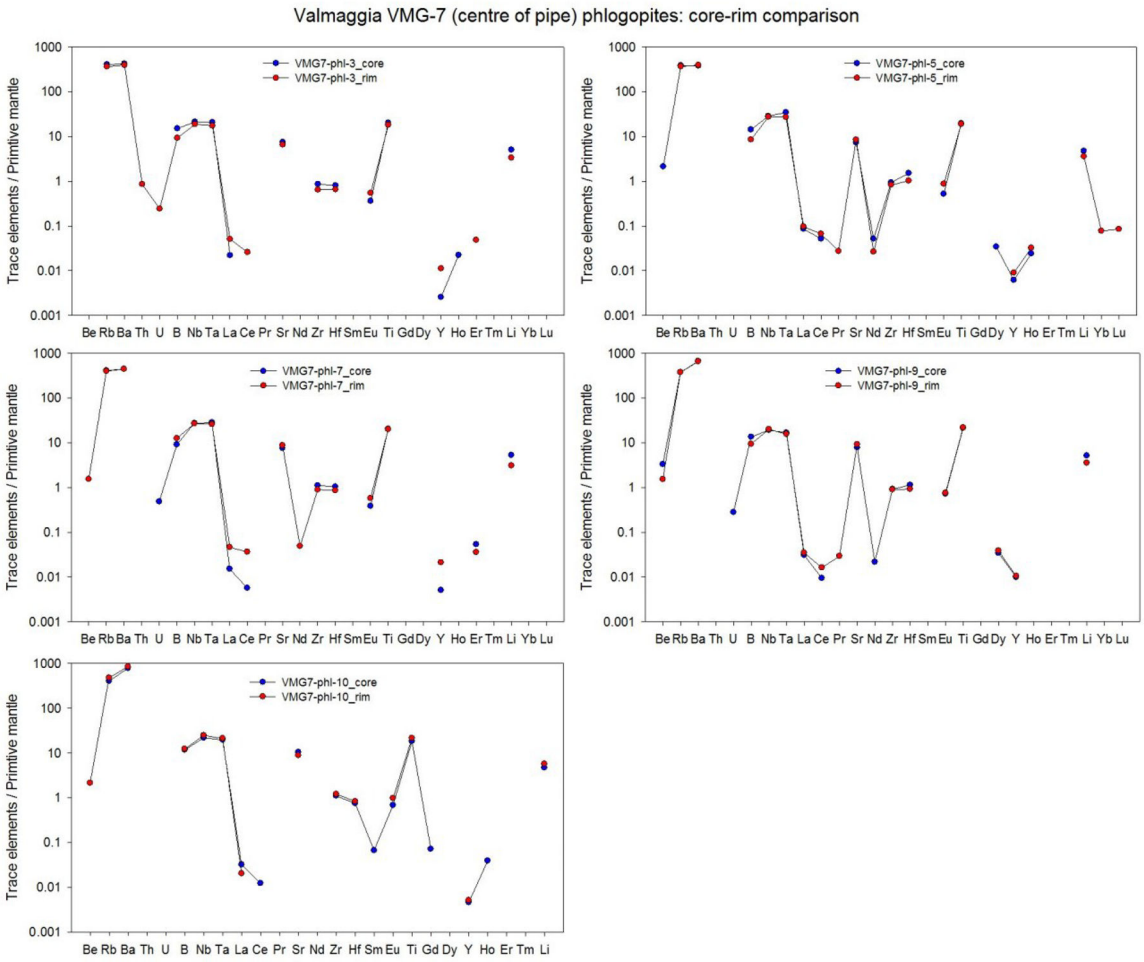

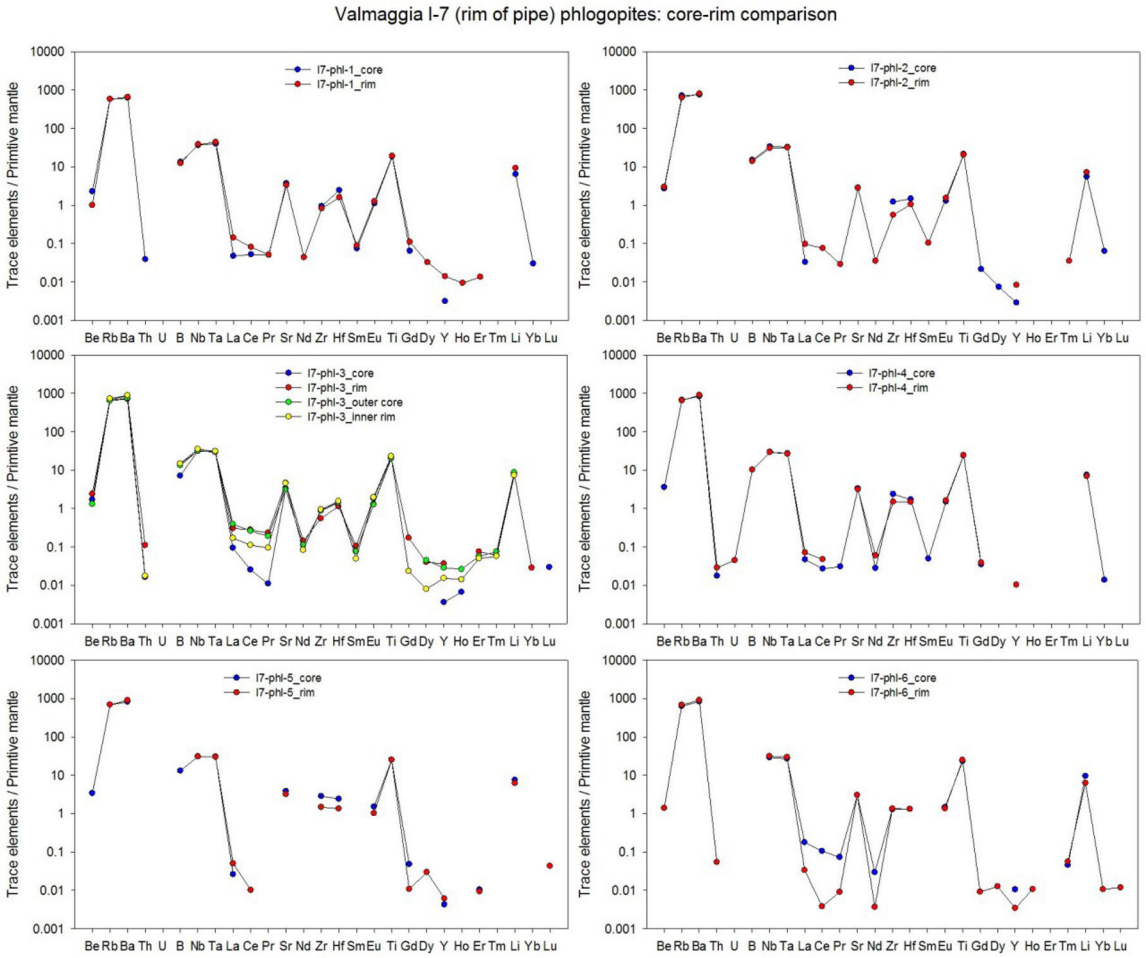

References

References

McDonough WF; Sun SS (1995): The composition of the Earth. Chemical Geology, v. 120, no. 3, pp. 223–253.

Appendix 4 -: Pipe bulk rock compositions generated during this study

Locality Sample ID		Bec d'Ovaga BO1241	Bec d'Ovaga BO1242	Bec d'Ovaga BO1243	Bec d'Ovaga BO1244	Bec d'Ovaga BO1245	Bec d'Ovaga BO1246
SiO2	*wt%*	45.38	45.68	45.78	42.95	53.27	43.35
TiO2	*wt%*	1.02	0.78	0.9	0.94	0.95	3.53
AI2O3	*wt%*	8.95	10.97	8.29	9.8	22.9	17.47
Fetot	*wt%*	13.35	13.78	13.22	13.4	5.72	10.15
MnO	*wt%*	0.17	0.17	0.18	0.16	0.06	0.13
MgO	*wt%*	23.34	18.04	21.27	23.48	1.25	7.72
CaO	*wt%*	5.57	6.62	7.08	5.89	6.38	8.42

Locality Sample ID		Bec d'Ovaga BO1241	Bec d'Ovaga BO1242	Bec d'Ovaga BO1243	Bec d'Ovaga BO1244	Bec d'Ovaga BO1245	Bec d'Ovaga BO1246
Na2O	*wt%*	1.46	1.74	1.23	1.07	4.78	2.52
K2O	*wt%*	0.45	0.38	0.35	0.57	2.85	3.59
P2O5	*wt%*	0.26	0.23	0.2	0.27	0.41	2.23
Ba	*ppm*	174	180	176	236	>1740	>1740
Be	*ppm*	0.71	0.92	0.79	0.78	0.54	0.83
Bi	*ppm*	0.24	0.59	0.16	0.17	0.3	<0.15
Cd	*ppm*	0.27	0.43	0.27	0.18	0.25	0.19
Ce	*ppm*	17.0	13.9	15.3	19.2	25.1	107
Co	*ppm*	87.4	115	84.1	94.2	55.5	36.7
Cr	*ppm*	1487	938	1342	920	15.0	28.0
Cs	*ppm*	0.56	0.36	0.28	0.88	0.14	1.71
Cu	*ppm*	432	1076	397	252	>2900	180
Dy	*ppm*	3.09	2.25	2.83	2.78	1.24	8.46
Er	*ppm*	1.80	1.36	1.68	1.61	0.65	4.05
Eu	*ppm*	1.08	0.93	0.99	1.06	6.13	4.65
Ga	*ppm*	10.2	11.9	10.3	10.1	21.2	21.9
Gd	*ppm*	3.15	2.28	2.88	2.87	1.75	12.2
Hf	*ppm*	1.90	1.45	1.79	2.28	3.57	1.14
Ho	*ppm*	0.62	0.45	0.58	0.55	0.23	1.56
In	*ppm*	0.07	0.08	0.08	0.05	0.05	0.06
La	*ppm*	7.00	5.92	6.12	8.18	14.8	44.6
Li	*ppm*	2.90	2.90	3.30	6.00	8.80	7.00
Lu	*ppm*	0.25	0.19	0.24	0.21	0.08	0.37
Mo	*ppm*	0.52	0.60	0.43	0.47	0.29	0.15
Nb	*ppm*	4.27	3.12	3.41	4.66	2.18	10.9
Nd	*ppm*	11.8	9.12	10.5	12.5	12.9	69.5
Ni	*ppm*	1133	2140	848	1048	1178	350
Pb	*ppm*	3.60	5.00	2.40	4.30	10.0	4.70
Pr	*ppm*	2.52	2.02	2.22	2.77	3.08	15.3
Rb	*ppm*	7.50	6.50	5.33	10.6	18.9	80.9
Sb	*ppm*	0.05	0.06	0.06	0.07	0.04	<0.04
Sc	*ppm*	24.7	25.5	32.4	19.1	4.90	22.9
Sm	*ppm*	2.93	2.14	2.65	2.89	2.14	14.2
Sn	*ppm*	1.45	0.97	1.20	1.20	0.38	1.46
Sr	*ppm*	185	198	194	219	549	454
Ta	*ppm*	0.27	0.19	0.21	0.30	0.09	0.50
Tb	*ppm*	0.50	0.35	0.44	0.45	0.22	1.50
Th	*ppm*	0.58	0.61	0.48	0.89	0.104	1.43
Ti	*ppm*	5190	4170	4873	5137	4602	19105
Tl	*ppm*	0.08	0.05	0.04	0.10	0.12	0.36
Tm	*ppm*	0.26	0.20	0.24	0.22	0.08	0.49

Locality Sample ID		Bec d'Ovaga BO1241	Bec d'Ovaga BO1242	Bec d'Ovaga BO1243	Bec d'Ovaga BO1244	Bec d'Ovaga BO1245	Bec d'Ovaga BO1246
U	*ppm*	0.20	0.20	0.17	0.37	0.08	0.59
V	*ppm*	173	174	213	126	82.1	330
W	*ppm*	0.30	0.22	0.24	0.44	0.06	0.17

References

Adam J, and Green T, 2006, Trace element partitioning between mica- and amphibole-bearing garnet lherzolite and hydrous basanitic melt: 1. Experimental results and the investigation of controls on partitioning behaviour: Contributions to Mineralogy and Petrology, v. 152, p. 1–17.

Adam J, Oberti R, Cámara F, and Green TH, 2007, An electron microprobe, LAM-ICP-MS and single-crystal X-ray structure refinement study of the effects of pressure, melt-H2O concentration and O2 on experimentally produced basaltic amphiboles: European Journal of Mineralogy, v. 19, p. 641–655.

Barboza SA, Bergantz GW, and Brown M, 1999, Regional granulite facies metamorphism in the Ivrea zone: is the mafic complex the smoking gun or a red herring?: Geology, v. 27, p. 447–450.

Bea F, and Montero P, 1999, Behavior of accessory phases and redistribution of Zr, REE, Y, Th, and U during metamorphism and partial melting of metapelites in the lower crust: an example from the Kinzigite Formation of Ivrea-Verbano, NW Italy: Geochimica et Cosmochimica Acta, v. 63, p. 1133–1153.

Begg GC, Hronsky JAM, Arndt NT, Griffin WL, O'Reilly SY, and Hayward N, 2010, Lithospheric, Cratonic, and Geodynamic Setting of Ni-Cu-PGE Sulfide Deposits: Economic Geology, v. 105, p. 1057–1070.

Blundy JD, and Wood BJ, 1991, Crystal-chemical controls on the partitioning of Sr and Ba between plagioclase feldspar, silicate melts, and hydrothermal solutions: Geochimica et Cosmochimica Acta, v. 55, p. 193–209.

Boriani A, Origoni EG, Borghi A, and Caironi V, 1990, The evolution of the "Serie dei Laghi" (Strona-Ceneri and Scisti dei Laghi): the upper component of the Ivrea-Verbano crustal section; Southern Alps, North Italy and Ticino, Switzerland: Tectonophysics, v. 182, p. 103–118.

Brenan JM, Ryerson FJ, and Shaw HF, 1998, The role of aqueous fluids in the slab-to-mantle transfer of boron, beryllium, and lithium during subduction: experiments and models: Geochimica et Cosmochimica Acta, v. 62, p. 3337–3347.

Burg J-P, and Vanderhaeghe O, 1993, Structures and way-up criteria in migmatites, with application to the Velay dome (French Massif Central): Journal of Structural Geology, v. 15, p. 1293–1301.

Canil D, and Fedortchouk Y, 2001, Olivine–liquid partitioning of vanadium and other trace elements, with applications to modern and ancient picrites: The Canadian Mineralogist, v. 39, p. 319–330.

Cocherie A, Rossi P, Fanning CM, and Guerrot C, 2005, Comparative use of TIMS and SHRIMP for U–Pb zircon dating of A-type granites and mafic tholeiitic layered complexes and dykes from the Corsican Batholith (France): Lithos, v. 82, p. 185–219.

Coogan LA, Wilson RN, Gillis KM, and MacLeod CJ, 2001, Near-solidus evolution of oceanic gabbros: insights from amphibole geochemistry: Geochimica et Cosmochimica Acta, v. 65, p. 4339–4357.

Costa F, Dungan MA, and Singer BS, 2001, Magmatic Na-rich phlogopite in a suite of gabbroic crustal xenoliths from Volcán San Pedro, Chilean Andes: Evidence for a solvus relation between phlogopite and aspidolite: American Mineralogist, v. 81, p. 29–35.

Dare SAS, Barnes S-J, and Prichard HM, 2010, The distribution of platinum group elements (PGE) and other chalcophile elements among sulfides from the Creighton Ni–Cu–PGE sulfide deposit, Sudbury, Canada, and the origin of palladium in pentlandite: Mineralium Deposita, v. 45, p. 765–793.

Eichhorn R, Loth G, Höll R, Finger F, Schermaier A, and Kennedy A, 2000, Multistage Variscan magmatism in the central Tauern Window (Austria) unveiled by U/Pb SHRIMP zircon data: Contributions to Mineralogy and Petrology, v. 139, p. 418–435.

Exley RA, Sills JD, and Smith JV, 1982, Geochemistry of micas from the finero spinel-lherzolite, Italian Alps: Contributions to Mineralogy and Petrology, v. 82, p. 59–63.

Faccenna C, Becker TW, Lallemand S, Lagabrielle Y, Funiciello F, and Piromallo C, 2010, Subduction-triggered magmatic pulses: A new class of plumes?: Earth and Planetary Science Letters, v. 299, p. 54–68.

Faure M, Lardeaux J-M, and Ledru P, 2009, A review of the pre-Permian geology of the Variscan French Massif Central: Comptes Rendus Geoscience, v. 341, p. 202–213.

Ferrario A, Garuti G, and Sighinolfi GP, 1982, Platinum and palladium in the Ivrea-Verbano basic complex, Western Alps, Italy: Economic Geology, v. 77, p. 1548–1555.

Fiorentini ML, and Beresford SW, 2008, Role of volatiles and metasomatized subcontinental lithospheric mantle in the genesis of magmatic Ni–Cu–PGE mineralization: insights from in situ H, Li, B analyses of hydromagmatic phases from the Valmaggia ultramafic pipe, Ivrea-Verbano Zone (NW Italy): Terra Nova, v. 20, p. 333–340.

Fiorentini ML, Grieco G, Ferrario A, and Tunesi A, 2002, Petrological and metallogenic outlines of the Valmaggia ultramafic pipe (Ivrea zone), NW Alps, Italy: Periodico di Mineralogia, v. 71, p. 219–239.

Foley S, 1992, Potassic and ultrapotassic magmas and their originVein-plus-wall-rock melting mechanisms in the lithosphere and the origin of potassic alkaline magmas: Lithos, v. 28, p. 435–453.

Foley SF, Prelevic D, Rehfeldt T, and Jacob DE, 2013, Minor and trace elements in olivines as probes into early igneous and mantle melting processes: Earth and Planetary Science Letters, v. 363, p. 181–191.

Foley SF, Venturelli G, Green DH, and Toscani L, 1987, The ultrapotassic rocks: characteristics, classification, and constraints for petrogenetic models: Earth-Science Reviews, v. 24, p. 81–134.

Fritschle T, Prelević D, Foley SF, and Jacob DE, 2013, Petrological characterization of the mantle source of Mediterranean lamproites: Indications from major and trace elements of phlogopite: Chemical Geology, v. 353, p. 267–279.

Garuti G, Bea F, Zaccarini F, and Montero P, 2001, Age, Geochemistry and Petrogenesis of the Ultramafic Pipes in the Ivrea Zone, NW Italy: Journal of Petrology, v. 42, p. 433–319.

Garuti G, Fiandri P, and Rossi A, 1986, Sulfide composition and phase relations in the Fe-Ni-Cu ore deposits of the Ivrea-Verbano basic complex (western Alps, Italy): Mineralium Deposita, p. 22–34.

Garuti G, Rivalenti G, Rossi A, Siena F, and Sinigoi S, 1980 The Ivrea-Verbano mafic ultramafic complex of the Italian western Alps: Discussion of some petrologic problems and a summary: Rendiconti della Societa Italiana di Mineralogia e Petrografia, v. 36.

Gillis KM, Coogan LA, and Chaussidon M, 2003, Volatile element (B, Cl, F) behaviour in the roof of an axial magma chamber from the East Pacific Rise: Earth and Planetary Science Letters, v. 213, p. 447–462.

Godel B, Barnes S-J, and Maier WD, 2007, Platinum-Group Elements in Sulphide Minerals, Platinum-Group Minerals, and Whole-Rocks of the Merensky Reef (Bushveld Complex, South Africa): Implications for the Formation of the Reef: Journal of Petrology, v. 48, p. 1569–1604.

Godel B, Barnes SJ, and Barnes S-J, 2013, Deposition mechanisms of magmatic sulphide liquids: evidence from high-resolution X-ray computed tomography and trace element chemistry of komatiite-hosted disseminated sulphides: Journal of Petrology, v. 54.

Grieco G, Ferrario A, von Quadt A, Koeppel V, and Mathez EA, 2001, The Zircon-Bearing Chromitites of the Phlogopite Peridotite of Finero (Ivrea Zone, Southern Alps): Evidence and Geochronology of a Metasomatized Mantle Slab: Journal of Petrology, v. 42, p. 89–24.

Hartmann G, and Wedepohl HK, 1993, The composition of peridotite tectonites from the Ivrea Complex, northern Italy: Residues from melt extraction: Geochimica et Cosmochimica Acta, v. 57, p. 1761–1782.

Henk A, Franz L, Teufel S, and Oncken O, 1997, Magmatic underplating, extension, and crustal reequilibration: insights from a cross-section through the Ivrea Zone and Strona-Ceneri Zone, Northern Italy: The Journal of Geology, v. 105, p. 367–377.

Hughes HSR, McDonald I, and Kerr AC, 2015, Platinum-group element signatures in the North Atlantic Igneous Province: Implications for mantle controls on metal budgets during continental breakup: Lithos, v. 233, p. 89–110.

Johnson MC, Rutherford MJ, and Hess PC, 1991, Chassigny petrogenesis: Melt compositions, intensive parameters and water contents of Martian (?) magma: Geochimica et Cosmochimica Acta, v. 55, p. 349–366.

Kelley KA, and Cottrell E, 2009, Water and the Oxidation State of Subduction Zone Magmas: Science, v. 325, p. 605–607. [PubMed: 19644118]

Kiseeva ES, and Wood BJ, 2013, A simple model for chalcophile element partitioning between sulphide and silicate liquids with geochemical applications: Earth and Planetary Science Letters, v. 383, p. 68–81.

Kullerud G, Yund RA, and Moh GH, 1969, Phase relations in the Cu–Fe–S, Cu–Ni–S and Fe–Ni–S system: In: Wilson HDB (ed.) Magmatic Ore Deposits. Economic Geology Monograph, v. 4.

Le Vaillant M, Saleem A, Barnes SJ, Fiorentini ML, Miller J, Beresford S, and Perring C, 2015, Hydrothermal remobilisation around a deformed and remobilised komatiite-hosted Ni-Cu-(PGE) deposit, Sarah's Find, Agnew Wiluna greenstone belt, Yilgarn Craton, Western Australia: Mineralium Deposita, p. 1–20.

Leake BE, Woolley AR, Arps CES, Birch WD, Gilbert MC, Grice JD, Hawthorne FC, Kato A, Kisch HJ, Krivovichev VG, Lintout K, Laird J, Mandarino JA, Maresch JC, Nickel EH, Rock NMS, Schumacher JC, Smith DC, Stephenson NCN, Ungaretti L, Whittaker EJW, and Youzhi G, 1997, Nomenclature of amphiboles: Report on the Subcommittee on Amphiboles of the International Mineralogical Association, Commission on New Minerals and Mineral Names: American Mineralogist, v. 82, p. 1019–1037.

Ledru P, Autran A, and Santallier D, 1994, Lithostratigraphy of Variscan Terranes in the French Massif Central: A Basis for Paleogeographical Reconstruction, *in* Chantraine J, Rolet J, Santallier DS, Piqué A, and Keppie JD, eds., Pre-Mesozoic Geology in France and Related Areas. IGCP-Project 233, Springer Berlin Heidelberg, p. 276–288.

Ledru P, Courrioux G, Dallain C, Lardeaux JM, Montel JM, Vanderhaeghe O, and Vitel G, 2001, The Velay dome (French Massif Central): melt generation and granite emplacement during orogenic evolution: Tectonophysics, v. 342, p. 207–237.

Lee C-TA, Leeman WP, Canil D, and Li Z-XA, 2005, Similar V/Sc systematics in MORB and arc basalts: implications for the oxygen fugacities of their mantle source regions: Journal of Petrology, v. 46, p. 2313–2336.

Locmelis M, Barnes SJ, Pearson NJ, and Fiorentini ML, 2009, Anomalous Sulfur-Poor Platinum Group Element Mineralization in Komatiitic Cumulates, Mount Clifford, Western Australia: Economic Geology, v. 104, p. 841–855.

Locmelis M, Melcher F, and Oberthür T, 2010, Platinum-group element distribution in the oxidized Main Sulfide Zone, Great Dyke, Zimbabwe: Mineralium Deposita, v. 45, p. 93–109.

Loucks RR, 2014, Distinctive composition of copper-ore-forming arcmagmas: Australian Journal of Earth Sciences, v. 61, p. 5–16.

Lu Y, Loucks RR, Fiorentini ML, Yang Z, and Hou Z, 2015, Fluid flux melting generated postcollisional high Sr/Y copper ore–forming water-rich magmas in Tibet: Geology.

Ludwig KR, 2011, Isoplot/Ex, Version 4.15: A geochronological toolkit for Microsoft Excel: Geochronology Center Berkeley, v. 4, p. 1–70.

Mallmann G, and O'Neill HSC, 2007, The effect of oxygen fugacity on the partitioning of Re between crystals and silicate melt during mantle melting: Geochimica et Cosmochimica Acta, v. 71, p. 2837–2857.

Matte P, 2001, The Variscan collage and orogeny (480–290 Ma) and the tectonic definition of the Armorica microplate: a review: Terra Nova, v. 13, p. 122–128.

Mattinson JM, 2005, Zircon U–Pb chemical abrasion ("CA-TIMS") method: Combined annealing and multi-step partial dissolution analysis for improved precision and accuracy of zircon ages: Chemical Geology, v. 220, p. 47–66.

Mavrogenes JA, and O'Neill HSC, 1999, The relative effects of pressure, temperature and oxygen fugacity on the solubility of sulfide in mafic magmas: Geochimica et Cosmochimica Acta, v. 63, p. 1173–1180.

Mazzucchelli M, Zanetti A, Rivalenti G, Vannucci R, Correia CT, and Tassinari CCG, 2010, Age and geochemistry of mantle peridotites and diorite dykes from the Baldissero body: Insights into the Paleozoic–Mesozoic evolution of the Southern Alps: Lithos, v. 119, p. 485–500.

McDonough WF, and Sun S-S, 1995, The composition of the Earth: Chemical Geology, v. 120, p. 223–253.

Mehnert KR, 1975, The Ivrea Zone, a model of the deep crust: Neues Jahrbuch fuer Mineralogie: Abhandlungen, v. 125, p. 156–199.

Merzbacher C, and Eggler DH, 1984, A magmatic geohygrometer: Application to Mount St. Helens and other dacitic magmas: Geology, v. 12, p. 587–590.

Mitchell RH, and Bergman SC, 1991, Petrology of lamproites: Springer Science & Business Media.

Mole DR, Fiorentini ML, Thebaud N, Cassidy KF, McCuaig TC, Kirkland CL, Romano SS, Doublier MP, Belousova EA, Barnes SJ, and Miller J, 2014, Archean komatiite volcanism controlled by the evolution of early continents Proceedings of National Academy of Sciences, v. 111, p. 10083–10088.

Monjoie P, Bussy F, Schaltegger U, Mulch A, Lapierre H, and Pfeifer HR, 2007, Contrasting magma types and timing of intrusion in the Permian layered mafic complex of Mont Collon (Western Alps, Valais, Switzerland): evidence from U/Pb zircon and 40Ar/39Ar amphibole dating: Swiss Journal of Geosciences, v. 100, p. 125–135.

Naldrett AJ, 2004, Magmatic sulfide deposits: Geology, Geochemistry and Exploration: Heidelberg, Springer, 728 p.

Nixon PH, 1987, Mantle Xenoliths Wiley, Chichester.

Norman MD, Griffin WL, Pearson NJ, Garcia MO, and O'Reilly SY, 1998, Quantitative analysis of trace element abundances in glasses and minerals: a comparison of laser ablation inductively coupled plasma mass spectrometry, solution inductively coupled plasma mass spectrometry, proton microprobe and electron microprobe data: Journal of Analytical Atomic Spectrometry, v. 13, p. 477–482.

Norman MD, Pearson NJ, Sharma A, and Griffin WL, 1996, Quantitative analysis of trace elements in geological materials by laser ablation ICPMS: Instrumental operating conditions and calibration values of NIST glasses: Geostandards Newsletter, v. 20, p. 247–261.

O'Hara MJ, 1968, The bearing of phase equilibria studies in synthetic and natural systems on the origin and evolution of basic and ultrabasic rocks: Earth-Science Reviews, v. 4, p. 69–133.

Oberthür T, 2011, Platinum-group Element Mineralization of the Main sulfide Zone, Great Dyke, Zimbabwe: Reviews in Economic Geology, v. 17.

Paquette J-L, Ménot R-P, Pin C, and Orsini J-B, 2003, Episodic and short-lived granitic pulses in a post-collisional setting: evidence from precise U-Pb zircon dating through a crustal cross-section in Corsica: Chemical Geology, v. 198, p. 1–20.

Peccerillo A, and Martinotti G, 2006, The Western Mediterranean lamproitic magmatism: origin and geodynamic significance: Terra Nova, v. 18, p. 109–117.

Pin C, and Sills JD, 1986, Petrogenesis of layered gabbros and ultramafic rocks from Val Sesia, the Ivrea Zone, NW Italy: trace element and isotope geochemistry Geological Society, London, Special Publications, v. 24, p. 231–249.

Prelevic D, and Foley SF, 2007, Accretion of arc-oceanic lithospheric mantle in the Mediterranean: Evidence from extremely high-Mg olivines and Cr-rich spinel inclusions in lamproites: Earth and Planetary Science Letters, v. 256, p. 120–135.

Prelević D, Foley SF, Romer R, and Conticelli S, 2008, Mediterranean Tertiary lamproites derived from multiple source components in postcollisional geodynamics: Geochimica et Cosmochimica Acta, v. 72, p. 2125–2156.

Quick JE, Sinigoi S, and Mayer A, 1994, Emplacement dynamics of a large mafic intrusion in the lower crust, Ivrea-Verbano Zone, northern Italy: Journal of Geophyiscal Research, v. 99, p. 21559–21573.

Raddick MJ, Parmentier EM, and Scheirer DS, 2002, Buoyant decompression melting: A possible mechanism for intraplate volcanism: Journal of Geophysical Research: Solid Earth, v. 107, p. ECV 7–1–ECV 7–14.

Richards JP, 2013, Giant ore deposits formed by optimal alignments and combinations of geological processes: Nature Geosci, v. 6, p. 911–916.

Rivalenti G, Garuti G, Rossi A, Siena F, and Sinigoi S, 1981, Existence of Different Peridotite Types and of a Layered Igneous Complex in the Ivrea Zone of the Western Alps: Journal of Petrology, v. 22, p. 127–153.

Rivalenti G, Rossi A, Siena F, and Sinigoi S, 1984, The layered series of the Ivrea-Verbano igneous complex, Western Alps, Italy: Tschermaks Mineralogische und Petrographische Mitteilungen, v. 33, p. 77–99

Rowe MC, Kent AJR, and Nielsen RL, 2009, Subduction Influence on Oxygen Fugacity and Trace and Volatile Elements in Basalts Across the Cascade Volcanic Arc: Journal of Petrology, v. 50, p. 61–91.

Rutter EH, Brodie KH, and Evans PJ, 1993, Structural geometry, lower crustal magmatic underplating and lithospheric stretching in the Ivrea-Verbano zone, northern Italy: Journal of Structural Geology, v. 15, p. 647–662.

Schaltegger U, 1997, Magma pulses in the Central Variscan Belt: episodic melt generation and emplacement during lithospheric thinning: Terra Nova, v. 9, p. 242–245.

Schaltegger U, Ulianov A, Müntener O, Ovtcharova M, Peytcheva I, Vonlanthen P, Vennemann T, Antognini M, and Girlanda F, 2015, Megacrystic zircon with planar fractures in miaskite-type nepheline pegmatites formed at high pressures in the lower crust (Ivrea Zone, southern Alps, Switzerland), American Mineralogist, 100, p. 83.

Schmid SM, Zingg A, and Handy M, 1987, The kinematics of movements along the Insubric Line and the emplacement of the Ivrea Zone: Tectonophysics, v. 135, p. 47–66.

Schnetger B, 1994, Partial melting during the evolution of the amphibolite- to granulite-facies gneisses of the Ivrea Zone, northern Italy: Chemical Geology, v. 113, p. 71–101.

Seat Z, Stone WE, Mapleson DB, and Daddow BC, 2004, Tenor variation within komatiite-associated nickel sulphide deposits: insights from the Wannaway Deposit, Widgiemooltha Dome, Western Australia: Mineralogy and Petrology, v. 82.

Shabanian E, Acocella V, Gioncada A, Ghasemi H, and Bellier O, 2012, Structural control on volcanism in intraplate post collisional settings: Late Cenozoic to Quaternary examples of Iran and Eastern Turkey: Tectonics, v. 31, p. n/a–n/a.

Shaw DM, 2006, Trace elements in magmas: a theoretical treatment: Cambridge University Press Cambridge.

Shervais JW, and Mukasa SB, 1991, The Balmuccia orogenic lherzolite massif, Italy: Journal of Petrology, v. Special Lherz iss. 155–174.

Sills JD, and Tarney J, 1984, Petrogenesis and tectonic significance of amphibolites interlayered with metasedimentary gneisses in the Ivrea zone, Southern Alps, Northwest Italy: Tectonophysics, v. 107, p. 187–206.

Sinigoi S, Quick JE, Clemens-Knott D, Mayer A, Demarchi G, Mazzucchelli M, Negrini L, and Rivalenti G, 1994, Chemical evolution of a large mafic intrusion in the lower crust, Ivren-Verbano Zone, northern Italy: Journal Geopgys. Res, v. 99, p. 21575–21590.

Sinigoi S, Quick JE, Demarchi G, and Klötzli U, 2011, The role of crustal fertility in the generation of large silicic magmatic systems triggered by intrusion of mantle magma in the deep crust: Contributions to Mineralogy and Petrology, v. 162, p. 691–707.

Sizova E, Gerya T, and Brown M, 2012, Exhumation mechanisms of melt-bearing ultrahigh pressure crustal rocks during collision of spontaneously moving plates: Journal of Metamorphic Geology, v. 30, p. 927–955.

Stampfli GM, Hochard C, Vérard C, and Wilhelm C, 2013, The formation of Pangea: Tectonophysics, v. 593, p. 1–19.

Taylor SR, and McLennan SM, 1985, The Continental Crust: Its Composition and Evolution: Blackwell Scientific Publications, Oxford, UK, pp. 312.

Tomkins AG, Rebryna KC, Weinberg RF, and Schaefer BF, 2012, Magmatic Sulfide Formation by Reduction of Oxidized Arc Basalt: Journal of Petrology, v. 53, p. 1537–1567.

Tribuzio R, Thirlwall MF, and Messiga B, 1999, Petrology, mineral and isotope geochemistry of the Sondalo gabbroic complex (Central Alps, Northern Italy): implications for the origin of post-Variscan magmatism: Contributions to Mineralogy and Petrology, v. 136, p. 48–62.

Turner SP, Platt JP, George RMM, Kelley SP, Pearson DG, and Nowell GM, 1999, Magmatism Associated with Orogenic Collapse of the Betic–Alboran Domain, SE Spain: Journal of Petrology, v. 40, p. 1011–1036.

Vanderhaeghe O, Teyssier C, and Wysoczanski R, 1999, Structural and geochronological constraints on the role of partial melting during the formation of the Shuswap metamorphic core complex at the latitude of the Thor-Odin dome, British Columbia: Canadian Journal of Earth Sciences, v. 36, p. 917–943.

von Raumer JF, Bussy F, and Stampfli GM, 2009, The Variscan evolution in the External massifs of the Alps and place in their Variscan framework: Comptes Rendus Geoscience, v. 341, p. 239–252.

Wang Z, and Becker H, 2015, Fractionation of highly siderophile and chalcogen elements during magma transport in the mantle: Constraints from pyroxenites of the Balmuccia peridotite massif: Geochimica et Cosmochimica Acta, v. 159, p. 244–263.

Wang Z, Becker H, and Gawronski T, 2013, Partial re-equilibration of highly siderophile elements and the chalcogens in the mantle: A case study on the Baldissero and Balmuccia peridotite massifs (Ivrea Zone, Italian Alps): Geochimica et Cosmochimica Acta, v. 108, p. 21–44.

Wendlandt RF, 1982, Sulfide saturation of basalt and andesite melts at high pressures and temperatures: American Mineralogist, v. 67, p. 877–885.

Wilkinson JJ, 2013, Triggers for the formation of porphyry ore deposits in magmatic arcs: Nature Geosci, v. 6, p. 917–925.

Yoder HS, and Tilley CE, 1962, Origin of basalt magmas: an experimental study of natural and synthetic rock systems: Journal of Petrol., v. 3, p. 342–532

Zaccarini F, Garuti G, Fiorentini ML, Locmelis M, Kollegger P, and Thalhammer OAR, 2014, Mineralogical hosts of platinum group elements (PGE) and rhenium in the magmatic Ni-Fe-Cu sulfide deposits of the Ivrea Verbano Zone (Italy): An electron microprobe study: Neues Jahrbuch f??r Mineralogie - Abhandlungen: Journal of Mineralogy and Geoche, v. 191, p. 169–187.

Zanetti A, Mazzucchelli M, Rivalenti G, and Vannucci R, 1999, The Finero phlogopite-peridotite massif: an example of subduction-related metasomatism: Contributions to Mineralogy and Petrology, v. 134, p. 107–122.

Zingg A, 1983, The Ivrea and Strona-Ceneri Zones (Southern Alps, Ticino and N-Italy): a review: Schweiz. Mineral. Petrogr. Mitt, v. 63, p. 361–392

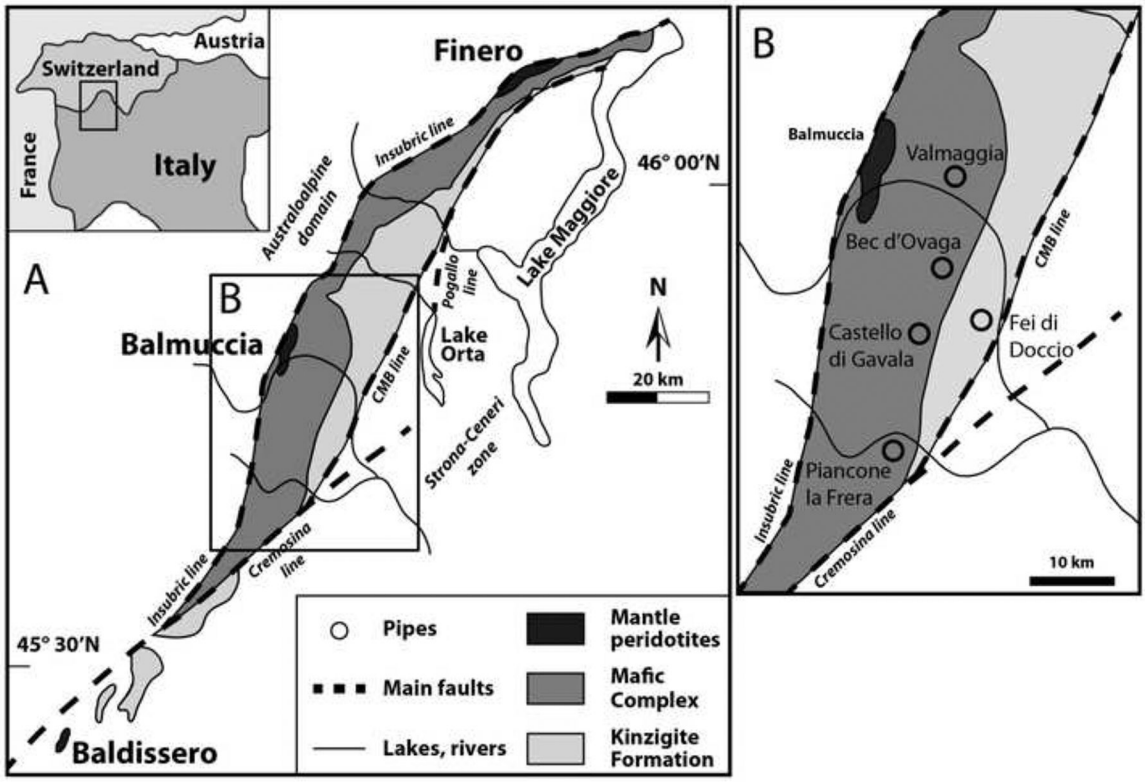

Figure 1 –.

Simplified geological map of the Ivrea-Verbano Zone showing the location of the pipes. Modified from Fiorentini and Beresford (2008).

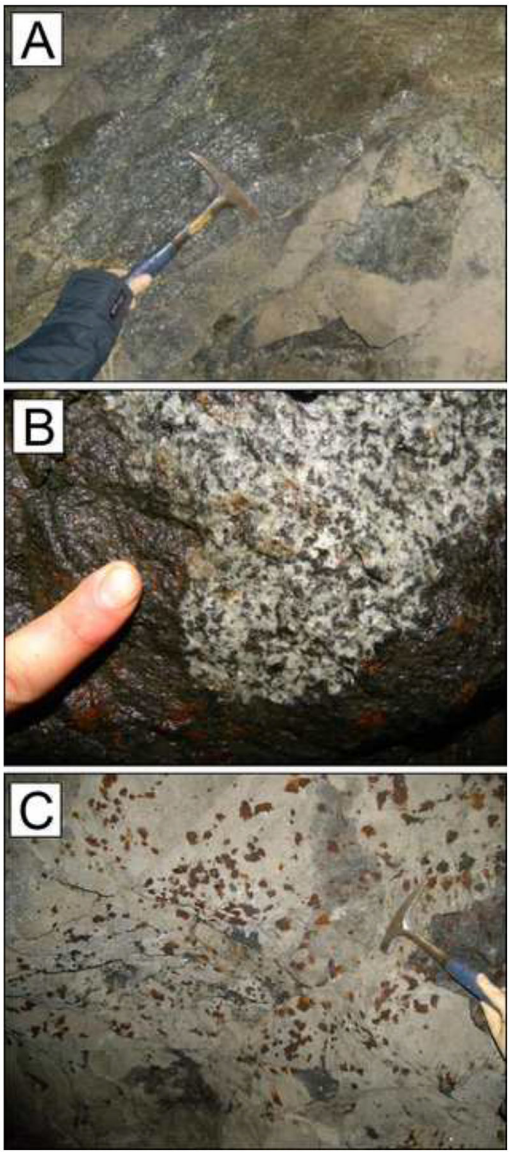

Figure 2 –.

Photographs showing outcrops in the Valmaggia mine. (A) Central part of the Valmaggia pipe, near sample site VMG-7; (B) Sharp contact between the Valmaggia pipe and the host gabbro; (C) Sulfide mineralization in the rim portion of the Valmaggia pipe near sample site I-7. A detailed map of the Valmaggia mine has been provided by Fiorentini et al. (2002).

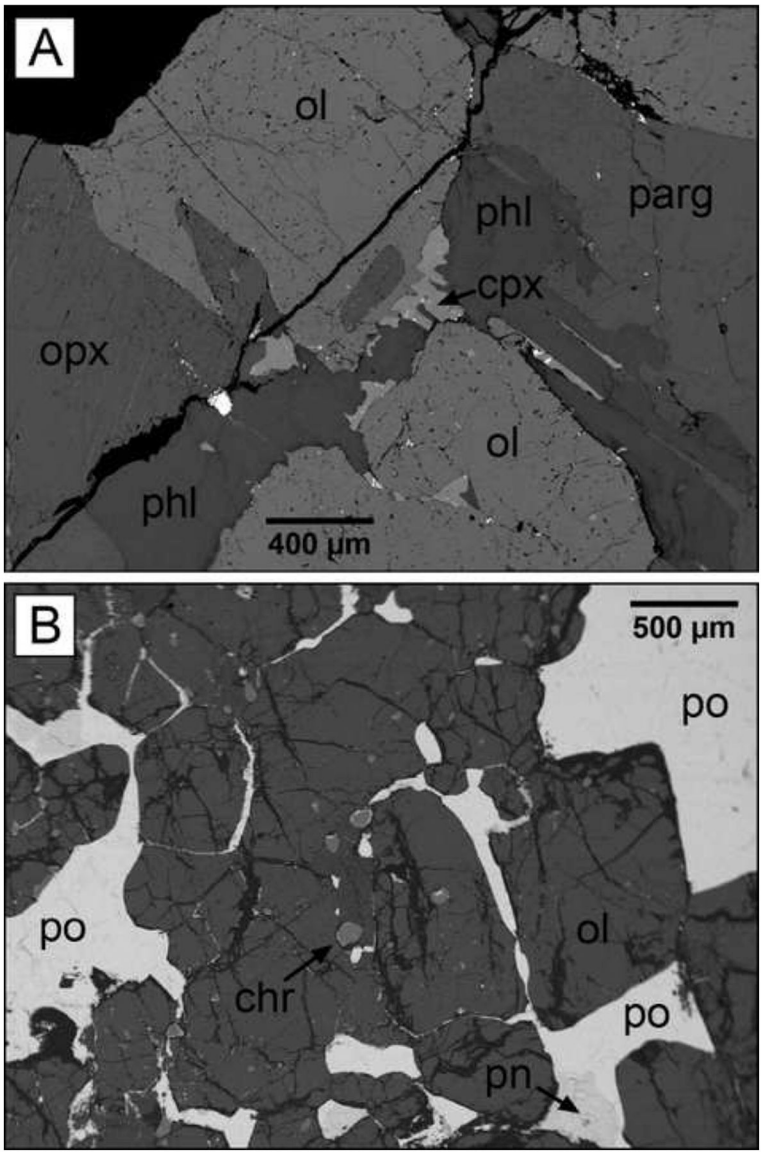

Figure 3 –.

Back scattered electron images of samples from the Valmaggia pipe showing (A) the typical pipe silicate assemblage (sample VMG-7), and (B) semi-massive sulfide mineralization (sample I-7). Chr: chromite, cpx: clinopyroxene, ol: olivine, opx: orthopyroxene, parg: pargasite, phl: phlogopite, pn: pentlandite, po: pyrrhotite.

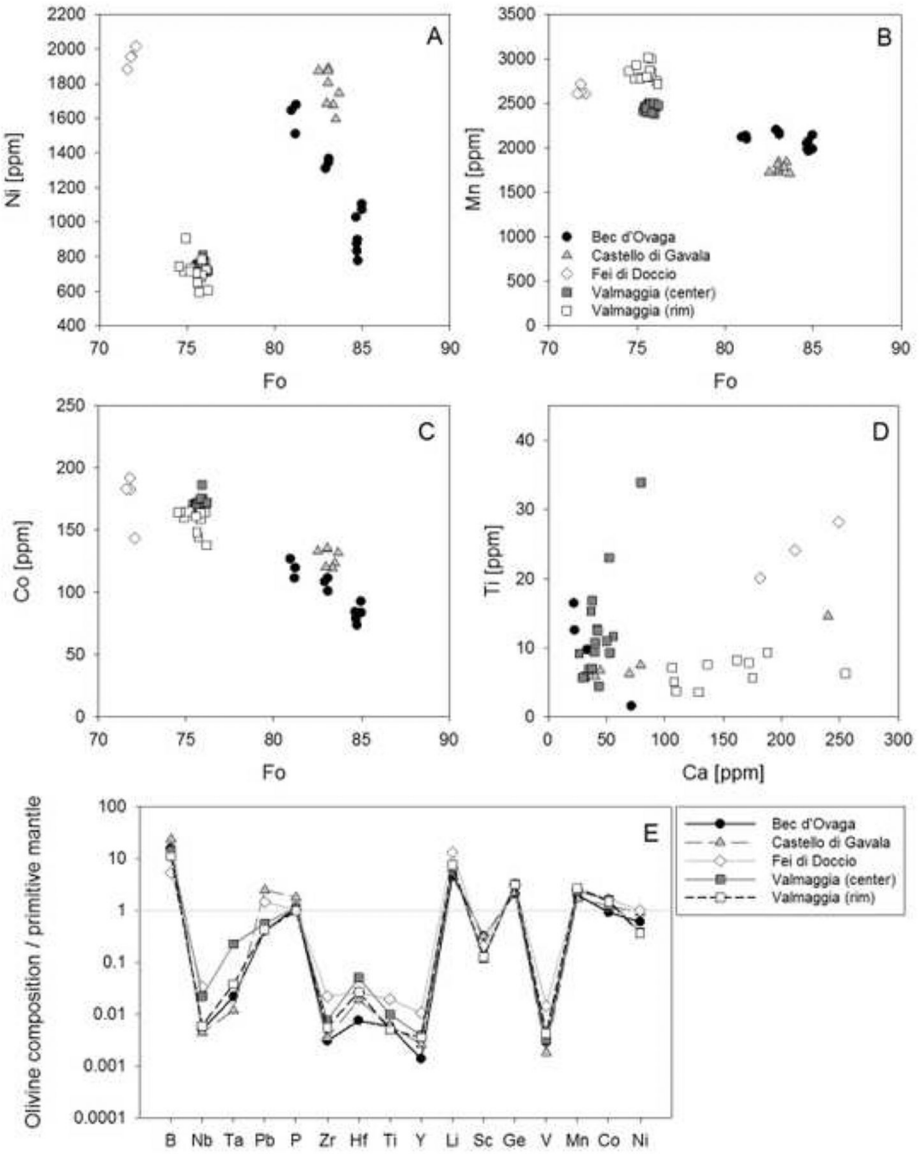

Figure 4 –.

Olivine mineral chemistry for each pipe sample illustrated in binary plots of (A) Ni vs. Fo, (B) Mn vs. Fo, (C) Co vs. Fo, (D) Ti vs. Ca. For the Valmaggia pipe, ‘center’ and ‘rim’ refer to samples collected from the inner and outer portions of the pipe. (E) Primitive mantle normalized trace element spidergram showing the compositional averages for each pipe sample. Primitive mantle values are from McDonough and Sun (1995).

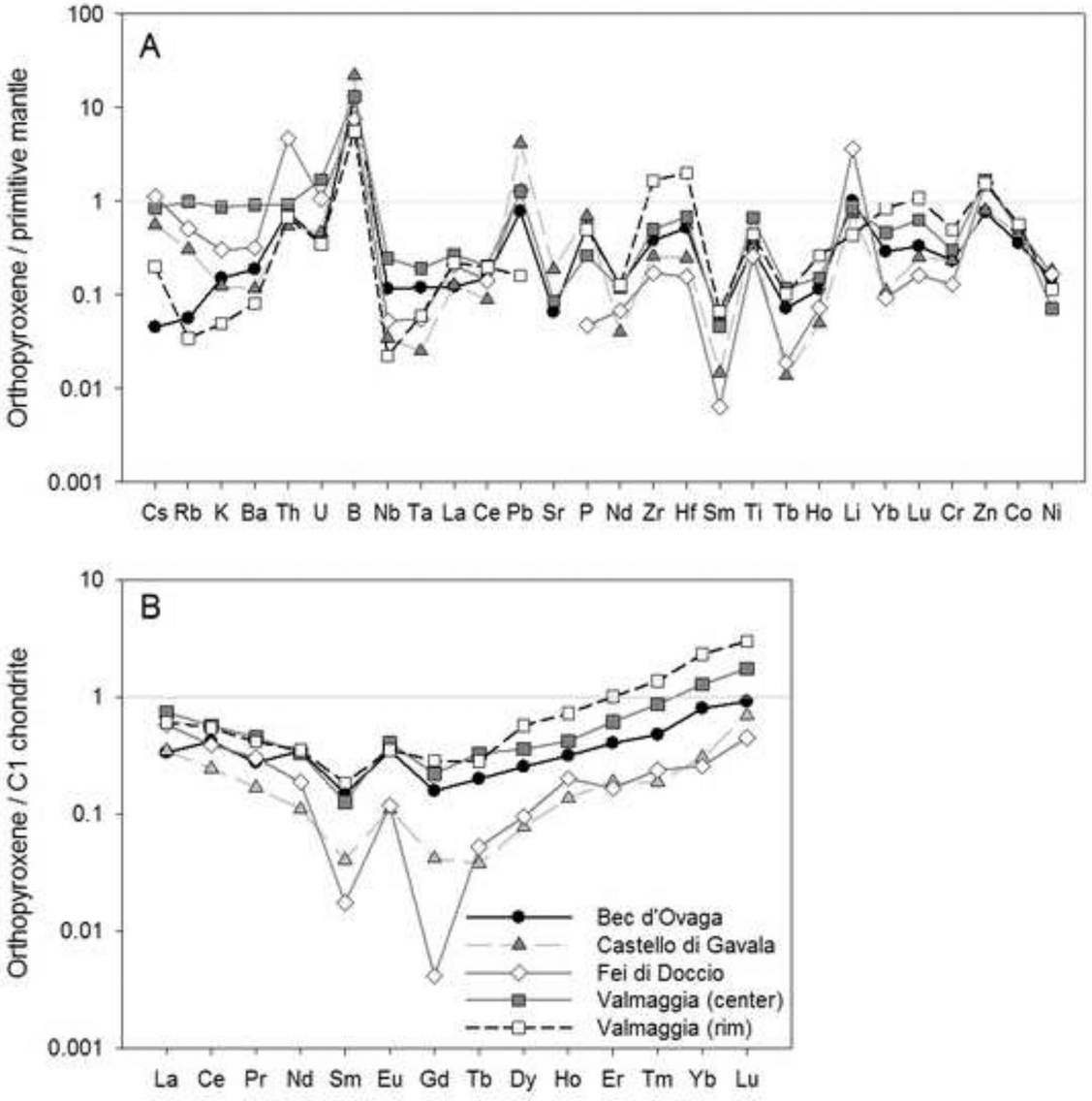

Figure 5 –.

(A) Primitive mantle-normalized concentrations of minor and trace elements, and (B) C1 chondrite-normalized rare earth element concentrations in orthopyroxene from the pipes. Shown are the compositional averages for each pipe sample. For the Valmaggia pipe, 'center' and 'rim' refer to samples collected from the inner and outer portions of the pipe. Primitive mantle values are from McDonough and Sun (1995).

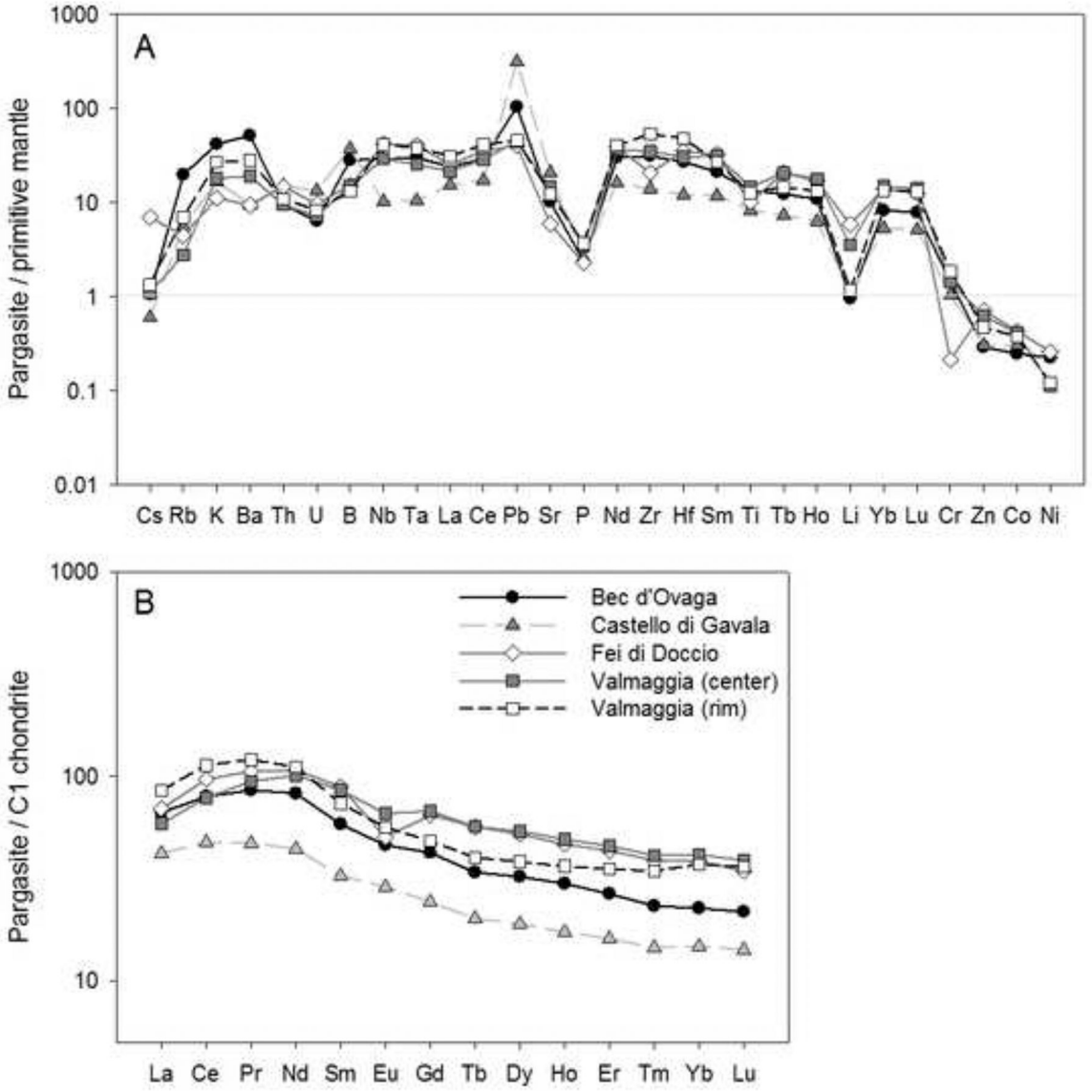

Figure 6 –.

(A) Primitive mantle-normalized concentrations of minor and trace elements, and (B) C1 chondrite-normalized rare earth element concentrations in pargasite from the pipes. Shown are the compositional averages for each pipe sample. For the Valmaggia pipe, ‘center’ and ‘rim’ refer to samples collected from the inner and outer portions of the pipe. Primitive mantle values are from McDonough and Sun (1995).

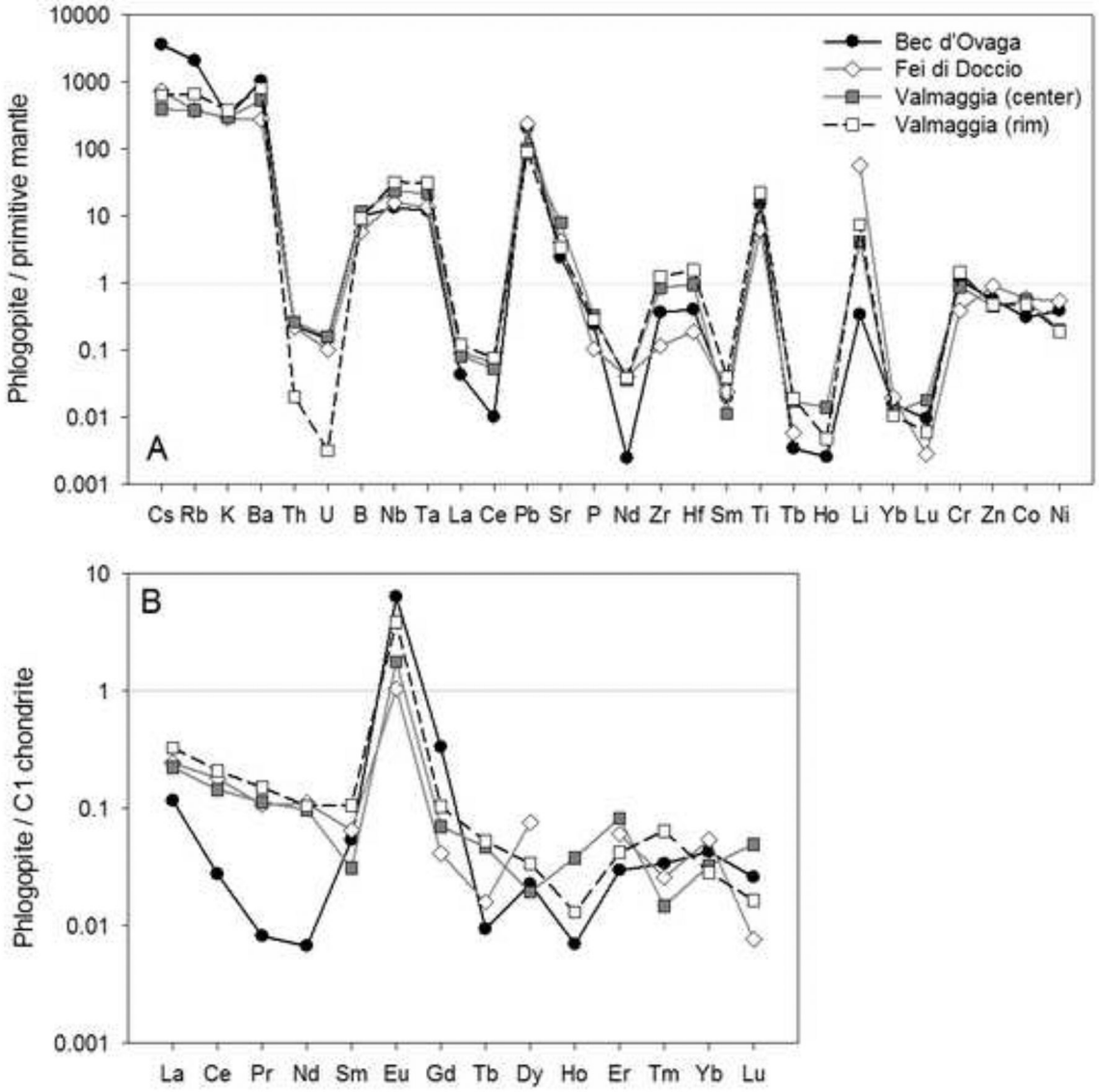

Figure 7 –.

(A) Primitive mantle-normalized trace element concentrations of minor and trace elements, and (B) C1 chondrite-normalized rare earth element concentrations in phlogopite from the pipes. Shown are the compositional averages for each pipe sample. For the Valmaggia pipe, ‘center’ and ‘rim’ refer to samples collected from the inner and outer portions of the pipe. Primitive mantle values are from McDonough and Sun (1995).

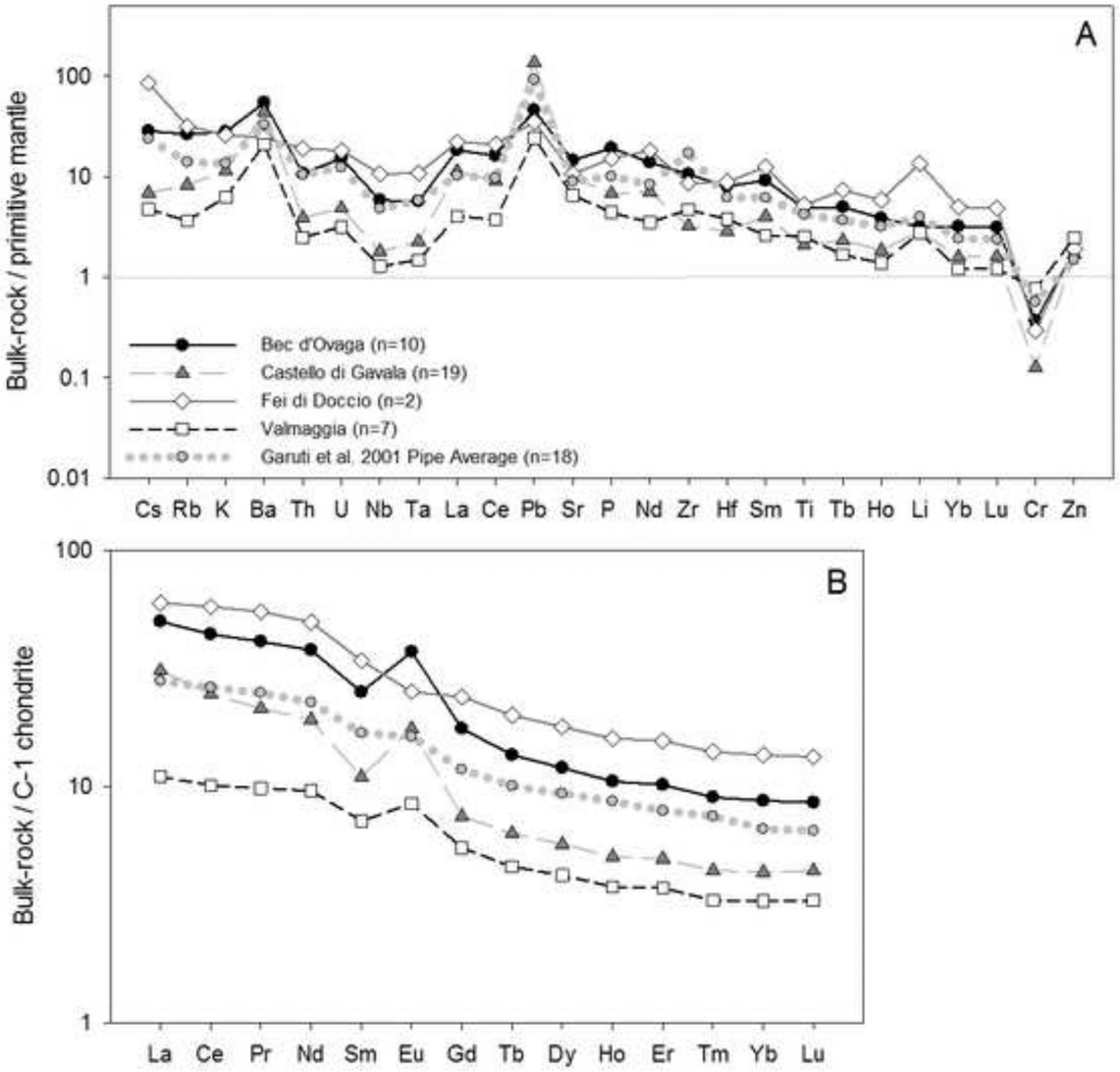

Figure 8 –.

(A) Primitive mantle-normalized concentrations of minor and trace elements, and (B) C1 chondrite-normalized rare earth element concentrations in bulk rock samples from the pipes. The plots show average compositions for each pipe compiled using data from this work and Garuti et al. (2001). Primitive mantle and C1-chondrite values are from McDonough and Sun (1995).

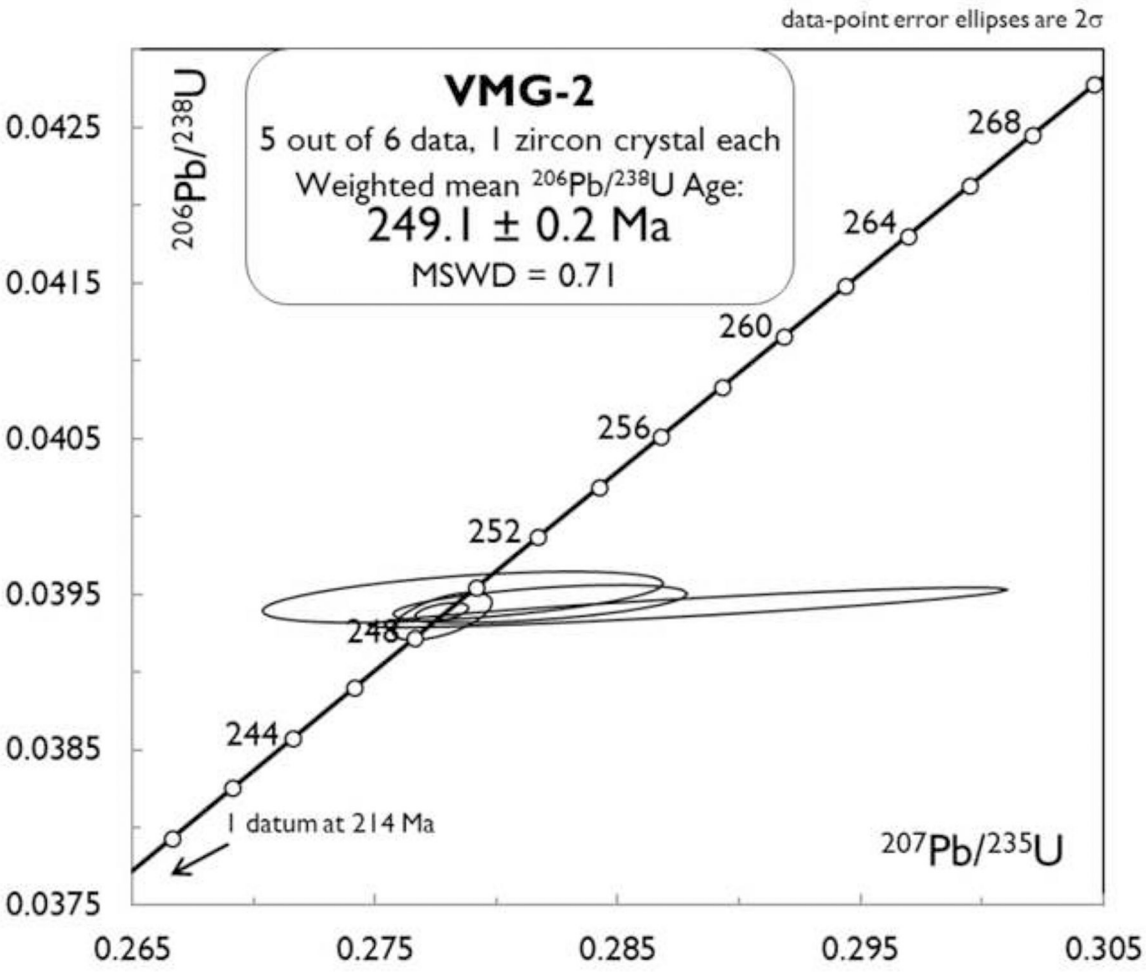

Figure 9 –.

U-Pb Concordia plot of results from chemical abrasion isotope dilution TIMS analyses of zircons from the Valmaggia pipe (sample VMG-2).

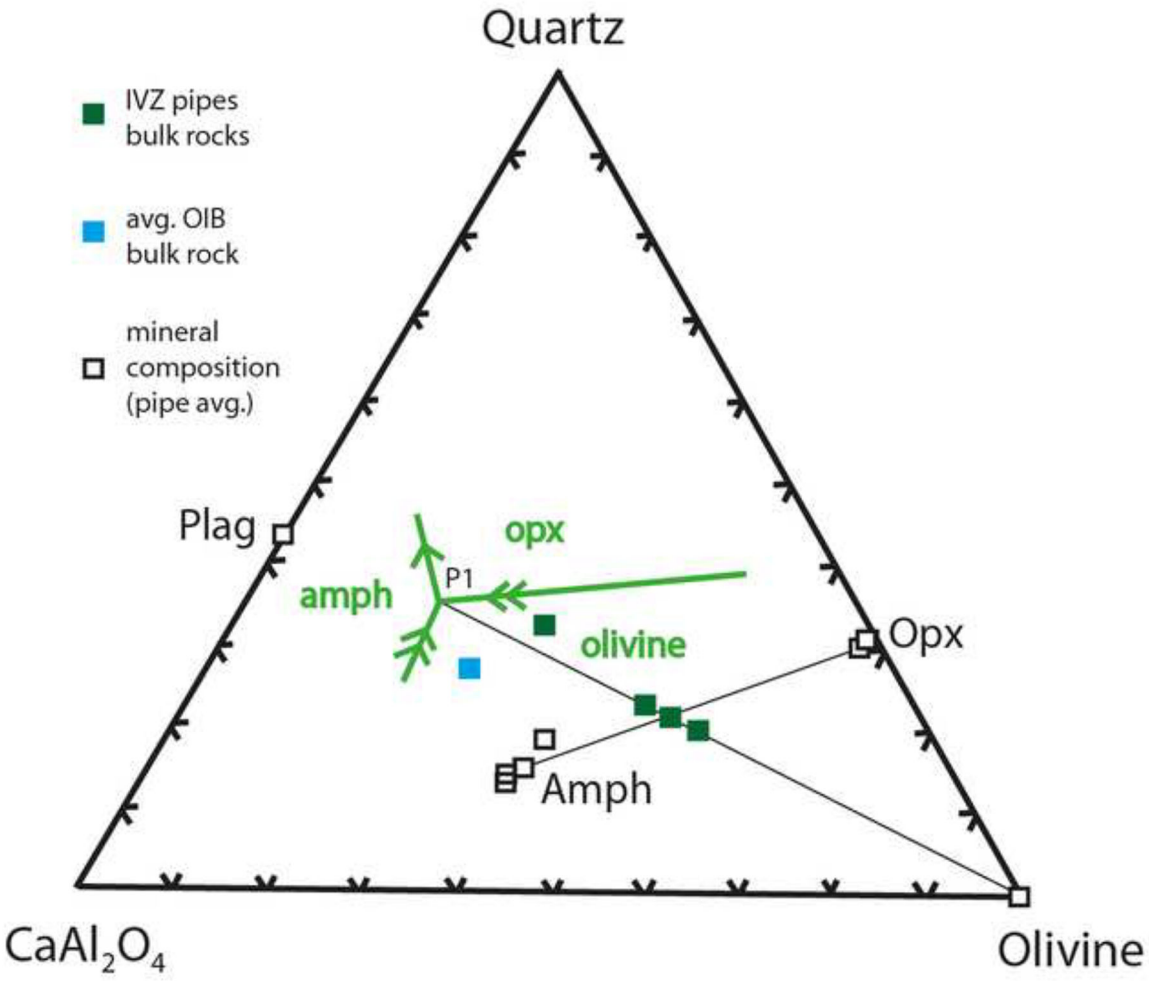

Figure 10 –.

Liquidus equilibria in part of the pseudo-system $CaAl_2O_4$-quartz-diopside-olivine based on experimental data for hydrous olivine basalt (Adam et al., 2007) and basanite melts (Adam and Green, 2006). The projection is from diopside and the relationships are for a diopside-saturated system. Also plotted are bulk-rock compositional data for the individual pipes (green squares), average mineral compositions for the individual pipes (white squares; data for plagioclase from Garuti et al (2001), together with an average ocean-island-basalt (blue square, based on data from the GEOROC data base). It is noted that only amphibole shows notable major element variation, whereas the other pipe mineral averages mostly plot on top of another. P1 = Peritectic 1, amph = amphibole, opx = orthopyroxene, plag = plagioclase. All compositions have been re-cast as CMAS components following the system of O'Hara (1968).

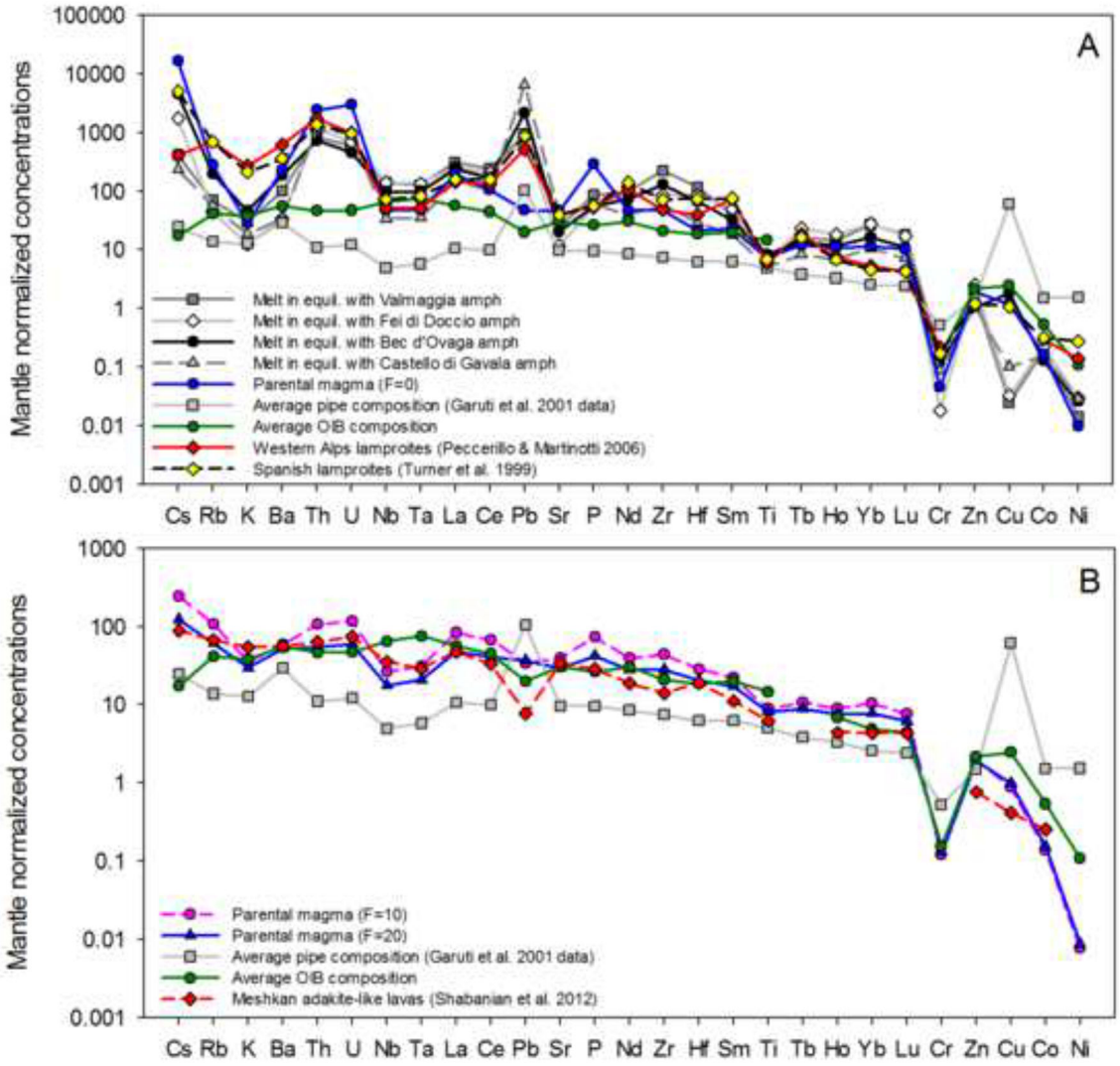

Figure 11 –.

(A) Minor and trace element contents of a parental magma calculated with the assumption that no inter-cumulus melt was retained in the pipes (F=0), and melt compositions in equilibrium with pipe amphiboles. The partition coefficients used in calculations are from Adam et al., (2007) with mineral compositions from Appendix 2 and bulk-rock data from Garuti et al., (2001). The compositions of selected lamproites (Turner et al., 1999; Peccerillo and Martinotti, 2006) and an average ocean-island basalt (GEOROC database) are shown for comparison.

(B) Minor and trace element contents of parental magmas calculated with the assumption that 10% (F=10) or 20% (F=20) inter-cumulus melt was retained in the pipes. The partition coefficients used in calculations are from Adam et al. (2007) [amphibole], Adam and Green (2006) [orthopyroxene and olivine], Kiseeva and Wood (2013) [sulfide melt], and Blundy and Wood (1991) [plagioclase], with bulk-rock data from Garuti et al. (2001). The compositions of arc-like basalts from Meshkan (Shabanian et al., 2012) and an average ocean-island basalt (GEOROC database) are shown for comparison.

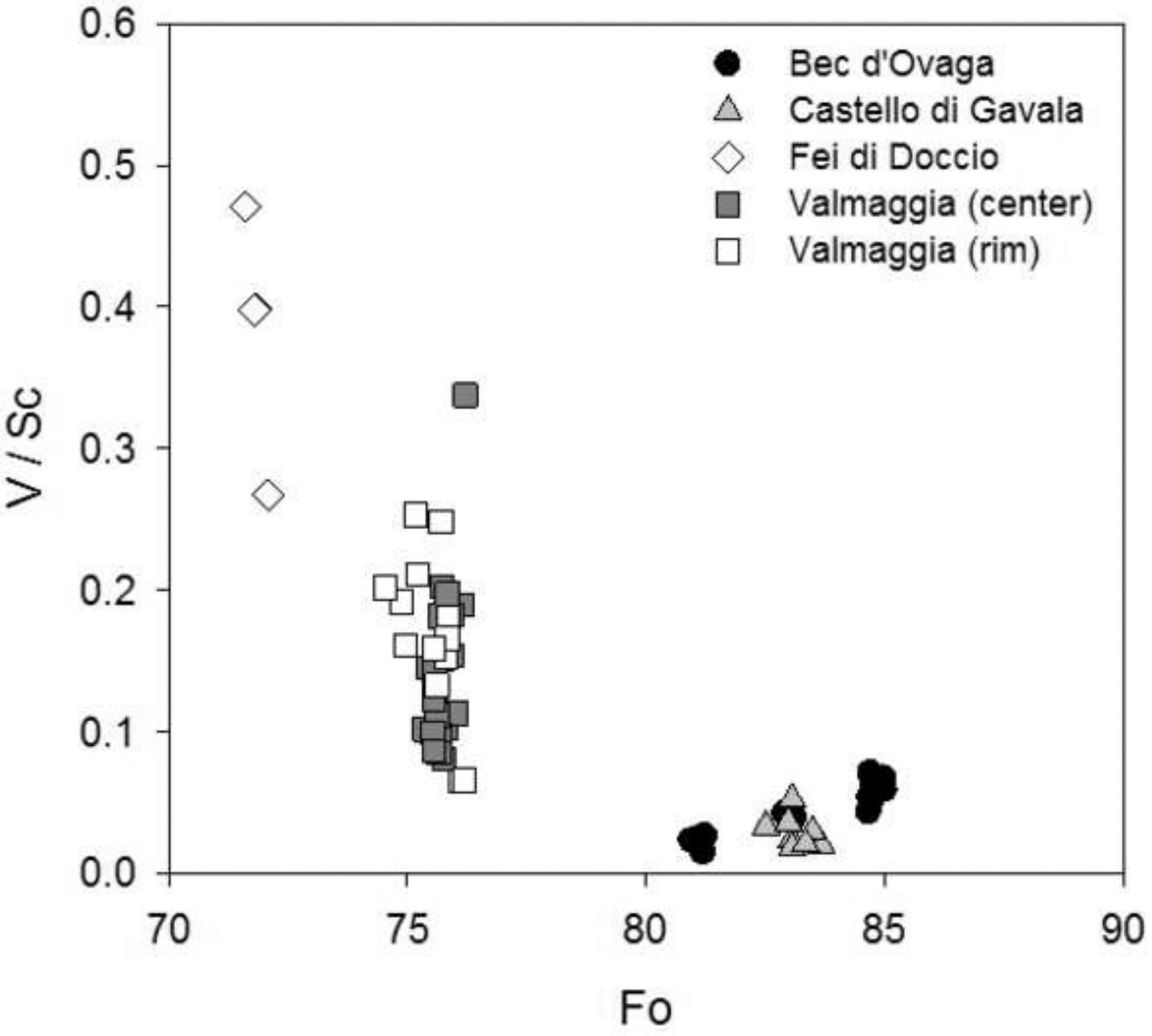

Figure 12–.

Plot of V/Sc vs. Fo in olivines from the pipes. For the Valmaggia pipe average mineral compositions for the individual pipes (data for plagioclase from, ‘center’ and ‘rim’ refer to samples collected from the inner and outer portions of the pipe. Low V/Sc ratios (<1–2) suggest oxidizing conditions during olivine crystallization, whereas reducing conditions would result in higher ratios.

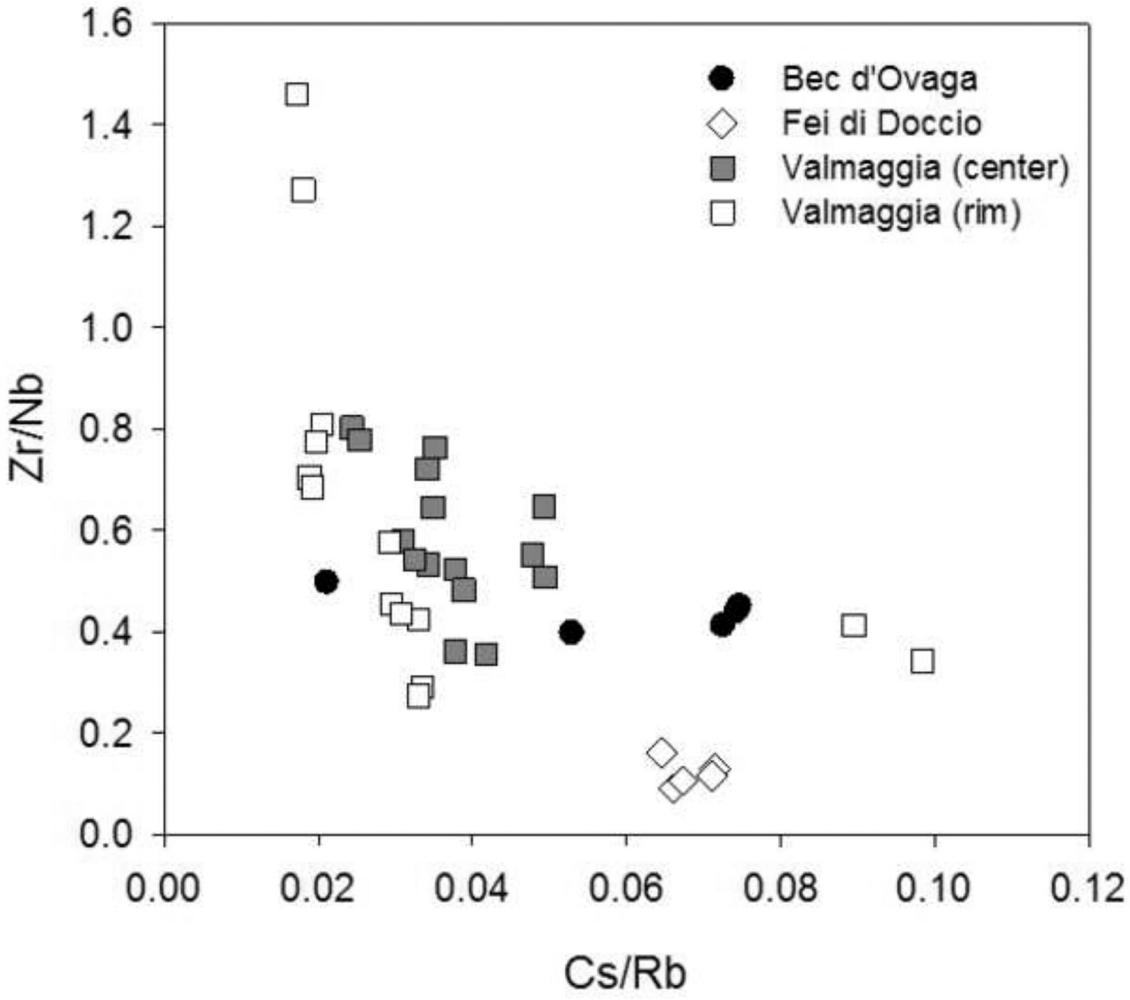

Figure 13 –.

Plots of Cs/Rb vs. Zr/Nb for phlogopite from the pipes. For the Valmaggia pipe, ‘center’ and ‘rim’ refer to samples collected from the inner and outer portions of the pipe.

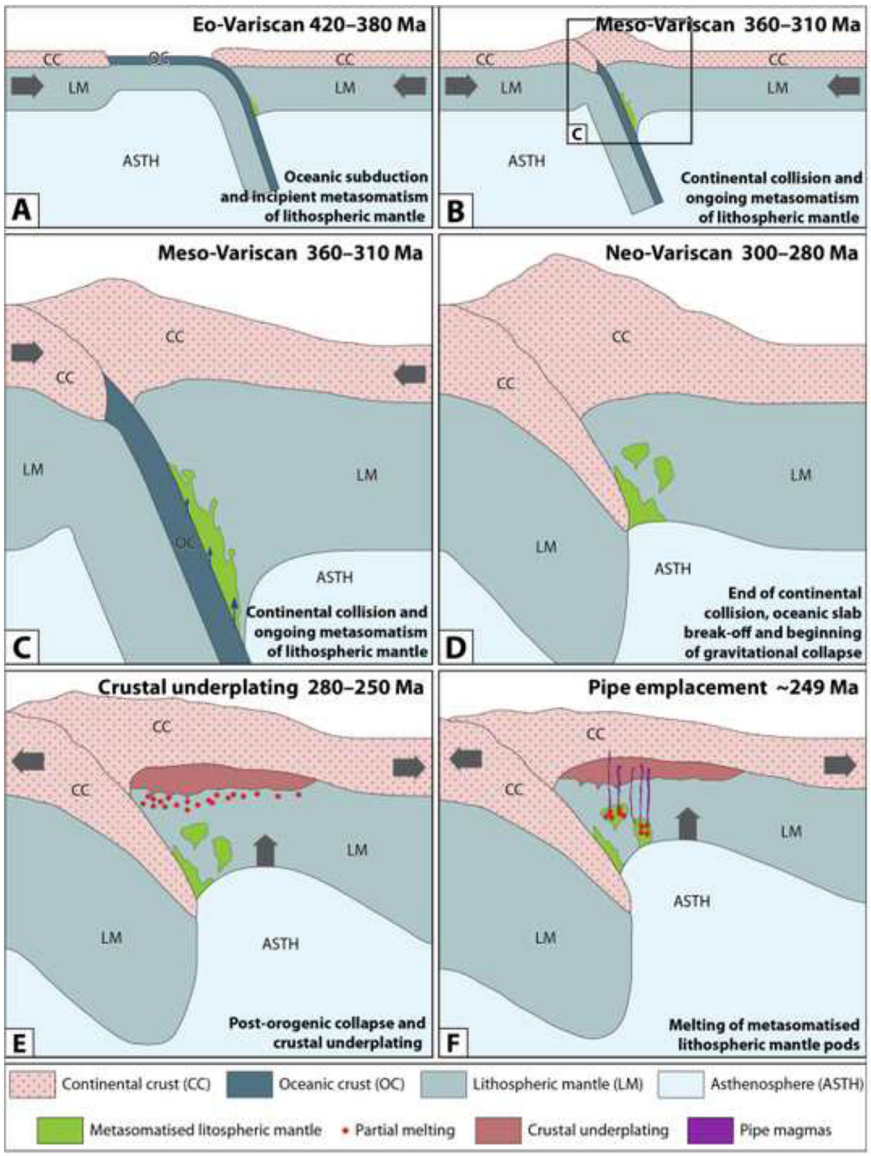

Figure 14 –.

Schematic illustrations of the geodynamic evolution that facilitated the genesis of the pipes. (A) Early oceanic subduction in the Eo-Variscan (420 – 380 Ma) initiating metasomatism of the lithospheric mantle. (B, C) Continental collision and ongoing metasomatism of the lithospheric mantle in the Meso-Variscan (360 – 310 Ma) creates pods of metasomatized mantle (*cf.* D). (D) End of the continental collision and beginning of the gravitational collapse in the Neo-Variscan (300 – 280 Ma). (E) Post orogenic collapse, crustal extension and asthenospheric rise cause decompression melting of the lithospheric mantle and initiate the underplating of the continental crust. (F) Further extension and asthenospheric rise cause partial melting of the metasomatized mantle pods, facilitating the intrusion of the pipe magmas into rocks of the upper lithospheric mantle and lower continental crust.

Table 1 –

Location and key characteristics of the samples analyzed by electron microprobe and laser ablation ICP-MS.

Sample ID	Pipe	Coordinates		Stratigraphic level	Position in pipe	Main phases	Minor and accesssory phases	Sulfide phases	Whole-rock data
BO-1	Bec' Ovaga	45°47'38" N	8°12'58" E	Mafic Complex	Central portion	Parg-Ol-Opx-Phl	Cm-Pl-Cpx-Sp-Ilm-Mag-Ap-Carb	Po-Pn-Cps-Cb-Mck-Py	Garuti et al. 2001
GV-1262	Castello di Gavala	45°46'38.24" N	8°11'24.76" E	Mafic Complex	Central portion	Parg-Opx-Ol	Cm-Phl-Pl-Cpx-Sp-Ilm-Mag-Ap-Carb-Zr	Po-Pn-Cps-Cb-Mck-Py	Garuti et al. 2001
VMG-7	Valmaggia	45°49'51.63" N	8°13'25.07" E	Mafic Complex	Central portion	Parg-Ol-Opx-Phl	Cm-Pl-Cpx-Sp-Ilm-Mag-Ap-Carb-Zr	Po-Pn-Cps-Cb-Mck-Py	This study
I-7	Valmaggia	45°49'51.63" N	8°13'25.07" E	Mafic Complex	Rim portion	Parg-Ol-Opx-Phl	Cm-Pl-Cpx-Sp-Mag-Ap-Carb-Zr	Po-Pn-Cps-Cb-Mck-Py	This study
FD-1	Fei di Doccio	45°45'45.31" N	8°14'43.29" E	Kinzigite Formation	Mine dump	Parg-Ol-Opx-Phl	Cm-Cpx-Pl-Ap-Sp-Ilm-Mag-Zr-Rt-Bd-Gr	Po-Pn-Cps	Garuti et al. 2001

Abbreviations: Parg = pargasite, Ol = olivine, Opx = orthopyroxene, Phl = phlogopite, Cm = cummingtonite, Pl = plagioclase, Cpx = clinopyroxene, Sp = spinel, Ilm = ilmenite, Mag = magnetite, Ap = apatite, Carb =carbonate, Po = pyrrhotite, Pn = pentlandite, Cps = chalcopyrite, Cb = cubanite, Mck = mackinawite, Py = pyrite, Zr = zircon, Rt = rutile, Bd = baddeleyite, Gr = graphite

Table 2 -

ent analyses of minerals from the pipes.

ne			Orthopyroxene							Amphibole					Phlogopite			
ec vaga	Castello di Gavala	Fei di Doccio	Valmaggia (core)[a]	Valmaggia (rim)[a]	Bec d'Ovaga	Castello di Gavala	Fei di Doccio	Valmaggia (core)[a]	Valmaggia (rim)[a]	Bec d'Ovaga	Castello di Gavala	Fei di Doccio	Valmaggia (core)[a]	Valmaggia (rim)[a]	Bec d'Ovaga	Fei di Doccio	Valmaggia (core)[a]	Valmaggia (rim)[a]
01	GV1262A	FD1	VMG7	I7	BO1	GV1262A	FD1	VMG7	I7	BO1	GV1262A	FD1	VMG7	I7	BO1	FD1	VMG7	I7
3	8	4	13	7	6	10	7	7	5	4	14	6	9	6	5	5	10	6
78	40.04	38.78	39.15	38.24	55.49	55.26	55.25	54.67	53.11	42.94	42.11	44.07	42.23	41.17	38.04	38.83	38.08	36.20
01	0.01	0.02	0.01	0.00	0.05	0.07	0.06	0.09	0.08	2.62	1.72	1.75	3.02	2.27	3.40	1.30	3.89	4.39
01	0.01	0.00	0.00	0.00	2.30	3.16	1.64	2.78	3.04	13.26	14.61	13.89	13.96	13.77	16.09	17.34	16.61	15.93
01	0.01	0.00	0.01	0.00	0.12	0.09	0.06	0.13	0.18	0.53	0.45	0.09	0.62	0.69	0.51	0.14	0.37	0.49
66	15.86	21.50	21.98	22.39	10.48	10.83	15.51	13.80	14.11	5.71	7.02	8.52	9.28	8.71	4.83	6.87	7.32	8.16
25	0.23	0.35	0.29	0.35	0.31	0.26	0.35	0.30	0.31	0.12	0.13	0.19	0.15	0.15	0.05	0.02	0.02	0.05
35	44.51	31.00	38.84	39.05	31.32	30.70	27.94	28.23	28.34	16.70	16.00	15.57	14.43	15.28	21.38	21.13	19.55	20.33
00	0.00	0.00	0.01	0.01	0.34	0.12	0.15	0.19	0.35	11.91	10.69	10.28	10.11	10.76	0.01	0.00	0.03	0.01
01	0.01	0.01	0.00	0.00	0.01	0.01	0.01	0.04	0.02	2.96	3.38	3.06	3.53	3.22	1.02	1.24	1.82	1.16
00	0.01	0.00	0.00	0.01	0.01	0.01	0.00	0.01	0.00	1.01	0.48	0.22	0.42	0.62	9.01	8.31	7.49	7.77
13	0.21	0.23	0.10	0.08	0.04	0.05	0.02	0.04	0.02	0.10	0.05	0.04	0.02	0.08	0.11	0.14	0.07	0.03
.23	100.89	100.90	100.41	100.19	100.45	100.57	101.00	100.28	99.60	97.87	96.68	97.70	97.85	97.00	94.47	95.33	95.34	94.66
.8	83.3	72.1	75.9	75.7	84.2	83.5	76.3	78.5	78.2	83.9	80.2	76.5	73.5	75.8	88.8	84.6	82.6	81.6
46	8.96	2.11	11.3	11.5	1.60	1.31	5.80	1.46	0.62	1.54	1.76	9.41	5.72	2.11	0.54	92.18	6.99	11.8
68	7.11	1.60	4.47	3.64	3.91	6.62	2.27	3.93	3.33	8.50	11.3	4.56	4.89	5.03	2.99	2.18	3.62	3.64
2	160	92.9	110	89.0	48.8	62.4	9.87	23.7	48.9	214	231	205	326	312	21.5	15.8	30.5	24.5
[b]	n.d.	n.d.	n.d.	n.d.	72.2	29.5	102	192	17.7	10012	4031	2668	4379	6578	72573	68889	71717	90112
18	5.13	3.32	1.98	2.04	13.1	10.5	6.79	10.1	13.3	62.6	33.1	44.1	48.8	61.4	8.67	2.78	5.12	8.63
98	7.29	23.5	11.9	6.17	374	477	309	728	566	16169	10009	12142	18069	15712	18088	7576	22944	26631
24	0.15	1.19	0.26	0.40	56.0	51.2	27.7	64.2	137	437	235	350	371	760	277	158	247	555
43	1.31	41.0	1.85	2.35	609	609	338	791	1369	3747	2746	559	3839	4906	2916	1020	2243	3705
.7	129	175	170	160	37.3	47.4	52.6	55.0	60.9	26.1	31.7	45.3	44.1	40.6	32.5	62.0	57.5	50.5
37	1769	1953	741	707	289	356	325	139	206	441	478	509	227	251	762	1062	391	360

ne			Orthopyroxene							Amphibole					Phlogopite			
ec vaga	Castello di Gavala	Fei di Doccio	Valmaggia (core)[a]	Valmaggia (rim)[a]	Bec d'Ovaga	Castello di Gavala	Fei di Doccio	Valmaggia (core)[a]	Valmaggia (rim)[a]	Bec d'Ovaga	Castello di Gavala	Fei di Doccio	Valmaggia (core)[a]	Valmaggia (rim)[a]	Bec d'Ovaga	Fei di Doccio	Valmaggia (core)[a]	Valmaggia (rim)[a]
01	GV1262A	FD1	VMG7	I7	BO1	GV1262A	FD1	VMG7	I7	BO1	GV1262A	FD1	VMG7	I7	BO1	FD1	VMG7	I7
3	8	4	13	7	6	10	7	7	5	4	14	6	9	6	5	5	10	6
43	1.95	0.16	6.44	0.46	0.17	0.53	0.17	0.26	bdl.[c]	87.4	4.88	1.60	1.44	1.23	3.49	0.49	0.80	2.99
.3	33.8	105.9	99.6	74.7	42.1	43.6	86.1	92.4	87.8	16.0	16.8	39.1	34.6	28.0	31.4	49.7	25.4	26.3
02	0.07	0.22	0.01	0.08	5.12	6.32	4.62	9.20	9.95	14.5	10.8	20.6	18.4	18.5	9.58	19.6	15.0	14.8
35	2.48	3.54	3.44	3.45	2.46	3.03	3.23	3.09	3.46	3.04	2.38	3.05	2.66	2.94	0.53	1.45	1.14	1.75
d.	n.d.	n.d.	n.d.	n.d.	0.067	0.20	0.35	0.65	bdl.	11.9	3.35	2.67	1.52	4.21	1244	226	220	391
d.	n.d.	n.d.	n.d.	n.d.	1.10	2.57	0.65	2.66	0.60	207	418	120	302	255	47.9	85.6	157	68.7
01	0.01	0.05	0.02	0.01	0.39	0.23	0.24	0.67	1.18	42.1	24.4	67.0	71.6	53.1	0.04	0.10	0.07	0.02
03	0.04	0.23	0.07	0.05	4.02	2.71	1.79	5.63	18.0	328	147	218	376	563	3.83	1.22	8.75	16.7
00	0.00	0.02	0.01	0.00	0.09	0.03	0.05	0.14	0.04	19.1	6.7	27.6	19.2	26.9	8.75	10.4	15.3	21.0
01	0.01	0.02	0.02	0.01	0.01	0.02	0.04	0.04	0.04	0.03	0.10	0.16	0.29	0.17	0.02	0.07	0.21	0.10
d.	n.d.	n.d.	n.d.	n.d.	0.18	0.38	0.27	0.13	bdl.	0.74	2.19	0.90	0.37	0.35	bdl.	0.20	bdl.	bdl.
d.	n.d.	n.d.	n.d.	n.d.	0.01	0.03	0.08	0.03	bdl.	0.38	0.02	0.15	0.04	0.03	75.8	15.5	8.12	12.7
d.	n.d.	n.d.	n.d.	n.d.	1.85	0.77	2.10	7.20	0.37	340	62.8	62.3	134	201	6811	1825	3495	5022
d.	n.d.	n.d.	n.d.	n.d.	0.08	0.09	0.14	0.16	0.15	15.7	9.94	16.4	14.2	20.5	0.03	0.07	0.06	0.05
d.	n.d.	n.d.	n.d.	n.d.	0.25	0.15	0.24	0.32	0.36	48.6	29.0	59.0	49.4	70.1	0.02	0.14	0.12	0.09
d.	n.d.	n.d.	n.d.	n.d.	0.03	0.02	0.03	0.04	0.04	7.92	4.35	9.79	8.92	11.3	0.00	0.01	0.05	0.01
d.	n.d.	n.d.	n.d.	n.d.	0.19	0.08	0.10	0.16	0.16	37.6	20.1	48.8	47.1	51.1	0.01	0.09	0.11	0.04
d.	n.d.	n.d.	n.d.	n.d.	0.04	0.01	0.02	0.04	0.05	8.61	4.82	13.1	12.9	11.2	0.01	0.02	0.03	0.03
d.	n.d.	n.d.	n.d.	n.d.	0.02	0.01	0.02	0.03	0.03	2.59	1.61	2.83	3.75	3.20	0.36	0.06	0.09	0.21
d.	n.d.	n.d.	n.d.	n.d.	0.08	0.04	0.01	0.07	0.08	8.39	4.81	12.8	13.8	9.76	0.07	0.01	0.05	0.02
d.	n.d.	n.d.	n.d.	n.d.	0.01	0.01	0.01	0.02	0.02	1.22	0.73	2.04	2.08	1.47	0.00	0.00	0.01	0.00
d.	n.d.	n.d.	n.d.	n.d.	0.06	0.03	0.04	0.10	0.15	7.91	4.65	12.8	13.4	9.28	0.01	0.02	0.02	0.01
d.	n.d.	n.d.	n.d.	n.d.	0.02	0.01	0.02	0.02	0.04	1.63	0.94	2.53	2.73	1.98	0.00	bdl.	0.01	0.00
d.	n.d.	n.d.	n.d.	n.d.	0.06	0.03	0.04	0.09	0.17	4.25	2.56	6.90	7.39	5.74	0.01	0.02	0.03	0.00
d.	n.d.	n.d.	n.d.	n.d.	0.01	0.01	0.01	0.02	0.03	0.57	0.36	0.95	1.04	0.85	0.00	0.00	0.01	0.00
d.	n.d.	n.d.	n.d.	n.d.	0.13	0.06	0.06	0.21	0.38	3.64	2.37	6.16	6.79	5.89	0.01	0.02	0.05	0.02

ne			Orthopyroxene					Amphibole					Phlogopite					
ec vaga	Castello di Gavala	Fei di Doccio	Valmaggia (core)[a]	Valmaggia (rim)[a]	Bec d'Ovaga	Castello di Gavala	Fei di Doccio	Valmaggia (core)[a]	Valmaggia (rim)[a]	Bec d'Ovaga	Castello di Gavala	Fei di Doccio	Valmaggia (core)[a]	Valmaggia (rim)[a]	Bec d'Ovaga	Fei di Doccio	Valmaggia (core)[a]	Valmaggia (rim)[a]
01	GV1262A	FD1	VMG7	I7	BO1	GV1262A	FD1	VMG7	I7	BO1	GV1262A	FD1	VMG7	I7	BO1	FD1	VMG7	I7
3	8	4	13	7	6	10	7	7	5	4	14	6	9	6	5	5	10	6
d.	n.d.	n.d.	n.d.	n.d.	0.02	0.02	0.01	0.04	0.08	0.53	0.35	0.85	0.97	0.89	0.00	0.00	0.01	0.00
00	0.01	0.01	0.02	0.01	0.15	0.07	0.05	0.21	0.59	7.69	3.41	10.0	8.52	13.1	0.11	0.05	0.29	0.51
00	0.00	bdl.	0.00	0.00	0.01	0.00	0.00	0.01	0.00	1.11	0.39	1.49	0.91	1.34	0.45	0.50	0.83	1.15
06	0.37	0.22	0.07	0.08	0.12	0.62	0.23	0.19	0.04	15.6	47.2	6.07	6.85	6.98	30.5	35.5	15.0	14.2
d.	n.d.	n.d.	n.d.	n.d.	0.06	0.04	0.43	0.08	0.04	0.76	1.20	1.17	0.77	0.88	0.02	0.02	0.25	0.00
d.	n.d.	n.d.	n.d.	n.d.	0.01	0.01	0.03	0.04	0.01	0.13	0.27	0.20	0.15	0.18	0.00	0.00	0.01	bdl.

are in wt% and were determined by electron microprobe. All other values (i.e. Li to U) are in ppm and were determined by laser ablation ICP-MS. All data are presented in Appendix
gma uncertainties and lower levels of detection.

lude analyses of mineral cores. All data and a core-rim comparison are presented in Appendices A2 and A3.

ined.

ction limit. The detection limits and 1-sigma error for each analysis are presented in Appendix A2.

Table 3:

U-Pb isotopic data for zircons from Valmaggia. Sample weights are calculated from crystal dimensions and are associated with as much as 50% uncertainty (estimated) Pb_c = Total common Pb including analytical blank (0.8±0.3 pg per analysis). Blank composition is: $^{206}Pb/^{204}Pb$ = 18.55 ± 0.63, $^{207}Pb/^{204}Pb$ = 15.50 ± 0.55, $^{208}Pb/^{204}Pb$ = 38.07 ± 1.56 (all 2σ), and a $^{206}Pb/^{204}Pb$ – $^{207}Pb/^{204}Pb$ correlation of 0.9. Th/U calculated from radiogenic $^{208}Pb/^{206}Pb$ and age. Measured isotopic ratios corrected for tracer contribution and mass fractionation (0.02 ± 0.06 %/amu). ρ = error correlation coefficient of radiogenic $^{207}Pb/^{235}U$ vs. $^{206}Pb/^{238}U$. All uncertainties given at 2σ Ratios involving ^{206}Pb are corrected for initial disequilibrium in $^{230}Th/^{238}U$ using Th/U = 4 in the crystallization environment.

Sample	wt. (Hg)	U (ppm)	Pbc (pg)	mol% Pb*	$\frac{Th}{U}$	$\frac{206Pb}{204Pb}$	$\frac{207Pb}{206Pb}$	± (%)	$\frac{207Pb}{235U}$	± (%)	$\frac{206Pb}{238U}$	± (%)	ρ	$^{206}Pb/^{238}U$ Age (Ma)	± (Ma)	$^{207}Pb/^{206}Pb$ Age (Ma)	± (Ma)
VMG-2: 1 crystal per fraction																	
1	0.4	165	0.8	78	0.68	201	0.05118	2.26	0.2786	2.42	0.03948	0.34	.54	249.6	0.8	249.0	51.9
2	0.8	264	1.9	83	0.75	285	0.05182	1.64	0.2818	1.76	0.03944	0.25	.54	249.3	0.6	277.6	37.4
3	0.4	176	1.9	61	0.65	104	0.05297	3.50	0.2879	3.74	0.03941	0.27	.89	249.2	0.7	327.5	79.4
4	0.6	149	0.6	87	0.72	339	0.05115	0.29	0.2778	0.32	0.03938	0.12	.47	249.0	0.3	247.5	6.6
5	0.9	302	3.2	79	0.82	226	0.05118	0.49	0.2778	0.61	0.03936	0.32	.59	248.9	0.8	249.1	11.3
6	1.2	190	3.5	70	0.63	153	0.05255	3.46	0.2445	3.69	0.03375	0.24	.95	214.0	0.5	309.6	78.7

Table 4 -

Calculated compositions of basaltic melts in equilibrium with amphiboles and melts

	Melts in equilibrium with amphibole				Melts produced by
	Valmaggia	**Fei di Doccio**	**Bec d'Ovago**	**Castello di Gavala**	**0% melt**
P (ppm)	7755	4764	4983	5370	25256
K	7195	2964	11125	4478	10691
Ti	9561	7541	10043	6217	11636
Cr	409	47.0	315	231	291
Co	20.5	23.6	13.6	16.5	13.2
Ni	27.7	59.1	51.3	55.6	13.7
Cu	0.748	1.00	54.6	3.05	23.8
Zn	92.8	140	57.2	60.0	114
Rb	41.8	26.7	119	33.5	257
Sr	494	236	406	828	1195
Zr	2348	908	1367	613	1000
Nb	90.2	92.1	63.5	22.4	33.7
Cs	8.59	36.8	95.0	4.93	406
Ba	659	222	1215	224	431
La	201	164	157	99.4	215
Ce	408	347	286	171	307
Nd	123	119	91.6	49.1	81.3
Sm	16.8	20.2	13.2	7.41	12.3
Tb	1.62	2.29	1.37	0.815	1.32
Ho	2.14	2.75	1.77	1.02	1.65
Yb	11.9	12.3	7.27	4.73	6.91
Lu	1.23	1.17	0.740	0.482	0.670
Hf	33.2	24.5	18.7	8.31	13.3
Ta	4.72	4.98	3.70	1.30	2.23
Pb	143	126	325	983	4.73
Th	66.6	90.3	58.5	92.1	206.2
U	12.1	14.1	9.29	19.4	53.4